

AD-A041 152

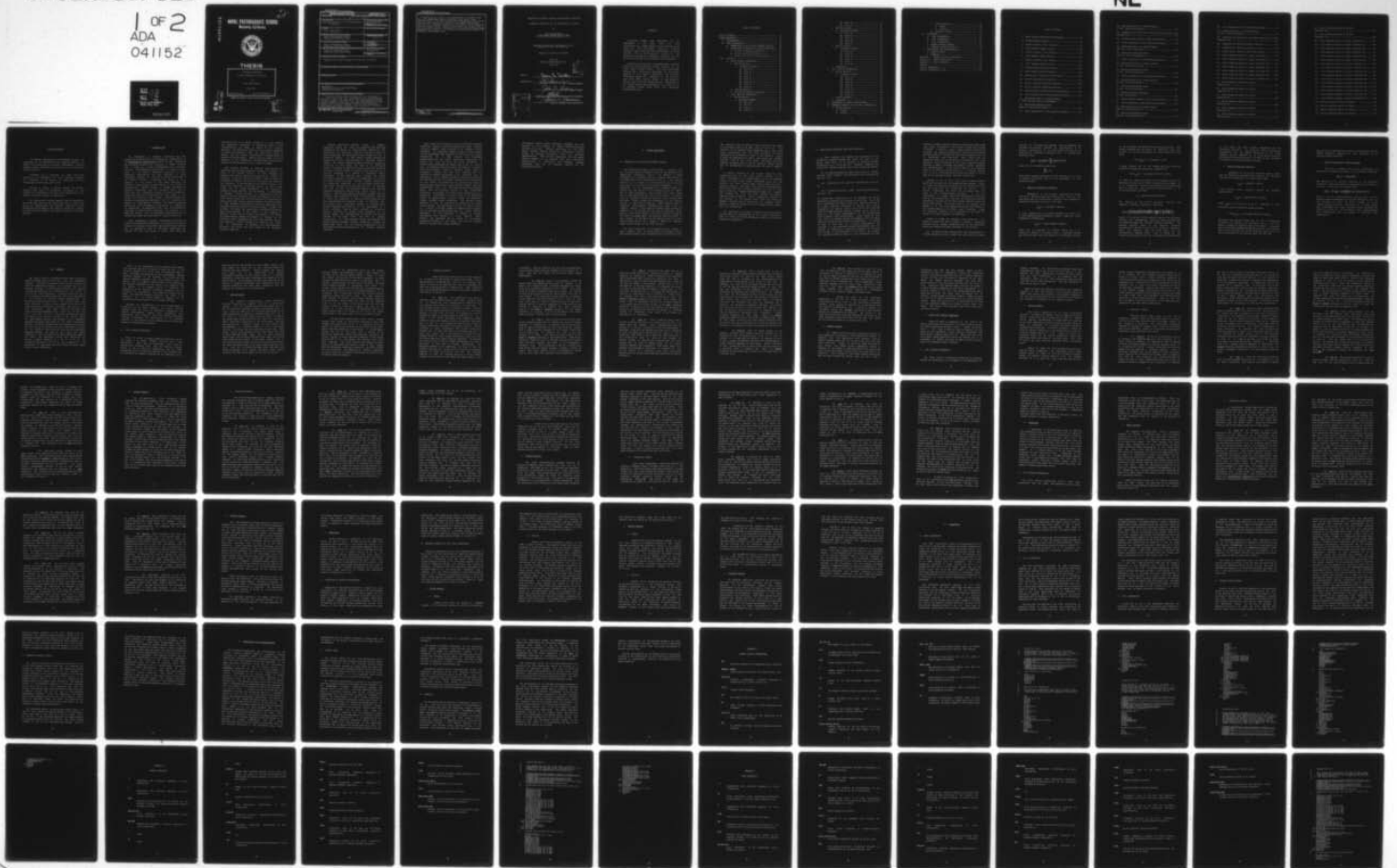
NAVAL POSTGRADUATE SCHOOL MONTEREY CALIF
COMPUTER SIMULATION OF THE SPUTTERING OF SILICON.(U)
JUN 77 G L SMITH

F/G 13/8

UNCLASSIFIED

1 OF 2
ADA
041152

NL



ADA 041152

Handwritten initials and number 2

NAVAL POSTGRADUATE SCHOOL

Monterey, California



THESIS

COMPUTER SIMULATION
OF THE SPUTTERING OF SILICON
by
Gary Lloyd Smith
June 1977
Thesis Advisor: Don E. Harrison, Jr.

Approved for public release; distribution unlimited.

AD No.
DDC FILE COPY

Handwritten initials
DDC
RECEIVED
JUL 5 1977
RL
D

UNCLASSIFIED

SECURITY CLASSIFICATION OF THIS PAGE (When Data Entered)

REPORT DOCUMENTATION PAGE		READ INSTRUCTIONS BEFORE COMPLETING FORM
1. REPORT NUMBER	2. GOVT ACCESSION NO.	3. RECIPIENT'S CATALOG NUMBER 9
4. TITLE (and Subtitle) 6 Computer Simulation of the Sputtering of Silicon		5. TYPE OF REPORT & PERIOD COVERED Master's Thesis June 1977
7. AUTHOR(s) 10 Gary Lloyd/Smith		6. PERFORMING ORG. REPORT NUMBER
9. PERFORMING ORGANIZATION NAME AND ADDRESS Naval Postgraduate School Monterey, California 93940		8. CONTRACT OR GRANT NUMBER(s)
11. CONTROLLING OFFICE NAME AND ADDRESS Naval Postgraduate School Monterey, California 93940		10. PROGRAM ELEMENT, PROJECT, TASK AREA & WORK UNIT NUMBERS 12 176p
14. MONITORING AGENCY NAME & ADDRESS (if different from Controlling Office) Naval Postgraduate School Monterey, California 93940		12. REPORT DATE 11 June 1977
		13. NUMBER OF PAGES 176
		15. SECURITY CLASS. (of this report) Unclassified
		15a. DECLASSIFICATION/DOWNGRADING SCHEDULE
16. DISTRIBUTION STATEMENT (of this Report) Approved for public release; distribution unlimited		
17. DISTRIBUTION STATEMENT (of the abstract entered in Block 20, if different from Report)		
18. SUPPLEMENTARY NOTES		
19. KEY WORDS (Continue on reverse side if necessary and identify by block number) Sputtering Computer simulation and sputtering Sputtering of silicon		
20. ABSTRACT (Continue on reverse side if necessary and identify by block number) Simulation models were developed for the bombardment of the (100), (110), and (111) orientations of a single-crystal silicon lattice by an argon ion. The interatomic potentials included repulsive terms only, and were approximated in closed analytic form by least-squares fitting of the calculated interatomic potentials obtained from the Hartree-Fock-Slater self-consistent field equations. → next page		

DD FORM 1473
1 JAN 73

EDITION OF 1 NOV 65 IS OBSOLETE
S/N 0102-014-6601

UNCLASSIFIED

SECURITY CLASSIFICATION OF THIS PAGE (When Data Entered)

257 450

UNCLASSIFIED

SECURITY CLASSIFICATION OF THIS PAGE(When Data Entered)

→ Sputtering was found to be predominantly a surface effect with most sputtering events occurring in the first three crystal layers. The (110) orientation demonstrated a sputtering mechanism not previously observed in fcc copper simulations, and the (111) orientation showed that reflection of the knock-on atom from lower crystal layers is more common in silicon than in the fcc copper lattice. Adjustment of the surface binding energy parameter to a value of 4-7 eV produced results which agree with available experimental data.

DD Form 1473
1 Jan 73
S/N 0102-014-6601

UNCLASSIFIED
2 SECURITY CLASSIFICATION OF THIS PAGE(When Data Entered)

Approved for public release; distribution unlimited.

Computer Simulation of the Sputtering of Silicon

by

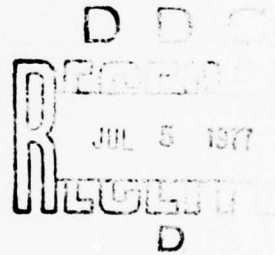
Gary Lloyd Smith
Lieutenant, United States Navy
B.S.E.E., Purdue University, 1971

Submitted in partial fulfillment of the
requirements for the degree of

MASTER OF SCIENCE IN PHYSICS

from the
NAVAL POSTGRADUATE SCHOOL

June 1977



Author:

Gary L. Smith

Approved by:

D. C. Garrison
Thesis Advisor

John N. Cooper
Second Reader

W. W. Miller
Chairman, Department of Physics and Chemistry

Robert A. Johnson
Dean of Science and Engineering

ACCESSION for	
NTIS	White Section <input checked="" type="checkbox"/>
DDC	Buff Section <input type="checkbox"/>
UNANNOUNCED	<input type="checkbox"/>
JUSTIFICATION	
BY	
DISTRIBUTION/AVAILABILITY CODES	
DDC SPECIAL/OTHER SPECIAL	
A	

ABSTRACT

Simulation models were developed for the bombardment of the (100), (110), and (111) orientations of a single-crystal silicon lattice by an argon ion. The interatomic potentials included repulsive terms only, and were approximated in closed analytic form by least-squares fitting of the calculated interatomic potentials obtained from the Hartree-Fock-Slater self-consistent field equations.

Sputtering was found to be predominantly a surface effect with most sputtering events occurring in the first three crystal layers. The (110) orientation demonstrated a sputtering mechanism not previously observed in fcc copper simulations, and the (111) orientation showed that reflection of the knock-on atom from lower crystal layers is more common in silicon than in the fcc copper lattice. Adjustment of the surface binding energy parameter to a value of 4-7 eV produced results which agree with available experimental data.

TABLE OF CONTENTS

LIST OF FIGURES.....	8
ACKNOWLEDGEMENTS.....	12
I. INTRODUCTION.....	13
II. MODEL DEVELOPMENT.....	18
A. GENERATION OF THE SILICON DIAMOND LATTICE....	18
B. INTERACTION POTENTIALS AND FORCE FUNCTIONS...	20
1. Ar-Si ⁺ Interaction Potential.....	22
2. Si-Si ⁺ Potential Function.....	24
3. Ar-Si ⁺ and Si-Si ⁺ Force Functions.....	25
III. RESULTS.....	26
A. (100) LATTICE ORIENTATION.....	27
1. 600-eV Results.....	28
a. Mechanism Summary.....	30
(1) Atom 32.....	30
(2) Atom 15.....	31
(3) Atom 9.....	31
(4) Atom 7.....	32
(5) Atom 18.....	32
(6) Atom 119.....	33
(7) Atom 57.....	33
(8) Atom 65.....	34
2. 1000-eV Results.....	34
3. 600-eV and 1000-eV Comparison.....	35
B. (110) LATTICE ORIENTATION.....	35
1. 600-eV Results.....	36
a. Mechanism Summary.....	37
(1) Atom 23.....	37
(2) Atom 14.....	38
(3) Atom 4.....	38
(4) Atom 48.....	39

	(5) Atom 18.....	39
	(6) Atom 61.....	40
2.	1000-eV Results.....	41
	a. Mechanism Summary.....	42
	(1) Atom 23.....	42
	(2) Atom 14.....	43
	(3) Atom 48.....	43
	(4) Atom 18.....	44
	(5) Atom 65.....	44
3.	2000-eV Results.....	45
	a. Mechanism Summary.....	46
	(1) Atom 23.....	47
	(2) Atom 14.....	47
	(3) Atom 13.....	48
	(4) Atom 12.....	48
	(5) Atom 4.....	48
	(6) Atom 18.....	49
4.	Comparison.....	50
C.	(111) LATTICE ORIENTATION.....	50
	1. 600-eV Results.....	51
	a. Mechanism Summary.....	52
	(1) Atom 30.....	52
	(2) Atom 24.....	53
	(3) Atom 31.....	53
	(4) Atom 25.....	53
	(5) Atom 47.....	54
	(6) Atom 119.....	54
	(7) Atom 63.....	55
	(8) Atom 95.....	55
	2. 1000-eV Results.....	56
	3. Comparison.....	57
D.	COMPARISON OF LATTICE ORIENTATIONS.....	57
E.	MOMENTUM TRANSFER IN THE (100) ORIENTATION... 58	
	1. 600-eV Results.....	58
	a. Copper.....	58
	b. Silicon.....	59

2.	1000-eV Results.....	60
a.	Copper.....	60
b.	Silicon.....	60
3.	Precursor Motion.....	61
IV.	DISCUSSION.....	63
A.	(100) ORIENTATION.....	63
B.	(110) ORIENTATION.....	64
C.	(111) ORIENTATION.....	65
D.	SURFACE BINDING ENERGY.....	66
E.	MOMENTUM TRANSFER STUDIES.....	68
V.	CONCLUSIONS AND RECOMMENDATIONS.....	70
A.	LATTICE MODEL.....	71
B.	DYNAMICS.....	72
Appendix A:	DIAMOND LATTICE SUBROUTINES.....	75
Appendix B:	ENERGY SUBROUTINE.....	83
Appendix C:	STEP SUBROUTINE.....	89
FIGURES.....		97
LIST OF REFERENCES.....		174
INITIAL DISTRIBUTION LIST.....		176

LIST OF FIGURES

1. Basic Silicon Tetrahedral Arrangement.....	97
2. Diamond Microcrystalite.....	98
3. Silicon Lattice, (100) Surface.....	99
4. (100) Surface Impact Points.....	100
5. Silicon Lattice, (110) Surface.....	101
6. (110) Surface Impact Points.....	102
7. Silicon Lattice, (111) Surface.....	103
8. (111) Surface Impact Points.....	104
9. Silicon Radial Electron Density.....	105
10. Argon Radial Electron Density.....	106
11. Argon-Silicon Interaction Potentials.....	107
12. Si-Si ⁺¹ Interaction Potential.....	108
13. Ar-Si ⁺⁴ Analytic Potential Function.....	109
14. Si-Si ⁺¹ Analytic Potential Function.....	110
15. Silicon Single Crystal [(100) Orientation].....	111
16. (100) Orientation, 600-eV Sputtering Events.....	112
17. Sputtering Ratio vs. Binding Energy [(100) Lattice, 600-eV bombardment].....	113
18. Sputtering Mechanism Trace [600 eV, (100) Orientation].....	114
19. (100) Orientation, 1-keV Sputtering Events.....	115

20. Sputtering Ratio vs. Binding Energy [1 keV, (100) Orientation].....	116
21. Comparison of 600-eV and 1-keV Sputtering Ratios [(100) Orientation].....	117
22. Silicon Single Crystal [(110) Orientation].....	118
23. (110) Orientation, 600-eV Sputtering Events.....	119
24. Sputtering Ratio vs. Binding Energy [600 eV, (110) Orientation].....	120
25. Sputtering Mechanism Trace [600 eV, (110) Orientation].....	121
26. (110) Orientation, 1-keV Sputtering Events.....	122
27. Sputtering Ratio vs. Binding Energy [1 keV, (110) Orientation].....	123
28. Sputtering Mechanism Trace [1 keV, (110) Orientation].....	124
29. (110) Orientation, 2-keV Sputtering Events.....	125
30. Sputtering Ratio vs. Binding Energy [2 keV, (110) Orientation].....	126
31. Sputtering Mechanism Trace [2 keV, (110) Orientation].....	127
32. Sputtering Ratio Comparison [(110) Orientation].....	128
33. Silicon Single Crystal [(111) Orientation].....	129
34. (111) Orientation, 600-eV Sputtering Events.....	130
35. Sputtering Ratio vs. Binding Energy [600 eV, (111) Orientation].....	131
36. Sputtering Mechanism Trace [600 eV, (111) Orientation].....	132

37.	(111) Orientation, 1-keV Sputtering Events.....	133
38.	Sputtering Ratio vs. Binding Energy [1 keV, (111) Orientation].....	134
39.	Comparison of 600-eV and 1-keV Sputtering Ratios [(111) Orientation].....	135
40.	Comparison of Sputtering Ratios (600 eV).....	136
41.	Comparison of Sputtering Ratios (1 keV).....	137
42.	Copper Single Crystal [(100) Orientation].....	138
43.	600-eV Momentum Spread in Copper (Timestep 1).....	139
44.	600-eV Momentum Spread in Copper (Timestep 5).....	140
45.	600-eV Momentum Spread in Copper (Timestep 15).....	141
46.	600-eV Momentum Spread in Copper (Timestep 20).....	142
47.	600-eV Momentum Spread in Copper (Timestep 25).....	143
48.	600-eV Momentum Spread in Copper (Timestep 27).....	144
49.	600-eV Momentum Spread in Silicon (Timestep 1).....	145
50.	600-eV Momentum Spread in Silicon (Timestep 10).....	146
51.	600-eV Momentum Spread in Silicon (Timestep 20).....	147
52.	600-eV Momentum Spread in Silicon (Timestep 30).....	148
53.	600-eV Momentum Spread in Silicon (Timestep 40).....	149
54.	600-eV Momentum Spread in Silicon (Timestep 50).....	150
55.	600-eV Momentum Spread in Silicon (Timestep 60).....	151

56.	600-eV Momentum Spread in Silicon (Timestep 70).....	152
57.	600-eV Momentum Spread in Silicon (Timestep 72).....	153
58.	1-keV Momentum Spread in Copper (Timestep 1).....	154
59.	1-keV Momentum Spread in Copper (Timestep 5).....	155
60.	1-keV Momentum Spread in Copper (Timestep 15).....	156
61.	1-keV Momentum Spread in Copper (Timestep 20).....	157
62.	1-keV Momentum Spread in Copper (Timestep 26).....	158
63.	1-keV Momentum Spread in Copper (Timestep 29).....	159
64.	1-keV Momentum Spread in Silicon (Timestep 1).....	160
65.	1-keV Momentum Spread in Silicon (Timestep 10).....	161
66.	1-keV Momentum Spread in Silicon (Timestep 20).....	162
67.	1-keV Momentum Spread in Silicon (Timestep 30).....	163
68.	1-keV Momentum Spread in Silicon (Timestep 40).....	164
69.	1-keV Momentum Spread in Silicon (Timestep 50).....	165
70.	1-keV Momentum Spread in Silicon (Timestep 60).....	166
71.	1-keV Momentum Spread in Silicon (Timestep 70).....	167
72.	1-keV Momentum Spread in Silicon (Timestep 80).....	168
73.	1-keV Momentum Spread in Silicon (Timestep 87).....	169
74.	600-eV Precursor Motion in Copper.....	170
75.	600-eV Precursor Motion in Copper.....	171
76.	600-eV Precursor Motion in Silicon.....	172
77.	600-eV Precursor Motion in Silicon.....	173

ACKNOWLEDGEMENTS

No computer simulation can be successful without the assistance of an efficiently run computer facility. My thanks to the personnel of the Naval Postgraduate School's computer center, especially the operators on the evening and midnight shifts.

Professor Don E. Harrison, Jr. spent many hours assisting in the development of this simulation program. His knowledge of the physics of sputtering, and his encouragement are greatly appreciated.

Patrick W. Kelly, a fellow student and friend, provided many hours of stimulating discussion on the simulation of sputtering. His aid in the compilation of the computer variable glossary is appreciated.

My very special thanks, however, must be extended to my loving wife Judi, who has endured many hours alone both during my undergraduate and graduate education, and who keypunched this manuscript for computer processing. Without her assistance and devotion my education would not have been possible.

I. INTRODUCTION

The phenomenon of physical sputtering has been extensively studied since its discovery and description in the Philosophical Transactions by Grove in 1852. Sputtering may be broadly viewed as the ejection of atomic material from a target as a result of bombardment by an energetic particle. The bombarding particles may be neutral atoms, ions, or the heavier elementary particles; but most scientific investigation has been restricted to ionic bombardment because the ions can be easily accelerated to any desired velocity. Sputtering has proven to be a nuisance in the design of high power amplifier and oscillator tubes because of grid erosion, in the design of thermonuclear reactors because of plasma contamination caused by sputtering from the container walls, and in solar-wind and atmospheric erosion of orbiting satellites. Useful applications of sputtering have been found in the fields of ion-getter pump design, thin-film deposition, etching of metallurgical specimens, and the cleaning and etching of semiconductor surfaces. The complete physical description of the phenomenon of sputtering is complicated by limitations of experimental technique, the mathematical difficulty of theoretically describing the behavior of a many-body system, and the incomplete understanding of the interacting forces and potentials in crystal structures.

Early experiments typically determined the sputtering ratio of polycrystalline materials. The sputtering ratio is defined as the number of target atoms sputtered per incident ion. An exhaustive study of low-energy sputtering was carried out over the course of seven years under the

direction of Dr. G. K. Wehner. Wehner et al [1] reported the temperature dependence of sputtering yields in the semiconductors, the effect of oxygen on ion ejection patterns, the sputtering yields of various metals bombarded by atomic and polyatomic ions, the sputtering yields of oxides, and the spatial distribution of ejected atoms in metals and semiconductors. Earlier work by Wehner et al [2] resulted in the compilation of sputtering yield data for metals and semiconductors in the 100-600 eV range.

The earliest attempts to describe theoretically the mechanisms of sputtering generally ignored the ordering of atoms in the crystal lattice. In 1921, Thompson [3] proposed that atomic ejection was caused by the release of radiation as the ion struck the target. Bush and Smith [4] attempted to describe the ejection of atoms as the result of the expansion of gas adsorbed by the target material. Von Hippel [5] presented the 'Hot-Spot Theory' in 1926, which stated that the energy dissipation of the slowing ion evaporated target material from the surface. A theory based on momentum transfer between the bombarding ion and the lattice atoms was proposed by Lamar and Compton [5] in 1934. Their theory stated that ions may penetrate the material and recoil from lower layers, causing ejection of surface atoms. In 1956 Harrison [7] proposed a theory for sputtering from amorphous materials based on transport theory. Silsbee [8] proposed the theory that sputtering in preferred directions from single crystals is the result of the focusing of momentum along a line of atoms in the crystal. This theory was questioned by Lehmann and Sigmund [9] because of the extremely short pathlength of the Silsbee focusons even at high energies. In 1969, Sigmund [10] reported his theory for the sputtering of amorphous and polycrystalline materials. His theory was also based on the Boltzmann transport equation.

Analytic sputtering theories cannot, in general, adequately define and treat the parameters and variables required in the theory of single-crystal sputtering. The development of high-speed computers offered the chance to better understand the sputtering process through the use of simulation models. In 1960, Gibson, Goland, Milgram, and Vineyard [11] built a computer model to represent metallic copper, and studied radiation damage events at energies up to 400 eV. In this model, one atom in the stationary lattice was given an arbitrary kinetic energy and direction of motion, and was allowed to interact with the atoms in the lattice, resulting in a cascade of independent binary collisions. In 1967, Harrison, Levy, Johnson, and Effron [12] used a computer to simulate the bombardment of a single fcc copper crystal by argon. Through computer simulation, the sputtering mechanisms in the fcc copper crystal were identified. Harrison et al reported that for ion energies less than 10 keV, the sputtering process in fcc crystals occurred predominantly within three atomic layers of the surface. The initial computer simulation included only the repulsive forces between the atoms. The algorithm utilized to solve the equations of motion in this simulation and later simulations was described in 1969 by Harrison, Gay, and Effron [13]. Continuing efforts to develop a more precise computer model resulted in the development of a Cu-Cu potential function which included an attractive portion, inclusion of surface layer relaxation in the crystal model, and determination of surface atom binding energies of the (100), (110), and (111) Cu crystal orientations. In 1972, Harrison, Moore, and Holcombe [14] showed improved agreement between simulation results and experimental data, but the original interpretation of the low-energy sputtering mechanisms in fcc crystals remained unchanged.

This thesis is an extension of the previous NPS computer simulation studies to silicon bombarded by argon. Silicon, a group IV element, forms a crystal in the diamond lattice structure. An acceptable computer model of single-crystal silicon bombardment must generate the lattice in the proper orientation, and it must simulate with reasonable approximations of the atomic interaction potentials and forces for both the Ar-Si and Si-Si collisions. A statistically representative impact area of the Si lattice must be determined for each crystal orientation, a suitable force and potential truncation distance (which allows a reasonable computer run time while ensuring that the principle of energy conservation is not violated) must be determined, and the maximum allowable distance moved by the most energetic atom in any given timestep must be determined so that forces and velocities are updated often enough to ensure energy conservation without making computer run times prohibitively long. For this preliminary silicon/diamond model, only the repulsive portion of the interatomic potentials is included, and surface layer relaxation is not considered. Furthermore, the lack of data on the sputtering yields of single-crystal silicon leaves the problem of surface binding energy unresolved. The minimum energy required to free an atom from the surface is the surface binding energy. For sputtering to occur, the kinetic energy of a lattice atom must exceed the surface binding energy, and the atom must be moving away from the target surface. Adjustment of this parameter to conform to reliable experimental data results in a more accurate model. However, this parameter has no effect on the physical mechanisms involved in the model, and can be adjusted whenever suitable data become available.

The diamond lattice model developed possesses the same features as the original fcc copper model developed by Harrison et al [12]. Further refinements of this model should include surface relaxation, interatomic cohesive energy, and perhaps non-central force and potential approximations. From earlier experience with the copper crystal however, it is expected that this preliminary identification of sputtering and momentum transfer mechanisms will not be affected greatly by the oversimplifications.

II. MODEL DEVELOPMENT

A. GENERATION OF THE SILICON DIAMOND LATTICE

The directional covalent bonds between a silicon atom and its four nearest neighbors result in the formation of a symmetrical tetrahedron (Fig.1). The bonding of these tetrahedra with successive nearest neighbors then results in the formation of the diamond lattice (Fig 2). The lattice constant a in silicon is 5.43 angstroms, and the lattice unit, which is the width of the basic tetrahedron, is 2.72 angstroms. In the development of the computer model, the lattice unit (LU) proves to be a convenient unit of length, and is used extensively. This lattice is fcc with a basis of two atoms associated with each lattice point. The second atom is displaced 0.86602 LU along the (111) diagonal from the first. Figure 3 shows the arrangement of the silicon lattice in the (100) orientation. Square abcd in Figure 3 encloses a statistically representative impact area for normally incident ions, which by folding along two axes of symmetry (e.g. ab and ad) will map into all possible impact points on the (100) surface. The (100) channel is shown at the center of square abcd. The distance from the center of this channel to the center of the nearest atom in the same vertical plane is 0.5 LU. Figure 4 shows the specific impact points chosen for the (100) surface.

The (110) orientation of the diamond lattice reveals a large channel (Fig. 5) through which the incoming ion may pass without making a hard collision with any lattice atom.

The distance from the center of this channel to the center of the closest atom in the same plane is 0.75 LU. This distance is the maximum impact parameter seen in any of the three orientations, and the Si-Ar potential and force functions must be modeled at least to this distance. Figure 6 shows the representative impact area used for normally incident ions on the (110) plane. The impact area abcd contains 30 impact points, and all possible impact points may be represented by a folding about the axis of symmetry ab.

A further rotation of the lattice yields the (111) orientation (Fig. 7). The large channel evident in the (110) orientation is no longer present, but an ion normally incident at point b may travel relatively deep into the lattice (the fifth plane) before experiencing more than a grazing collision. The small (111) channels surrounding the fifth plane atom have an impact parameter of 0.471 LU. This may be viewed as a "pseudo-channeling" effect, and suggests that perhaps the (110) and (111) surfaces may exhibit somewhat similar behavior. A more complicated folding of any triangle in the hexagon will yield the total area abcdefg. Triangle bcd was chosen for the computer model. Figure 8 shows the position of the 36 impact points used in the (111) orientation.

The subroutines utilized to generate the three lattice orientations are a modification of the lattice generators used by Finno in silicon channeling studies [15], and are discussed in Appendix A.

B. INTERACTION POTENTIALS AND FORCE FUNCTIONS

In 1967, Wedepohl [16] reported the calculation of the interaction energies between like atoms and ions in the energy range which is of interest in radiation damage calculations (i.e., 50 eV-10⁵ eV). Wedepohl compared the interaction energies obtained from three theoretical models:

(i) the quantum-mechanical (QM) radial electron density obtained using Hartree self-consistent field calculations (see ref. 17),

(ii) Thomas-Fermi (TF) electron distributions (see ref. 18).

(iii) Thomas-Fermi-Dirac (TFD) electron distributions (see ref. 19).

An unpublished modification of the Wedepohl QM method developed by Harrison was utilized to obtain the Si-Si and Ar-Si interaction potential functions. Tabulated values of the radial electron densities of various ionic states (including the neutral states) of Ar and Si were obtained from the Herman-Skillman computer program [20], which is based on the Slater approximation of the Hartree-Fock self-consistent field calculations. These densities were then used in a program similar to Wedepohl's [16] to obtain tabulated values of the interaction potentials. It should be kept in mind that the adiabatic approximation was utilized, i.e. the electronic charge distributions were not allowed to deform due to electronic repulsion as the atoms were brought in close proximity to each other. This results in a screening function which is in all likelihood too high,

yielding a higher (harder) repulsive potential between atoms than would be obtained if the electron clouds were allowed to deform. In addition, since a radial density function was utilized and angular dependence was ignored, the resulting potential does not include the directional properties of the Si electronic wave functions. Also, since only the repulsive portion of the potential is calculated, the Si-Si potential must be truncated at the lattice nearest-neighbor distance in order to prevent spontaneous crystal expansion and disintegration. As was stated earlier, the truncation point of the Ar-Si potential must be at a distance greater than 0.75 LU. The truncation distance was chosen to be the same as the nearest-neighbor distance (0.86602 LU).

Figures 9 and 10 show the Si and Ar radial electron densities obtained from the Herman-Skillman program. Figure 11 shows the potentials obtained from the interaction of Ar and Si^{+4} , and from the interaction of Ar^{+1} -Si. The Ar-Si $^{+4}$ interaction was chosen for the model since it is lower at the nearest-neighbor distance. It is not unreasonable to assume that under experimental conditions many of the accelerated Ar ions will be neutralized from the conduction electrons of the metal before collision with the first lattice atom. The silicon atom in the lattice will appear as an ion to the approaching argon atom because of the covalent sharing of its outer shell electrons. Since the potential function in all likelihood is too hard, the choice of a lower potential is reasonable.

Figure 12 shows the selected Si-Si potential. The choice of Si-Si $^{+1}$ was made in order to obtain a potential function which closely approached zero at the equilibrium separation (nearest-neighbor distance) in the lattice.

The potential values obtained were then approximated in a closed analytical form in order that they could be easily

utilized in the sputtering program. Wilson, Haggmark, and Biersack [21] recently reported the approximation of 14 diatomic interactions by the least-squares fitting of the free-electron potential solutions with a Moliere-like potential form:

$$V(r) = (Z_1 Z_2 e^2 / r) \sum_{i=1}^3 C_i \exp(-b_i r / a)$$

where (a) is a screening length and,

$$\sum_{i=1}^3 C_i = 1$$

This method averaged approximately 10% accuracy, and is seen to resemble the method used in the development of this sputtering model.

1. Ar-Si⁺⁺ Interaction Potential

Examination of the Ar-Si⁺⁺ potential plot showed that for a separation distance greater than 0.25 LU, the logarithmic plot was essentially a straight line suggesting a Born-Mayer potential function of the form:

$$V_{BM}(r) = \exp[PEXA + PEXB \cdot r].$$

A least squares fit of the region between 0.25 LU and 0.75 LU (the maximum impact parameter) yielded a value for these exponential coefficients:

$$V_{BM}(r) = \exp[8.40056 - 10.85482r],$$

where V(r) is potential in electron volts and r is separation distance in lattice units. A "peeling" process was then utilized, where the value of the Born-Mayer portion

of the potential was subtracted from each data point. This process revealed that the region of separation less than 0.10916 LU could be represented by a Bohr potential of the form:

$$V(r) - V_{BM}(r) = (1/r) \exp[A + B \cdot r].$$

A least squares fit of the region less than 0.10916 LU yielded the following exponential coefficients:

$$V(r) - V_{BM}(r) = (1/r) \exp[7.16410 - 21.10187r].$$

In order to insure continuity of the analytic form of the potential function and its first derivative with respect to r , a "transition" function was utilized at the cross-over point (0.10916 LU). This transition function proved to be of the Born-Mayer form also:

$$V_D = \exp[10.36930 - 30.13574r].$$

The modeling of the Ar-Si⁴⁺ potential function was complete, yielding a function of the form:

$$V(r) = \begin{cases} (1/r) \exp(7.16410 - 21.10187r) + V_{BM}(r); & r < 0.10196 \text{ LU} \\ \exp(10.36930 - 30.13574r) + V_{BM}(r); & r \geq 0.10196 \text{ LU} \end{cases}$$

Figure 13 is the plot of the analytic model of the potential function and corresponding potential values obtained from the Herman-Skillman and modified Wedepohl programs. The maximum relative error in the analytic potential representation between 0.0 and 0.75 LU occurs at 0.24950 LU, where the analytic model is 7.67% higher than the corresponding computed value. This is caused by the "transition potential" which has not damped out sufficiently

at this point, but which rapidly disappears into the Born-Mayer potential. The potential model obtained was incorporated into the ENERGY subroutine of the basic computer program (Appendix B) as a two-branch potential function with cross-over point at 0.10916 LU and truncation at 0.86602 LU (nearest-neighbor distance).

2. Si-Si⁺¹ Potential Function

Examination of the Si-Si⁺¹ potential values showed that for separation distances above 0.5458 LU the potential function was essentially of the Born-Mayer form:

$$V_{BM}(r) = \exp[EXA + EXB \cdot r].$$

A two variable linear regression yielded the following coefficients:

$$V_{BM}(r) = \exp[6.68394 - 6.94475r],$$

where $V_{BM}(r)$ is in eV, and r is in LU. "Peeling" of this potential from the tabulated values yielded:

$$V(r) - V_{BM}(r) = (1/r) \exp[6.95261 - 15.56752r].$$

Continuity was obtained without the use of a "transition potential" by placing the crossover point at 0.7 LU. Figure 14 shows the analytic form of the Si-Si⁺¹ potential and corresponding Herman-Skillman data points. The relative error in the analytic form of the potential function is less than six percent for all energies less than 10.0 keV.

This potential representation was also incorporated into the ENERGY subroutine (Appendix B), with truncation at the nearest-neighbor distance.

3. Ar-Si⁺ and Si-Si⁺ Force Functions

The force functions were simply determined by obtaining the negative gradients of the potential functions:

$$F(r) = - \partial V(r) / \partial r$$

The problem of an infinite gradient at the potential truncation point was handled as demonstrated by Harrison et al [13]. By utilizing the average force:

$$\langle F_i \rangle = [V(x) - V(R)] / (R - x); R - D < x < R$$

where R is the nearest-neighbor distance and D is the maximum allowed displacement of the most energetic atom in one timestep, the force is gently "turned on" at the nearest-neighbor distance. The value for D which allows both reasonable run times and small energy decrement was found to be 0.075 LU. The two-branch force approximations were incorporated into the program in subroutine STEP (Appendix C).

III. RESULTS

The three lattice orientation models were utilized in computer program runs at 600-eV and 1-keV ion bombardment energies. The (110) orientation model was also utilized in 2-keV ion bombardment programs. The program runs at all energies revealed no large energy decrements from timestep to timestep, leading to the conclusion that the choice of 0.075 LU for D was reasonable. A computer run with D set at 0.1 LU showed a decreased sputtering ratio and a degradation of the ability to maintain energy conservation. The preliminary investigative runs of the silicon model were made utilizing a crystal size of 8x4x8 in the case of the (100) and (111) orientations, and 8x8x8 in the case of the (110) orientation. Each model contained 256 atoms (the (110) orientation generates only 1 atom per lattice site while the (100) and (111) orientation generate two, hence the apparant, but non-real, increase in the lattice size). The mean elapsed computer time required to run a completely compiled and linked load module on the Naval Postgraduate School's IBM 360/67 computer was approximately 160 minutes. The lattice size of 256 atoms did not sufficiently contain all the possible events even at these low ion bombardment energies; however, the size of the lattice was deemed sufficient to test the model while still minimizing computer run times. The sputtering ratios were determined for lattice binding energies of 1 eV to 10 eV in 1-eV increments, and also at 15 eV for each orientation. The mechanisms of sputtering were then traced at active impact points in each orientation.

Prior to the development of the diamond lattice model, work had been done on a fcc model in which the size of the lattice expanded when atoms near the boundaries began to move. The model was developed but was unsuccessful because momentum transfer to the boundary was so rapid that the crystal expanded to maximum size very shortly after ion impact, and no computer time was saved in the simulation. The spread of momentum in a fcc crystal was compared with the spread in the diamond lattice to determine the differences in the momentum spreading mechanism, and to determine the feasibility of an expanding diamond lattice model. The momentum spreading mechanism was found to be different, but the rapid spread of momentum to the boundaries also was observed in the diamond lattice.

Although the investigation of the ion bombardment of silicon is by no means complete, the results obtained indicate that the model is physically reasonable, and further investigation coupled with correlation with experimental data obtained from other sources could prove fruitful in enhancing the understanding of the problems involved in the etching and ion implantation of silicon and germanium semiconductor materials.

A. (100) LATTICE ORIENTATION

Figure 15 shows a roughly isometric projection of the 256 atoms in an 8x4x8 diamond lattice with (100) orientation. This type of projection, first used by Harrison and Delaplain [22], with the distance between layers in the Y direction exaggerated, and the atoms represented by 20° ellipses has proved to be a valuable tool for analyzing the computer programs and for displaying data.

The first atom in the lattice is atom number three, with atom number one being the Ar ion, and atom number two reserved for other projects. Future studies may utilize atom number two as an interstitial atom, surface irregularity (adatom), or the second atom in a diatomic bombarding molecule without disturbing the numbering of the basic crystal. In the display of sputtered atoms and in the tracing of ejection mechanisms, lower planes which were not directly involved in the event were eliminated from the figures, but included in all calculations.

1. 600-eV Results

The complete 41-impact-point, 600-eV simulation utilized 175 minutes of computer time on an 8x4x8 size crystal. With the surface binding energy (ETHR) set at 1 eV, 123 atoms were sputtered yielding a sputtering ratio of 3.00. Figure 16 shows that the low energy sputtering of the (100) orientation is basically a surface event, with 46 of the atoms in the first layer being sputtered, 11 atoms in the second layer being sputtered, and only one sputtering event (atom 149) taking place in the third layer. Atom 149 was ejected with a velocity normal to the crystal face corresponding to a kinetic energy of 1.33 eV, a low energy ejection. All atoms that were sputtered at more than three impact points were contained in the first layer, with atom 32 being sputtered seven times, atom 39 being sputtered eight times, atom 40 being sputtered five times, and atom 55 being sputtered five times. In the lower layers, atom 95 was sputtered three times, and atom 103 was sputtered twice. All other sputtered atoms in the lower layers sputtered only once. Atom 103 is inside the impact area, and atom 95 is directly adjacent to it; thereby receiving large kinetic energies very soon after impact of the ion the lattice.

A plot of the sputtering ratio vs. the surface binding energy was developed in order to gain insight into the value of the surface binding energy. Figure 17 shows the results of this plot for the 600 eV program. The rapid increase in sputtering ratio below 3 eV indicates that the surface binding energy is higher than this value. The more gently sloping decrease in sputtering ratio above 3 eV yields little insight into the value of the binding energy. The sputtering ratio of 0.122 at a binding energy of 15 eV indicates that 5 atoms were ejected with a normal velocity component greater than 13,152 m/sec. The most energetic atom ejected was atom 59, with a normal velocity component of 24,072 m/sec. This occurred when atom 39 was impacted 0.125 LU to the right of its center, and 0.125 LU below center, causing it to move to the upper left edge of the crystal at a high velocity. All sputtering events with energy greater than 15 eV occurred in the first and second layers (four in the first layer, one in the second layer).

The most active impact point in the 600-eV program occurred when atoms 39 and 40 were impacted at point 5025 (impact point displaced 0.50 LU in X direction from the center of atom 39, and 0.25 LU in Z direction, hence 5025). Eight atoms were sputtered at this point. A single-impact program was run at this point with a listing of the positions, velocities, kinetic and potential energies, and forces exerted on each atom which possessed a total energy greater than 0.1 eV. The listing was printed once every five timesteps. The atom motions which caused the eight atoms to be sputtered were traced in order to gain insight into the sputtering mechanisms involved in the (100) diamond lattice orientation. The advantage of computer simulation in which each atom is uniquely identified is evident in the following mechanism summary.

a. Mechanism Summary

Atoms 7,9,15,18,32,57,65, and 119 were sputtered as a result of an ion impact at impact point 5025. Atom 57 was sputtered at timestep 100, atom 65 at timestep 105, atoms 7,9, and 15 at timestep 110, atom 18 at timestep 115, and atom 32 was sputtered at timestep 130. Each sputtered atom was followed separately, and the individual traces are illustrated in Figure 18.

(1) Atom 32. The impacting Ar ion (atom 1) traveled into the second crystal layer after striking atom 40. At timestep 20, atom 1 passed within 0.508 LU of atom 103, causing 103 to move in the positive X direction. As atom 103 moved below atom 32, it forced 32 upward. Atoms 31 and 41 moved upward and away from atom 32 as it was still gaining velocity from atom 103. At timestep 45, atom 103 reached its point of closest approach with atom 32. As a result of the 32-103 collision, atom 32 gained an upward velocity (having been slowed slightly by grazing collisions with 31 and 41). At timestep 60 atoms 32 and 103 were no longer interacting, and atom 32 had risen 0.118 LU. Atom 32 continued to rise, interacting with no other atoms until timestep 125. At that time atom 32 interacted with atom 25 which was rising with a low velocity as a result of atom movement below it. This slight interaction slowed atom 25, but raised atom 32's normal velocity component. At timestep 130, atoms 25 and 32 were no longer interacting, and atom 32 continued to rise with no further interactions. The mechanism observed in the sputtering of atom 32 was the grazing collision with a lower atom in the basic tetrahedron composed of atoms 31,32,41,97, and 103. The velocity imparted to atom 103 (roughly parallel to the X,Z plane) resulted in the rising of the center and upper atoms in the

tetrahedron. Atom 32, however, was the only atom possessing a high enough normal velocity component to be counted as a sput. This may not always be the case in higher energy bombardments.

(2) Atom 15. Atom 1 in its passage through the second layer also interacted with atom 96, causing it to move in the Z direction with a velocity component of -29,516 m/sec while traveling downward at 6715 m/sec. The atoms below 96 slowed its downward velocity slightly. At timestep 60 atom 80 was struck by atom 96, which caused atom 80 to rise rapidly. As 96 continued to pass under 80, it imparted a high negative Z velocity component to 80. Atom 80 then rose under atom 15. Atom 15 interacted with no other atom, quickly gained a Y velocity component of -7838 m/sec and was counted as sputtered at timestep 110. Here a mechanism similar to the **scoop** or **squeeze** mechanism in fcc copper described by Harrison et al [12] took place in the second layer, causing a surface atom to be sputtered.

(3) Atom 9. After collision with atom 15, atom 80 was deflected below atom 9, reaching the point of closest approach at timestep 100. By timestep 105, atoms 80 and 9 were no longer interacting and atom 9 rose from the surface with a normal velocity component of -9311 m/sec, interacting with no other atom. At timestep 110, atom 9 was also counted as a sput. This event was also a result of the **scoop** or **squeeze** mechanism in the second layer. Atom 80 was deflected upward by atom 10, and also rose from the surface with a velocity slightly too small to be considered a sputtered atom. This illustrates a case of a second layer atom rising from the surface through a vacancy created by impact from lower layers, and it is reasonable to assume that at other times this occurrence causes sputtering.

(4) Atom 7. As atom 80 rose under atom 15, it also interacted with atom 8, reaching the point of closest approach at timestep 80. Atom 8 traveled in the negative X and Z directions while rising into collision with atom 7. The motion of atom 8, which was approximately at an angle of 45° with the normal to the surface, caused atom 7 to be accelerated in the same direction. At timestep 100, atom 7 no longer interacted with the greatly slowed atom 8, but rose from the surface with an X velocity of -4893 m/sec, a Y velocity of -4559 m/sec, and a Z velocity of -4338 m/sec. At timestep 110, atom 7 was also counted as a sput. The **scoop** or **squeeze** mechanism in the second layer caused the center atom in tetrahedron 7,8,15,71,79 to impart momentum to its upper atom at an angle similar to the **deep** mechanism described by Harrison et al [12]; however, the mechanism is unique to the diamond lattice where the spread of momentum through the tetrahedral atoms occurs at all depths, and seemingly in all directions.

(5) Atom 18. After traveling under atom 9, atom 80 collided with atom 10 at timestep 80, and then rose upward from the surface. Atom 10 passed under atom 17, causing it to rise at a velocity too low to be considered a sputtered atom, and then passed below atom 18 at a distance of 0.803 LU, imparting a velocity of 1891 m/sec in the X direction, -2359 m/sec in the Y direction, and 3389 m/sec in the Z direction to atom 18. Atom 18 then crossed the vacancy between it and atom 34, colliding with atom 34 at timestep 150. As atom 18 passed above 34, its normal velocity component was increased to -3689 m/sec, while its Z component was reversed to 375 m/sec. At timestep 155, atom 18 was counted as a sputtered atom, also having been sputtered by the second-layer mechanism affecting the motion of atom 80.

(6) Atom 119. Atom 1 struck atom 40 as it entered the crystal, driving atom 40 downward into collision with atoms 112 and 119. Atom 119 was then driven toward atom 120, and at timestep 50 was driven upward by the combination of interactions with atoms 40 and 120. At timestep 70, atom 119 was no longer interacting with atoms 40 and 120, but was deflected upward further by atom 129, and was deflected in the negative X and positive Z directions by collision with atoms 57 and 58. At timestep 90, atom 119 was interacting with no other atoms, and was traveling with an X velocity of -2149 m/sec, a Y velocity of -4215 m/sec, and a Z velocity of 3460 m/sec. At timestep 105, atom 119 collided with atom 64, reversing its X velocity and slowing its negative Y velocity. By timestep 115, atom 119 had risen to 0.157 LU above the surface, and was interacting with no other atom. At timestep 130, atom 119 was counted as a sputtered atom, possessing a normal velocity component of -3035 m/sec. Again the **squeeze** mechanism caused an atom to rise from the second layer and, in this case, move into the (100) channel formed by atoms 57, 58, 119, and 120, be reflected out of the the channel and rise due to a secondary collision with another surface atom.

(7) Atom 57. Atom 119 while rising to the surface, collided with atoms 57 and 58 at timestep 70. At timestep 75, atom 119 passed within 0.762 LU of atom 57 causing it to rise from the surface. At timestep 90, atom 57 was no longer interacting with atom 119, and possessed a normal velocity component of -4312 m/sec. Atom 57 continued to rise, interacting with no other atoms, and was counted as a sputtered atom at timestep 100. Again the **squeeze** mechanism in the second layer resulted in the sputtering of a surface atom.

(8) Atom 65. The collision of atom 119 with atom 58 resulted in the passing of atom 58 below atom 65 at a distance of 0.748 LU at timestep 85. By timestep 95, atom 65 was no longer interacting with atom 58, and continued to rise with no further interactions until being counted as a sputtered atom at timestep 105. Atom 65 possessed a normal velocity component of -4185 m/sec after interaction with atom 58. Once again the squeeze mechanism in the second layer, combined with momentum coupling in tetrahedron 57,58,65,121,129 caused a surface sputtering event.

During the trace of the sputtering mechanisms at 600 eV, the third and fourth layers never contributed an active atom to the sputtering mechanism; however, these layers are essential to the mechanism since the coupling of momentum in the Y direction through the tetrahedra allows the squeeze mechanism to occur without driving the "squeezed" atom downward. The rising of two atoms from the second layer was responsible for seven of the eight sputtering events observed, and one event was caused by the lateral movement of a second layer atom.

2. 1000-eV Results

The complete 41-impact-point simulation program run with bombarding ion energy of 1 keV required 183 minutes of computer time. The sputtering ratio obtained with the surface binding energy set at 1 eV was 3.415, with 140 atoms being sputtered. Figure 19 shows the atoms sputtered at this energy. The higher energy bombardment caused an increase in the number of atoms sputtered in the second and third layers and caused a fourth-layer atom (atom 225) to be sputtered. This indicates that higher energy simulations must not only increase the lattice size in the X and Z

directions, but must add more crystal layers in the Y direction in order to adequately contain all sputtering events. Atom 225 was sputtered with an X velocity component of only 29 m/sec, and a Z velocity component of 86 mSec, while the normal velocity component was -3681 mSec. Investigation of this type event may show that the atom in fact transited a (100) channel while rising to the surface. A normal velocity component of 3861 m/sec corresponds to a kinetic energy of 2.2 eV, a low energy sputtering event, which may be below the final value determined for the surface binding energy by further studies. Figure 20 shows the plot of the 1000 eV sputtering ratio vs. surface binding energy. Again the rapid rise of the sputtering ratio below 3 eV was observed, suggesting a binding energy above this value. This would then eliminate many of the lower layer sputtering events.

3. 600-eV and 1000-eV Comparison

Figure 21 shows the comparison of the 1000-eV and 600-eV sputtering ratios plotted vs. surface binding energy. The 1000-eV simulation proved to have a higher sputtering ratio at each value of ETHR as might be expected, but the values of the sputtering ratios closely approached each other above a binding energy of 8 eV. Above this point only the highest energy sputtering events are counted, and it is reasonable to assume the value of ETHR is below the point where the sputtering ratios converge.

B. (110) LATTICE ORIENTATION

The (110) lattice orientation proved very interesting because the sputtering ratio decreased as the bombarding ion

energy increased. For this reason, mechanism traces were performed not only at 600 eV and 1 keV, but also at 2 keV. Because the (110) orientation is a much more open lattice than the (100) orientation, it was expected that the sputtering ratio of the (110) orientation would be lower than that of the (100) orientation. This was confirmed at both 600 eV and at 1 keV.

Figure 22 shows the isometric projection and numbering sequence of the (110) lattice. As was stated earlier, an 8x8x8 (110) lattice was utilized in the computer simulation, but all eight half-layers are not included in the figure in the interests of legibility of the numbering scheme.

1. 600-eV Results

The 600-eV simulation of the (110) orientation utilized 139 minutes of computer time to complete 30 impact points. Shots which did not place the ion near the channel center required approximately the same number of timesteps as the (100) orientation computer simulation, while shots in which the bombarding ion transited the channel typically required fewer timesteps. The 600-eV simulation caused 60 atoms to sputter resulting in a sputtering ratio of 2.00 for a surface binding energy of 1 eV. Figure 23 shows the sputtered atoms for the 600-eV simulation. Again, most sputtering events took place in the first layer, with atom 95 being the only multiply sputtered atom in the second layer.

Figure 24 shows the plot of sputtering ratio vs. ETHR for 600-eV simulation. The sputtering ratio rises rapidly below the value of 5 eV for the surface binding energy, and reaches a plateau value of 0.233 for binding energies of 7, 8, and 9 eV. Four atoms were ejected with

normal velocity components corresponding to an energy of 15 eV or greater, the most energetic ejection being atom 95 which was ejected with a normal velocity component of -15,131 m/sec when atom 23 was impacted at its center by the bombarding ion. The ratios of Y and Z velocities of atom 95 indicate that it rose 1.81 LU while transiting 0.63 LU in the positive Z direction. Atom 95 then rose to the surface in the channel formed by atoms 30,31,32,61, and 63. The (110) channels, therefore, were observed to allow the escape of lower atoms with high energies, while focusing their ejections in a near-normal direction. Atom 23, the next most energetic ejection was studied in the mechanism trace performed at the most active impact point.

a. Mechanism Summary

The most active impact point in the 600 eV simulation occurred where the ion struck atom 23 at a point 0.141 LU to the right of center and 0.2 LU above center in the positive Z direction. The single-shot simulation required 334 seconds of computer time. Atoms 4,14,18,23,48, and 61 were sputtered. Figure 25 illustrates the mechanisms described in the individual atom traces.

(1) Atom 23. The Ar ion collided with atom 23 at timestep 1 and imparted negative X and Z velocity to it while driving it downward. At timestep 20, atom 23 reached its point of closest approach to atom 46, passing above it at a distance of 0.54 LU. A brief interaction with atom 46 slowed atom 23's positive Y velocity slightly. Atom 23 continued downward and in the negative X and Z direction, and by timestep 35 had reached its closest point of approach with atom 45. The collision with atom 45 reversed the descent of atom 23, while interactions with atoms 14 and 44 prevented direction changes in the Z direction. At timestep

60, atom 23 was no longer interacting with atoms 45, 14, or 44, but was interacting only with atom 12. The collision with atom 12 slowed atom 23's velocity in the negative X direction, reversed its negative Z velocity, and accelerated it in the negative Y direction. At timestep 80, atom 23 was counted as a sputtered atom. At that time, atom 23 was still interacting with atom 12, but the computer simulation ceased accelerating the atom because it had already risen 0.4 LU above the surface. The high energy ejection of atom 23 was a purely surface event, with the impacted atom traveling a large distance across the surface because of the vacancies created by the (110) channels. This large lateral displacement is not possible in close packed orientations.

(2) Atom 14. Atom 23, while rebounding from atom 45, passed within 0.618 LU of atom 14. The interaction of atom 23 and atom 14 caused 14 to rise with a velocity of -1013 m/sec. At timestep 50, atom 14 was squeezed between atoms 23 and 15, slowing its velocity in the negative Y direction. Atom 14 then continued to rise, and at timestep 60 was interacting with no other atoms. The normal velocity of atom 14 at that time was -1421 m/sec, insufficient to cause sputtering. At timestep 120, atom 45, which was recoiling upward as a result of its previous impact by atom 23, overtook the slowly rising atom 14. The resultant collision slowed atom 45, but increased the normal component of atom 14. At timestep 125 then, atom 14 was no longer interacting with atom 45, and was counted as a sputtered atom with a normal velocity component of -3600 m/sec. The **squeeze** mechanism described by Harrison et al [12] was the primary mechanism responsible for this surface sputtering event.

(3) Atom 4. Atom 45, after being struck by atom 23, moved downward under atom 14. At timestep 70, atom 45 began interaction with atom 36, accelerating 36 upward

and in the negative X and Z directions. At timestep 80, atom 45 reached its closest point of approach to atom 36 and began to recoil back under atom 14. Atom 36 was deflected slightly by atom 35, and by timestep 110 had moved into interaction with atom 4. Atom 4 was accelerated upward by the interaction with atom 36, and was squeezed slightly by interaction with atom 3 at timestep 115. By timestep 125, atom 4 was interacting with no other atoms, and was rising with a normal velocity component of -2674 m/sec. At timestep 140, atom 4 was counted as a sputtered atom. The primary mechanism involved was the mole mechanism described by Harrison et al [12]. This is distinguished from the scoop or squeeze mechanism by the low angle at which the approaching atom strikes the sputtered atom.

(4) Atom 48. Atom 1, after striking atom 23, continued into the second layer. Interaction with atoms 118, 119, and 88 deflected atom 1 into the (110) channel as it passed through the second layer. At timestep 30, atom 1 reached its closest point of approach to atom 88, passing within 0.406 LU and accelerating atom 88 downward into collision with the lower part of atom 89. By timestep 45, atoms 88 and 89 reached the point of closest approach and atom 89 had acquired a Y velocity component of -1309 m/sec. At timestep 45, atom 89 was also interacting slightly with atom 90, and was being deflected in the positive Z direction by atom 48. Atom 89 caused atom 48 to rise from the crystal. By timestep 80, atom 48 was no longer interacting with any other atom, and at timestep 145 it was counted as a sputtered atom with a normal velocity component of -3400 m/sec. The mechanism involved was primarily the deep mechanism.

(5) Atom 18. After being deflected by atom 48, atom 89 collided with the underside of atom 49. Atom 49 then rose in the lattice pushing atom 18 upward from the

surface. At timestep 100, atoms 49 and 18 reached the closest point of approach, their separation being 0.852 LU. At timestep 105, atom 18 had acquired a normal velocity component of -3064 m/sec, and was 0.156 LU above the lattice surface. Atom 18 continued to rise without any other interactions, and was counted as a sputtered atom at timestep 125. The primary mechanism was again the deep mechanism caused by the rising of atom 89 from the second layer.

(6) Atom 61. Atom 1, when transiting the second layer, caused the outward movement of atoms 118, 119, and 83. Atom 118 moved under atom 95, and at timestep 70, collided with atom 94. Atom 94 moved upward, and while still interacting with atom 118, caused atom 61 to rise from the surface. At timestep 90, atom 94 had reached a maximum upward velocity of -3106 m/sec, and atom 61 had reached an upward velocity of -1663 m/sec. By timestep 110, the coupling of momentum from atom 118 through 94 to atom 61 was complete, with atom 61 rising at -4071 m/sec, and atom 94 having slowed to -731 m/sec. Atom 61 continued to rise with no further interactions, and was counted as a sputtered atom at timestep 145. The mechanism was the deep mechanism caused by atom 94.

Six sputtering events occurred at this impact point; three sputtering events were the result of the deep mechanism, two sputtering events were surface events characterized by the squeeze or mole mechanism, and the most energetic event was characterized by a mechanism not seen in the more close-packed lattice orientations. This large lateral displacement followed by one or more surface reflections can perhaps best be described as a skip mechanism. The other two surface mechanisms observed (the sputtering of atoms 4 and 14) were the indirect result of the "skipping" of atom 23.

2. 1000-eV Results

The 30-impact-point, 1-keV simulation program required 141 minutes of computer time, two minutes longer than the 600 eV simulation. With the binding energy set at 1 eV, 56 atoms were sputtered, resulting in a sputtering ratio of 1.866. The lower sputtering ratio was unexpected at a bombarding energy of 1 keV; therefore, the mechanisms of sputtering were again traced at the same impact point that was examined at 600 eV. Figure 26 shows the atoms sputtered in the 1-keV simulation. At 1 keV, the sputtering was again primarily a surface phenomenon, with only three single sputs occurring in the second layer, and no atoms being sputtered from any layer lower than the second. The 1-keV simulation caused the sputtering of five boundary atoms, while the 600-eV simulation sputtered four atoms on the surface layer boundary. Only two atoms were ejected with normal velocity components corresponding to kinetic energies greater than 15 eV, as compared with 4 high energy ejections in the 600-eV simulation. At impact point 0 (dead center of atom 23), atom 95 was ejected with a normal velocity component of -16,296 m/sec. Atom 95 was ejected through the same channel as it was in the 600-eV simulation. Figure 27 shows the plot of sputtering ratio vs. ETHR for the 1 keV simulation. Again, a rapid rise in the sputtering ratio was observed below 3 eV. The decrease between 4 eV and 8 eV, however, was not as gently sloping as the 600-eV run. The sputtering ratio continued to drop fairly rapidly until 9 eV, at which point only the two highest-energy atoms were sputtered.

a. Mechanism Summary

The 1-keV single-impact-point program required 339 seconds of computer time, 5 seconds longer than the 600 eV simulation. Atoms 14,18,23,48, and 65 were sputtered, a decrease of 1 atom from the 600 eV simulation. Two atoms (atoms 4 and 61) which were sputtered at 600 eV, were not sputtered at 1 keV. Atom 65 was sputtered at 1 keV, but not in the lower-energy simulation. The mechanism trace was performed and compared at each step with the corresponding 600-eV program. Figure 28 illustrates the individual atom traces.

(1) Atom 23. At timestep 1, atom 23 was impacted 0.141 LU to the right of center and 0.2 LU above center in the Z direction. The impact drove atom 23 downward, and in the negative X and Z directions. Atom 23 was deflected slightly by atom 46, and at timestep 45 had been deflected upward by atom 45. At timestep 70, atom 23 was interacting with atoms 12 and 13, striking slightly below these atoms. At timestep 80, atom 23 reached the closest point of approach to atom 12, and was deflected upward in a nearly normal direction. Atom 12 continued upward, interacting primarily with atom 12, and at timestep 100 had passed upward out of interaction range with any atom. Atom 23 continued upward with a normal velocity component of -7500 m/sec and nearly zero X and Z velocities and was counted as a sputtered atom at timestep 120. The **skip** mechanism again caused the sputtering of atom 23, as it did in the 600 eV simulation; however, atom 23 was not deflected upward as much by atom 45 and therefore impacted slightly below atom 12 and 13, slowing its normal velocity component rather than accelerating it as was the case in the 600 eV simulation.

(2) Atom 14. Atom 23, while rebounding from atom 45, passed within 0.601 LU of atom 14. The interaction of atom 14 and 23, combined with slight recoils from atoms 13 and 15, caused atom 14 to rise from the lattice. Atom 14 continued to rise, and at timestep 105 was interacting with no other atoms. At timestep 115, atom 14 was counted as a sputtered atom. Atom 14 possessed a normal velocity component of -4491 m/sec at that time. Once again the **scoop** or **squeeze** mechanism was responsible for a surface sputtering event. In this case 14 was not impacted by atom 45 after being squeezed by atom 23, but received sufficient velocity from the primary mechanism itself. After being driven downward by atom 23, atom 45 came to rest 0.711 LU below its initial position.

(3) Atom 48. Atom 1, after striking atom 23, continued into the second layer. At timestep 30, atom 1 impacted atom 88, causing atom 88 to move in the positive X direction underneath atom 89. At timestep 45, atom 89 started to rise from the second layer, and by timestep 50 atom 89 was accelerating atom 48 upward. At timestep 70, atom 89 reached its closest point of approach to atom 48, rising to within 0.765 LU. Atom 89 was slowed by atom 48, and by timestep 95 was traveling downward toward its initial position. Atom 48 continued to rise, interacting slightly with atom 47, and pushing atom 25 upward at a velocity too low to cause it to sputter. By timestep 95, atom 48 was interacting with no other atom and was rising with a normal velocity component of -3552 m/sec. At timestep 155, atom 48 had risen 0.418 LU above the surface and was counted as a sputtered atom. The mechanism involved was essentially the same **deep** mechanism involved in the sputtering of atom 48 during the 600-eV simulation. The only difference was that atom 88 was impacted more directly by atom 1, because the

higher energy possessed by the Ar ion prevented its deflection into the (110) channel.

(4) Atom 18. At timestep 90, atom 89 after being deflected by its collision with atom 48, interacted with atom 49. At timestep 100, atom 49 having been accelerated in the positive X and negative Z directions, rose under atom 18. At timestep 120, atom 49 was at its closest point of approach to atom 18, passing under atom 18 at a distance of 0.836 LU. Atom 18 rose without interacting with any other atom, and at timestep 125 possessed zero potential energy. At timestep 135, atom 18 was counted as a sputtered atom, possessing a normal velocity component of -4230 m/sec. The primary mechanism involved was the **deep mechanism** caused by the rising of atom 89 from the second layer, just as was the case in the 600-eV sputtering event.

(5) Atom 65. Atom 1, when colliding with atom 88 in second layer, also interacted with atom 119, accelerating it in the positive X and Z direction and driving it downward. At timestep 45, atom 119 moved within interaction range with atom 120, accelerating atom 120 in the positive X and Z direction with a virtually negligible Y velocity component. At timestep 65, atom 120 interacted not only with atom 119, but experienced grazing collisions with atoms 97, 121, and 161 (atom 161 is located directly below atom 97 in the fourth layer). Atom 120 was focused then into collision with atom 98, and was within interaction range at timestep 100. At timestep 100, atom 119 had recoiled slightly, and was no longer interacting with atom 120. Atom 120 was rising slightly as a result of its collision with atom 161, and rose underneath atom 98. Atom 98 then rose toward the first layer, and at timestep 115 began interacting with atom 65. Atom 65 rose from the surface interacting with only atom 98. At timestep 130, atom 65 had acquired a normal velocity component of -3246

m/sec, and was interacting with no other atoms. At timestep 130, atom 65 reached a height of 0.499 LU above the surface and was counted as a sputtered atom. Atom 65 was sputtered by the deep mechanism. Essentially the same mechanism occurred in the 600 eV simulation, but the lower energy Ar ion was deflected into the (110) channel and therefore did not transfer sufficient momentum to atom 119. Atom 98 did, in fact, rise at a much lower velocity causing atom 65 to rise. At program termination, however, atom 65 was rising with a normal velocity component of -877 m/sec and was still 0.2 LU below the lattice surface.

Atoms 61 and 4 were sputtered in the 600-eV simulation, but not in the 1-keV simulation. Atom 4 was not sputtered because atom 45 was driven deeper into the crystal, and came to rest in a lower layer, rather than recoiling into atom 13 as it did in the 600-eV simulation (Fig. 25). Atom 61 was not sputtered because the Ar ion was not deflected into the (110) channel. Atom 118, therefore, did not achieve a high outward velocity. In the 1-keV simulation, atom 118 moved into the vacancy left by atom 119 rather than in the negative X direction. Atom 94 never possessed sufficient energy to be listed.

3. 2000-eV Results

The 2-keV 30-impact-point program required 135 minutes of computer time, 4 minutes less than the 600 eV simulation. With ETHR set at 1 eV, 44 atoms were sputtered, resulting in a sputtering ratio of 1.467. This sputtering ratio was lower than the sputtering ratio obtained in the 1-keV simulation. Figure 29 shows the sputtered atoms obtained at 1 eV binding energy. Once again, the sputtering was observed to be predominantly a surface phenomenon, with two sputtering events occurring in the second layer (atoms 95

and 127), and a single sputtering event occurring in the fourth layer (atom 223). Two high energy ejections were observed, occurring at the same impact points as the high energy ejections in the 1-keV program. Atom 95 was ejected with a normal velocity component of -16,020 m/sec, 176 m/sec slower than the 1 keV event, and atom 63 was ejected at -17,835 m/sec, 2,353 m/sec more than the 1-keV event. Atom 95 again exited the surface through the (110) channel, as it did in the two lower-energy simulations. Atom 223, the fourth-layer sputtering event also exited the surface through the same (110) channel. Only two boundary atoms were sputtered in the surface layer, as compared to five in the 1-keV simulation, and four in the 600-eV simulations; however, the sputtering of a fourth-layer atom showed that not only must the crystal be expanded in the X and Z directions, but more layers must be added if containment of the events is to be achieved. The fourth-layer sput occurred at an energy of 2.88 eV, again a relatively low energy sputtering event. Figure 30 shows the plot of sputtering ratio vs. surface binding energy. The rapid rise of sputtering ratio below 3 eV is again evident, and a plateau value of 0.133 is reached at 8 and 9 eV, similar to the 1-keV case. A surface binding energy above the 3-eV point would eliminate the lower-layer sputtering event.

a. Mechanism Summary

The 2-keV single-shot simulation required 369 seconds of computer time, 30 seconds longer than the 1 keV simulation. Five first-layer atoms were sputtered, the same number as in the 1 keV simulation; however, atoms 23, 48, and 65 were not sputtered at 2 keV, and atoms 4, 12, and 13 were sputtered instead, indicating another change of the predominant mechanisms. The traces of the atoms are illustrated in figure 31. The trace of atom 23, which was

sputtered by the skip mechanism in both the 600-eV and 1-keV simulations, but not sputtered in the 2-keV simulation is also included.

(1) Atom 23. At timestep 1, atom 23 was impacted by the Ar ion. Atom 23 moved over atom 46 and collided with atom 45 moving atom 45 downward into the crystal. Atom 23 then rebounded from atom 45, and struck atoms 12 and 13 much as it did in the 600-eV and 1-keV programs; however, atom 23 struck below these two atoms and was deflected downward. Atom 23 was deflected further downward by collision with atom 35, and continued down into the second layer. At timestep 160, atom 23 exited the crystal at its left side while traveling between the second and third layers, carrying with it 21.29 eV of kinetic energy after having lost 116.44 eV of its initial kinetic energy by collisions within the lattice. The skip mechanism seems, then, to be energy dependent. At higher energies the "skipping" atom causes too much surface damage when colliding with surface atoms, therefore moving into the crystal rather than rebounding across its surface. The absence of this mechanism at higher energies could, in part at least, account for the decreased sputtering ratio at higher energies.

(2) Atom 14. At timestep 50, atom 23, while still traveling downward over atom 45, began interacting with atom 14. Atom 14 was forced upward from the lattice by this interaction. At timestep 75, atom 23 reached its point of closest approach to atom 14, passing below it at a distance of 0.513 LU. At the same time atom 14 experienced grazing collisions with atoms 13 and 15, deflecting it upward even further. At timestep 110, atom 14 had risen 0.40 LU above the surface. Although it was still interacting with atom 23, it was counted as a sputtered atom. The mechanism which caused atom 14 to sputter was no

longer predominantly the **squeeze** or **scoop** mechanism, but could be classified as the **mole** mechanism because of the lower impact on atom 14.

(3) Atom 13. At timestep 75, atom 14 interacted with atom 13 causing it to move -0.007 LU in the X direction, and -0.006 LU in the Z direction, while rising -0.004 LU. Atom 13 continued to move in the negative X, Y, and Z directions at a very low velocity until atom 23 began interaction with it. At timestep 100 atom 13 was passed by atom 23 at a distance of 0.621 LU. At the closest point of approach, atom 23 was 0.171 LU below atom 13, thereby accelerating atom 13 upward from the surface. Atom 13 continued to rise, interacting with no other atoms, and at timestep 130 was counted as a sputtered atom. The low impact of atom 23 on atom 13 classifies this as a mole mechanism also.

(4) Atom 12. After passing atoms 14 and 13, atom 23 collided with the underside of atom 12 and was sharply deflected downward. Atom 23 moved into interaction range with atom 12 at timestep 100, and reached its closest point of approach at timestep 105, passing under atom 12 at a distance of 0.508 LU. Atom 12 was accelerated in the X direction to a velocity of -16,863 m/sec, and upward with a velocity of -10,307 m/sec. At timestep 115, atom 12 was no longer interacting with any atom, and it was counted as a sputtered atom. Once again a surface atom was sputtered by the mole mechanism.

(5) Atom 4. After being deflected downward by atom 12, atom 23 continued in the negative X direction and at timestep 120 moved into interaction range with atom 35. At timestep 125, atom 23 reached its closest point of approach to atom 35, accelerating it upward into collision with atom 4. Atom 4 rose from the lattice interacting with

no other atom, and at timestep 140 had moved out of interaction range with atom 35. At timestep 150, atom 4 was counted as a sputtered atom, possessing a normal velocity component of $-3,111$ m/sec. The mole mechanism caused the transfer of momentum from the center atom of the incomplete tetrahedron 4,35,36, and 68 to the upper atom (atom 4), causing another surface sputtering event. Atom 4 was not sputtered in the 1-keV simulation, but was sputtered in the 600-eV simulation. In the 600 eV simulation, however, the recoil of atom 45 caused atom 36 to impact atom 4 and raise it from the surface. In the 2-keV case, a totally different interaction chain was involved.

(6) Atom 18. After striking atom 23, atom 1 moved into the second layer striking atom 88. Atom 88 traveled in the positive X direction and rose from its position in the second layer, forcing atom 89 downward and in the positive X direction. At timestep 80, atom 89 interacted with atom 48, causing it to rise slowly from the crystal surface. Atom 89 also recoiled from atom 112, and rose, interacting with atom 49 at timestep 130. At timestep 135, atom 18 was lifted from the crystal surface by the rising atom 49, and interacted briefly with atom 17, which was moving as the result of a collision with atom 15. At timestep 140, atom 18 was interacting only with atom 49. At timestep 145, atom 18 was interacting with no other atoms and was rising from the crystal with a normal velocity component corresponding to a kinetic energy of 1.01 eV. At timestep 160, atom 18 was counted as a sputtered atom. The mechanism was again the deep mechanism caused by the rising of atom 89 from the second layer.

In both the 600-eV and 1-keV simulations, atom 48 was sputtered by the deep mechanism caused by the rising of atom 89. In the 2 keV simulation, however, atom 88 rose above atom 89 rather than squeezing it upward, and

atom 89 rose as the result of recoil from atom 112. This lower energy rebound did not accelerate atom 48 sufficiently to cause it to be counted as a sputtered atom. In the 1-keV simulation, atom 65 was sputtered by atom 98 as it rose from the second layer. In the 2-keV simulation, atom 119 was not impacted by atom 1, and remained essentially at rest in the crystal; therefore, atom 120 did not transfer a significant amount of energy to atom 98.

Although atom 65 did rise slightly, it was still below the crystal surface at program termination.

4. Comparison

A comparison of the sputtering ratios vs. ETHR for each bombarding energy yielded no insight into the value for surface binding energy of the (110) orientation of silicon. Figure 31 shows that for a binding energy below 3-eV, the sputtering ratios of the 600-eV program were higher than the 1-keV or 2-keV programs. Between 3 eV and 7 eV, the 1-keV program possessed the highest sputtering ratios, and between 8 eV and 15 eV, the 600 eV sputtering ratios were again the highest. At a binding energy of 7 eV, all three programs displayed the same sputtering ratio. Comparison of the mechanism traces showed that the skip mechanism probably occurs only at low bombarding energies, and also that as bombarding energy increases, surface damage caused by driving surface atoms deeper into the crystal decreases the number of surface sputtering events.

C. (111) LATTICE ORIENTATION

The (111) lattice orientation, being a more open orientation than the (100), was expected to have a lower

sputtering ratio at corresponding energies. This was confirmed at both 600 eV and 1 keV. The sputtering ratio at 1 keV was higher than the sputtering ratio at 600 eV, showing that the unexpected results encountered in the (110) orientation were not duplicated in the (111) orientation. Figure 33 shows isometric projection of the (111) orientation. The fourth layer is a duplicate of the first, and was eliminated from the figure in the interest of legibility.

1. 600-eV Results

The complete 36-impact-point 600-eV simulation required 139 minutes of computer time. With the binding energy set at 1 eV, 51 atoms were sputtered yielding a sputtering ratio of 1.417. All sputtered atoms were located in the first three layers, with four multiple and three single sputts originating in the second layer, and three single sputtering events originating in the third layer (Fig. 34). Nine atoms located on the X and Z boundaries were sputtered, indicating that the lattice dimensions were too small to sufficiently contain all events at 600 eV. Four atoms were ejected at energies greater than 15 eV. Three of the high energy ejections were surface layer events (atoms 24,27,59), and one ejection (atom 171) originated in the third layer. Atom 171 was sputtered from the third layer with a normal velocity component corresponding to 28 eV, indicating that the open lattice allows channeling of these third layer atoms to the surface without experiencing hard collisions enroute.

Figure 35 shows the plot of the 600-eV sputtering ratio vs. ETHR. Again, the rapid rise of the sputtering ratio below 3 eV was observed, suggesting that the binding energy is above 3 eV.

a. Mechanism Summary

A five-minute, single-impact-point program was run with 600-eV bombarding energy, and the impact point displaced 0.141 LU from the impact atom center in the X direction and 0.133 LU from the atom center in the Z direction. At this active impact point, six atoms were sputtered from the surface layer, and two atoms were sputtered from the second layer. Figure 36 illustrates traces of the atoms listed separately in the summary.

(1) Atom 30. At timestep 1, atom 39 was impacted by the Ar ion. Atom 39 moved downward while traveling in the negative X and Z directions, and at timestep 25 moved into interaction range with atom 30. Atom 30 was accelerated downward at 13,328 m/sec, and at timestep 35, collided with atom 85. Atom 30 recoiled upward from atom 85 and rose beneath atom 24. At timestep 65, atom 30 passed within 0.651 LU of atom 24 and was deflected in the positive Z direction. After passing beneath atom 24, atom 30 collided with atom 32 and was deflected upward. At timestep 95, the rapidly rising atom 30 interacted with atom 31, causing its normal velocity component to be slowed from -5729 m/sec to -4405 m/sec. At timestep 110, a brief interaction with atom 23 further slowed atom 30's normal velocity component to -2845 m/sec. At timestep 125, atom 30 had risen 0.119 LU above the lattice surface, and was interacting with no other atoms. At timestep 140, atom 30 was counted as a sputtered atom. This interaction was the result of a second-layer reflection, the only pure reflection observed in the mechanism traces performed.

The placement of the atoms in the second and third layers with "pseudo-channels" to the surface makes this type of event more probable in the (111) orientation than in the (100) or (110) orientations.

(2) Atom 24. Atom 30, while rising to the surface, began interaction with atom 24 at timestep 55. Atom 30 passed below atom 24 at a distance of 0.651 LU, accelerating it in the negative Y direction. Atom 24 was also accelerated in the positive X and negative Z directions by atom 30, and at timestep 95 it was slowed by collision with atom 16. At timestep 105, atom 24 interacted with both atoms 15 and 16, and was deflected toward atoms 25 and 26. The interaction with atoms 25 and 26 at timestep 120 slowed atom 24's normal velocity component to -2071 m/sec, reducing its energy below the 1 eV required to sputter. At timestep 130, atom 24 was still 0.173 LU below the surface, and its normal velocity component had fallen to -1255 m/sec. At timestep 155, atom 79 rose under atom 24 as the result of impact by atom 85. Atom 74 accelerated atom 24 upward, and by timestep 160 atom 24 was interacting with no other atom and was rising with sufficient energy to be counted as a sputtered atom. At timestep 165, atom 24 was counted as a sputtered atom. The primary mechanism which caused atom 24 to sputter was the **deep** mechanism caused by atom 79 rising from the second layer. This was assisted by the reflection of atom 30 from the second layer.

(3) Atom 31. Atom 30, after passing below atom 24, was deflected upward by atom 32. At timestep 95, atom 30 began interaction with atom 31. Atom 31 rose from the surface, and by timestep 110 was no longer interacting with atom 30. At timestep 120, atom 31 was counted as a sputtered atom. This event was also the result of the **deep** mechanism.

(4) Atom 25. At timestep 120, atom 24 was slowed by atom 25. The interaction with atom 24 caused atom 25 to rise from the crystal surface. At timestep 130, atom 25 had risen 0.292 LU above the lattice surface and was no longer interacting with atom 24. At timestep 135, atom 25 was counted as a sputtered atom. Atom 24 struck atom 25 at a point which distinguishes this event as a **mole** mechanism.

(5) Atom 47. The Ar ion (atom 1) passed downward into the second layer after colliding with atom 39. During its passage downward, it passed within 0.671 LU of atom 48, causing atom 48 to rise upward under atom 47. At timestep 35, atom 48 caused atom 47 to rise upward. Atom 47 was accelerated to a normal velocity of -2880 m/sec by atom 48, and rose from the surface interacting with no other atom. At timestep 95, atom 47 was counted as a sputtered atom. This type of mechanism shows again the interaction of nearest neighbors in the basic tetrahedra, and can best be characterized by the **deep** mechanism.

(6) Atom 119. The Ar ion, after passing through the second layer, passed within 0.391 LU of atom 175, accelerating it in the positive Z direction. The movement of atom 175 caused atom 120 to rise under atom 119. At timestep 60, atom 119 was accelerated upward. At timestep 70, atom 119 was deflected slightly by atom 58, and at timestep 75 it was deflected slightly by atom 56. At timestep 85, atom 119 was 0.935 LU below the surface and was rising freely, interacting with no other atom, with a normal velocity component of -3861 m/sec. At timestep 110, atom 119 passed within 0.797 LU of atom 48, and was slowed to -3747 m/sec. By timestep 120, atom 119 was 0.384 LU below the surface, and was again rising freely with a normal velocity component of -3645 m/sec. At timestep 145, atom 119 was counted as a sputtered atom. The primary sputtering mechanism was the **mole** interaction of atoms 175 and 120.

(7) Atom 63. The interaction of atoms 120 and 64 caused atom 64 to rise below atom 63. At timestep 80, atom 64 pushed atom 63 upward from the surface. Atom 63 interacted with no other atoms, and at timestep 105 was counted as a sputtered atom. The mechanism was the **deep** mechanism caused by atom 120.

(8) Atom 95. After colliding with atom 39, atom 1 continued downward into the second layer. At timestep 25, atom 1 passed within 0.404 LU of atom 103, accelerating atom 103 into collision with atom 98. Atom 103 passed within 0.508 LU of atom 98, accelerating atom 98 downward and in the negative X and Z directions. At timestep 115, atom 98 entered into interaction with atom 95, accelerating atom 95 upward, and in the negative X and Z directions. At timestep 120, atom 98 passed its closest point of approach to atom 95. At timestep 130, atom 95 had risen -0.175 LU, and was no longer interacting with any atom. Atom 95 continued to rise, and at timestep 175 was counted as a sputtered atom. The primary sputtering mechanism was the **mole** mechanism which occurred when atom 98 collided with the lower part of atom 95.

The mechanisms observed in the (111) orientation were all of the type observed by Harrison et al [12]. Harrison et al cited rare examples of the reflection of impacted atoms from lower layers resulting in a sputtering event. The open nature of the (111) orientation makes this type of event more probable in the diamond lattice than in the close-packed fcc crystal investigated by Harrison et al.

2. 1000-eV Results

The 1 keV simulation program required 162 minutes of computer time, 23 minutes longer than the 600-eV simulation. A total of 56 atoms were sputtered with the binding energy set at 1 keV, yielding a sputtering ratio of 1.556. Figure 37 shows the atoms sputtered at this energy. All sputtering events occurred in the first three crystal layers; however, ten atoms were sputtered in the second layer as compared with seven in the 600-eV simulation, and six third-layer atoms were sputtered, twice as many as in the 600-eV simulation. Eleven boundary atoms were sputtered, one more than in the 600 eV simulation. Four atoms were ejected with normal velocity components corresponding to a kinetic energy greater than 15 eV. Three of the high-energy sputs were surface events, while one high-energy sput originated in the third lattice layer. The third-layer sput (atom 179) traveled in the negative X direction while rising to the surface. Since atom 179 was located at the left edge of the crystal, it traveled outside the lattice boundary while rising, and might have been slowed if the lattice were larger.

Figure 38 shows the plot of sputtering ratio vs. ETHR for the 1 keV simulation. The familiar rise below 3 eV binding energy was again evident. The rate of decrease of sputtering ratio above 3 eV was approximately the same as the 600 eV simulation's rate of decrease. The sputtering ratio reached a plateau of 0.250 at 9 and 10 eV, and decreased to 0.111 at 15 eV.

The increased sputtering of deeper atoms as the bombarding energy increased was expected because of the geometry of the (111) orientation. The open appearance of

the "pseudo-channels" is terminated in the third layer, and rising atoms below this depth encounter a much denser crystal. Considerable damage to the second and third layers would be required to create vacancies for deeper sputtering events.

3. Comparison

Figure 39 shows the comparison of the sputtering ratios at 600 eV and 1 keV when plotted vs. ETHR. The sputtering ratio obtained at 1 keV, which was higher at a binding energy of 1 eV, consistently remained above the sputtering ratio obtained at 600 eV until convergence of the sputtering ratios at a binding energy of 15 eV. The sputtering ratios closely approached each other above a binding energy of 8 eV, again suggesting that the correct value of binding energy is probably below this value. The number of boundary atoms sputtered at 600 eV and at 1 keV indicated that the lattice must be expanded in the X and Z directions in order to effect containment, but the depth of four layers seems sufficient to contain all sputtering events at energies up to 1 keV.

D. COMPARISON OF LATTICE ORIENTATIONS

Comparison of the sputtering ratio's obtained at each orientation vs. ETHR for the 600-eV and 1-keV runs yielded additional insight into a possible energy range for the surface binding energy. Examination of figures 3, 5, and 7 shows the (100) orientation to be the densest orientation with highest probability of momentum reversal. The (111) orientation has the next highest probability, and the (110) lattice is the least dense with high probability of deep

penetration. This observation leads to the conclusion that the sputtering ratios should decrease in the order: (100), (111), (110). Figures 40 and 41 show that the sputtering ratios of the (111) and (110) orientations reversed their order of sputtering yields at a value of 4 eV in both the 600-eV and 1-keV simulations. The 600-eV simulation showed another reversal of order at a binding energy of 9 eV. These data points would then indicate that the most probable range of binding energy exists between 4 eV and 9 eV.

E. MOMENTUM TRANSFER IN THE (100) ORIENTATION

Simulation programs were run with bombarding energies of 600 eV and 1 keV for both 8x4x8 fcc copper and 8x4x8 silicon diamond lattices with the impact point displaced 0.3 LU in the X and Z directions from the impact atom's center. Single timestep listings of the atoms were obtained, and the spread of momentum through the crystals was traced by following the spread of lattice atoms which possessed total energies above 0.1 eV. The traces were terminated when a boundary atom was found to possess a total energy greater than 0.1 eV. In addition, simulations were run in which the lower energy spread of momentum (total energy > 0.0) in the top layer of both orientations was traced. Figure 42 shows the numbering scheme of the (100) fcc crystal.

1. 600-eV Results

a. Copper

Figures 43-48 show the spread of momentum through the fcc lattice obtained in the 600 eV simulation.

The momentum was seen to travel along the close-packed (110) chain in the surface layer, and correspondingly along the adjacent (110) chains in the second layer. by timestep 27 (1.345×10^{-14} sec) the upper boundary atom was reached in the surface layer. All atoms moving with an energy greater than 0.1 eV were observed to be boundary atoms of the (110) channel formed by the major diagonal in the crystal.

b. Silicon

Figures 49-57 show the momentum spread in the (100) diamond lattice. The momentum spread here was also observed to travel predominantly along the boundary atoms of the (110) channel formed along the major diagonal. However, as atoms 96, 102, 114, and 120 began to move, they transferred momentum outward from the (110) channel into neighboring channels. The momentum spread was observed to be very orderly, and the mechanism of the spread was observed to be the obvious fact that a moving atom affects the motion of its nearest neighbors. The outward spread of momentum from the first layer to the second was initially slowed in the third layer, since only atoms on the major (110) diagonal commenced moving first. This effect was again found to have an obvious cause, since atoms on the major diagonal were being affected by the motion of two nearest neighbors simultaneously. An extension of the figure at timestep 72 into the fourth layer showed that motion on the three diagonals of the third layer had caused motion on the two diagonals in the fourth layer, resembling very closely the motion of the second-layer atoms. It is assumed that if a fifth layer had been added, the first atoms to move in that layer would have been on the major diagonal, resembling the motion of the first layer. The boundary was reached in the second layer at timestep 72 (3.549×10^{-14} sec).

The transfer of momentum along the (110) chain in the surface layer was broken by the sputtering of atom 57.

2. 1000-eV Results

a. Copper

Figures 58-63 show the momentum spread in the fcc (100) crystal at a bombarding energy of 1 keV. Again, momentum information was observed to travel in the surface layer (110) chain; however, the second and third-layer transfer patterns showed an irregularity not found in the 600 eV simulation. This irregularity was found to result from the passage of the Ar ion between atoms 53 and 57, forcing these atoms in opposite directions. This collision started a momentum transfer along a (110) chain just as the initial impact started a transfer along the surface (110) chain. The boundary was reached at timestep 29 (1.196 x 10⁻¹⁴ sec).

b. Silicon

Figures 64-73 illustrate the momentum transfer in the diamond lattice at 1 keV bombarding energy. The mechanism progressed in a manner similar to the 600 eV simulation with the exception of two off-diagonal atoms moving in the surface layer. It was found that atom 42 was being moved by the slight upward movement of atom 113, and atom 56 was being moved by the slight upward movement of atom 119. This then indicated that the momentum is eventually spread in all directions by nearest-neighbor interactions in the basic tetrahedra. Once again the momentum transfer in the surface (110) chain was broken by

the sputtering of atom 57. The boundary was reached at timestep 87 (3.337×10^{-14} sec).

A comparison of the momentum transfer in the (100) fcc crystal and the (100) diamond lattice showed that the spread of momentum in the diamond lattice was typically deeper, and that the information was spread in orthogonal directions because of the orientation of the silicon bonds in the basic tetrahedra. The collision chains in the diamond lattice seemed to be more easily terminated than in the fcc lattice, but the information spread was still orderly, and could not be represented by a random cascade of collisions such as would be seen in an amorphous solid.

The information spread to the lattice boundaries was 2-3 times slower in the diamond lattice than in the corresponding size fcc lattice, indicating perhaps that smaller lattice sizes in the diamond lattice than in the fcc lattice may prove to sufficiently contain a sputtering event.

3. Precursor Motion

In previous simulation work with fcc crystals, it was found that the simulation conditions rapidly transfer momentum to the boundaries, causing very slight displacements of all atoms in the crystal. These very small displacements, however, affect the subsequent motions of all atoms because of the program's sensitivity to very small displacements and velocities. These small motions would be masked by the thermal motions of the atoms in a real lattice, but they are one of the irritating problems which must be addressed in the simulation programs. In order to compare the effects of these displacements in the fcc crystal and the diamond lattice, a listing of all atoms in

the top layer was obtained for both lattices, and the "precursor motion" of all surface atoms were traced until the boundaries of the surface layers were reached.

Figures 74 and 75 show the spread of momentum through the first layer of an 8x4x8 fcc crystal impacted by a 600 eV Ar ion at a point displaced 0.3 LU in the X direction and 0.3 LU in the Z direction from the center of atom 21. As expected, the momentum traveled along the (110) close-packed chain, reaching both boundaries within five timesteps (1.684×10^{-15} sec).

Figures 76 and 77 show the advance of the precursor motion in the (100) diamond lattice with 600 eV bombarding energy. It was observed that one timestep (approximately 4×10^{-16} sec) was sufficient time to transfer momentum to the next-nearest neighbor. The orthogonal placement of next-nearest neighbors in the tetrahedra then allowed energy transfer in all directions, and the outward spreading "ripple" of momentum reached the surface boundaries in five timesteps (1.894×10^{-15} sec). The diamond lattice and the fcc lattice exhibited very different behaviors in these small-scale energy transfers, but the speed of momentum transfer to the boundaries was approximately the same.

IV. DISCUSSION

A. (100) ORIENTATION

The (100) orientation, being the closest-packed of the three lattice orientations required the longest computer run times and possessed the highest sputtering ratios. At a bombarding energy of 600 eV, the sputtering events were confined to the first three layers (Fig. 16); however, nine atoms located on the X or Z boundaries were sputtered in the first layer. This indicates that at energies as low as 600 eV an 8x4x8 crystal size is inadequate. The 1 keV simulation sputtered 13 atoms located on the X or Z boundaries (Fig. 19), 11 in the first layer, two in the second layer, and one in the third layer. In addition, a low-energy sputtering event originated in the fourth layer. This indicates that the lattice size must be extended in the Y direction if higher energy bombardments are to be performed.

The sputtering mechanisms observed in the (100) orientation (Fig. 18) were essentially the same as those observed in the fcc copper crystal. The one significant exception was the sputtering of atom 32 which was caused by the movement of a third-layer atom in a direction essentially parallel to the X,Z plane. The tetrahedral arrangement of the silicon atoms allowed momentum transfer not only to the nearest neighbor (atom 32), but also to the next-nearest neighbors (atoms 31 and 41). This type of interaction demonstrates the fact that momentum information

can be efficiently transferred from the surface into deeper crystal layers, and conversely from deeper crystal layers to the surface, allowing these deep layers to have a major effect on surface layer interactions. This type of interaction is another indication that the crystal depth is inadequate.

Examination of the sputtering ratios obtained at 600 eV and 1 keV (Figs. 17 and 20) showed a rapid increase in low-energy sputtering events below a surface binding energy of 3 eV. The fourth-layer sputtering event observed at 1 keV bombarding energy was below the 3 eV threshold, and therefore is not considered a significant sputtering event.

B. (110) ORIENTATION

The (110) orientation exhibited the same containment problems as the (100) orientation. At 600 eV, sputtering events were confined to the first two layers (Fig. 23), but four atoms on the X or Z boundaries were sputtered. At 1 keV, five atoms were sputtered on the X or Z boundaries (Fig. 26), but all sputtering events still occurred in the first two layers. With the bombarding energy set at 2 keV, only two X and Z boundary atoms were sputtered (Fig. 29), but a fourth-layer sputtering event occurred with an ejection energy of 2.88 eV. This indicates that the number of layers used in the (110) simulations must be increased at bombarding energies above 1 keV. In addition, the lattice dimensions must be increased in the X and Z directions, especially at lower energies.

The fact that the momentum in the (110) orientation is directed deeper at higher energies was observed in the mechanism traces. The mechanisms were again the same as

those observed by Harrison et al [12], with the exception of the skip mechanism. The skip mechanism rapidly transferred energy rather large distances across the lattice surface and indirectly caused additional sputtering events by imparting high velocities to at least two other surface atoms (Figs. 25 and 28). Without the relatively open spaces created by the (110) channels, and without the placement of the atoms in the ($\bar{1}$ 10) chains located in the lower half-layer of the surface, this mechanism would not be possible. The surface demonstrated a rather "brittle" quality, in that at lower energies the "skipping" atoms were reflected, but at 2-keV bombarding energy, the "skipping" atom was deflected deeply into the crystal. This deep deflection eliminated the surface sputtering of the "skipping" atom, and caused high energy interactions in the lower layers (Fig. 31).

The comparison of the sputtering ratios obtained at 600 eV, 1 keV, and 2 keV plotted vs. ETHR (Fig. 32) showed a cross-over of the sputtering ratio curves at binding energies of 3 and 7 eV. A possible explanation for this type of behavior may exist, however. As the energy of the bombarding ion is increased, the target cross sections of the lattice atoms increase to a point, and then become smaller. This type of behavior could explain the increase in sputtering ratio observed when the energy was increased from 600 eV to 1 keV, and could also explain the lower sputtering ratio obtained at 2 keV. In Fig. 32, the region between 3 and 7 eV shows this type of behavior.

C. (111) ORIENTATION

At both 600 eV and 1 keV bombarding energies, the sputtering events in the (111) orientation were confined to the first three layers (Figs. 34 and 37); however, nine X or

Z boundary atoms were sputtered at 600 eV, and 11 were sputtered at 1 keV. The location of the atoms at the bottom of the "pseudochannels" aided in containment at these low energies, but it is expected that at higher energies the increased crystal damage and decreased target cross sections of these blocking atoms may necessitate crystal expansion in the Y direction.

The mechanisms observed in the (111) orientation were all of the type described in Harrison et al [12], but the one instance of reflection of an atom in the mechanism trace (Fig. 36) indicates that the reflection mechanism is more common in the diamond lattice than in a fcc crystal. It is expected that at higher energies this mechanism will become less common because of lower-layer damage.

The plots of sputtering ratio vs. ETHR in the (111) lattice simulations (Figs. 35 and 38) show the rapid rise of low-energy sputtering events below 3 eV also. This type of behavior was common to all three orientations, and seems to be a very good indication that the binding energy is above this value.

D. SURFACE BINDING ENERGY

Figures 40 and 41 show the comparison of the sputtering ratios of the three lattice orientations plotted vs. ETHR. It was observed that above a surface binding energy of 4 eV, the order of sputtering ratios at both bombarding energies was (100), (111), (110). Considering the densities of the three lattice orientations, this was the order expected for the sputtering ratios. In the 600 eV program, the sputtering ratios of the (110) and (111) surfaces were nearly equal above a binding energy of 4 eV, and these two

ratios were not radically different than the sputtering ratio of the (100) orientation. In 1963, Southern, Willis, and Robinson [23] reported their investigation of the bombardment of Ge and Si by 1- to 5- keV Ar ions. Southern et al reported that they did not find any significant differences in the yields of the (100), (110), and (111) Ge lattices except possibly at higher energies where the sputtering ratios seemed to decrease in the order (100), (111), (110), with the (111) and (110) yields being quite similar. Figures 40 and 41 show this type of behavior also. Considering experimental uncertainties and the possible differences in the sputtering yields of Ge and Si, it can be seen that the sputtering ratios might have been equal within experimental accuracy at lower energies, but as the bombarding energy was increased the ordering of the different orientations became more evident. The interesting fact is that by adjusting ETHR to a value greater than 4 eV, the proper ordering of the sputtering yields is obtained. Southern et al also reported the sputtering ratio of the (111) Si crystal orientation at 1-keV bombarding energy was approximately 0.45. Figure 38 shows that this sputtering ratio was obtained in the 1-keV simulation when the surface binding energy was adjusted to a value of 6-7 eV. Additionally, Wehner et al [2] reported the sputtering ratio of polycrystalline silicon (uncorrected for secondary electron emission) to be approximately 0.52 at a bombarding energy of 600 eV. The mean sputtering ratios of the three orientations was computed for the 600 eV Ar bombardment, and was found to be 0.567 at 4 eV binding energy and 0.467 at 5 eV. These rough calculations show that the sputtering ratios obtained in the simulations agree reasonably well with the available experimental data. Anderson [24] reported obtaining a sputtering ratio of roughly 0.2 for the Si (110) surface bombarded by Ar at 200 eV. Although this result can lead to no definite statement about the simulation, it is reassuring that this sputtering ratio is

below the ratios obtained in the (110) surface 600 eV simulation for binding energies between 1 eV and 10 eV. A reasonable assumption then, based on the proper ordering of the (100), (111), and (110) sputtering ratios between 4 eV and 9 eV, and the reasonable ordering of the (110) ratios obtained at 600 eV, 1 keV, and 2 keV between 3 eV and 7 eV, is that the surface binding energy is between 4 eV and 7 eV.

E. MOMENTUM TRANSFER STUDIES

The study of the spread of energies greater than 0.1 eV in the (100) diamond lattice showed that the momentum was initially transferred along the (110) chains, but spread outward from these chains because of the placement of nearest neighbors on the tetrahedron diagonals. The lattice boundaries were first reached in the lower layers in the diamond lattice (Figs. 57 and 73), as compared to the surface layer in fcc copper (Figs. 48 and 63). The momentum spread to the boundaries required 2-3 times more timesteps in Si than it did in Cu. This indicates then that the silicon lattice may contain all sputtering events utilizing a smaller lattice than the fcc case at corresponding bombardment energies. Since the boundaries are reached later, these boundary conditions will have a smaller effect upon the sputtered atoms, and since the boundaries are reached in lower layers, they will have less effect on the predominant surface sputtering events.

The "precursor motion" in the silicon lattice (Figs. 76 and 77) was observed to spread rapidly in all directions, rather than along a (110) chain as it did in copper (Figs. 74 and 75). It was originally expected that momentum would be transmitted deeper into the lattice, but would spread outward to the X and Z boundaries more slowly. The fact

that every atom in the surface layer was displaced by the fifth timestep was surprising but, in retrospect, should have been expected. These small displacements and atom vibrations are masked by thermal effects, since at the end of the fifth timestep the largest kinetic energy possessed by any atom other than the impact atom was on the order of 10^{-3} eV, and atomic displacements were on the order of 10^{-4} LU (2.72×10^{-4} angstroms). This computer artifact then has no physical significance, but it does affect the subsequent motions of all atoms in the lattice. These small displacements cause the atoms to oscillate about their equilibrium positions until a higher-energy interaction causes a larger displacement. The period of these oscillations (10^{-16} sec) is below that which would be expected in thermal vibrations. This motion is merely numerical noise, and must be tolerated, but not ignored when constructing a simulation model. The observed precursor motion does, however, demonstrate that different lattice configurations do transfer momentum information in radically different ways.

V. CONCLUSIONS AND RECOMMENDATIONS

The preliminary development and investigation of the silicon lattice produced physically reasonable results utilizing an acceptable amount of computer time. The simulations performed with ion bombarding energies of 600 eV, 1 keV, and 2 keV resulted in the identification of the **skip** sputtering mechanism, which was not identified by Harrison et al [12] in the fcc copper lattice. The **reflection** mechanism was found to be more common in the diamond (111) orientation than in the closely-packed fcc crystal. Adjustment of the binding energy to a value between 4 and 7 eV resulted in the proper ordering of the sputtering ratios of the (100), (110), and (111) lattice orientations. The sputtering ratio of the (110) lattice was found to decrease as the bombarding energy was increased to 2 keV as a result of the decreased target cross sections of the lattice atom. A lattice size of 256 atoms was found inadequate to contain all sputtering events at a bombarding energy as low as 600 eV, but was deemed large enough to conduct preliminary bombardment simulations. The spread of momentum in the diamond lattice was found to be 2-3 times slower in the diamond lattice than in the fcc lattice. The initial studies performed should be continued and expanded upon. Wehner et al [1] have gathered data on the temperature dependence of the sputtering yields of silicon, and the ejection patterns obtained from the (100), (110), and (111) orientations. The computer program presently has the capability to randomly displace the lattice atoms as a function of lattice temperature, and with slight modifications could be made to gather statistical data on the ejection directions of the sputtered atoms. Since

experimental data are readily available in these areas, the extension of the silicon investigation into these areas is recommended.

A. LATTICE MODEL

The lattice models of the three orientations do not presently include the bulk relaxation of the lattice surface layers. Harrison et al [14] included surface layer relaxation in their improved fcc copper model and found that emission directions were modified slightly by the relaxation process, and the energy distribution of the sputtered atoms was modified slightly. It is recommended that surface relaxation be applied to the silicon lattice also.

The potential approximations utilized in the simulation programs yielded physically reasonable lattice behaviors at the bombardment energies investigated; however, the relative error of the Si-Si⁺ potential increases above ten percent at potential energies above 10 keV. If high energy bombardments are to be simulated, it would be advisable to improve the approximation at small atomic separations. Inclusion of an attractive potential region could prove to be extremely difficult, and perhaps oversophisticated. In order to properly include an attractive potential region, the directional effect of the potential function would also have to be included. If, in fact, this could be accomplished it is expected that the computer run times involved in simulating the bombardment of a suitable lattice size could become prohibitive. It is expected that the inclusion of an attractive potential region would not materially affect the identification of the sputtering mechanisms, but, as pointed out by Harrison et al [14], the inclusion of an attractive potential would eliminate the use

of a binding energy term, which is a convenient adjustable parameter.

The problem of adequate containment of all sputtering events remains unresolved. While the 256 atom lattice was deemed large enough for preliminary studies, it is recommended that the lattice size be increased until further lattice size increases do not affect the sputtering ratio obtained at a given bombarding energy. The value of ETHR can then be adjusted to obtain a sputtering ratio which conforms to available experimental data.

Preliminary diamond lattice investigations showed that reasonable sputtering ratios were obtained, and correct ordering of the sputtering ratios of the (100), (110), and (111) orientations were obtained with the binding energy set between 4 and 7 eV. Further investigations of sputtering with larger lattice sizes should be performed, and the results correlated with available experimental data in order to further localize the binding energy value.

B. DYNAMICS

The sputtering events observed at bombarding energies of 600 eV, 1 keV, and 2 keV were observed to be predominantly surface events, with almost all sputtering events occurring within the first three lattice layers. The **squeeze**, **scoop**, **mole**, and **deep** mechanisms reported by Harrison et al [12] were observed to be essentially the same in the diamond lattice as in the fcc crystal. The (110) diamond lattice orientation exhibited a mechanism by which a surface atom was displaced across a (110) channel opening, and was reflected from surface atoms, sputtering with a high velocity. This mechanism was described as a **skip** mechanism.

The (111) orientation showed the reflection of a surface impact atom from second and third-layer atoms, a mechanism reported only rarely in the fcc lattice. In all orientations, the efficient transfer of momentum to all atoms in the basic silicon tetrahedron was noted. It is recommended that the energy dependence of the skip and reflection mechanisms be investigated in order to verify their decreasing importance at higher bombarding energies.

The sputtering ratios of all three orientations, but especially the (110) orientation, should be studied as a function of bombarding energy. The point at which the decreased target cross sections of the lattice atoms cause decreased sputtering ratios should be determined, and these data correlated with available experimental data. This will aid in the determination of the surface binding energy.

The investigation of the momentum spreading mechanism in the (100) orientation showed that the momentum initially spreads along the (110) chains, much as it does in the fcc lattice, but the tetrahedral arrangement of the lattice atoms spreads the momentum orthogonal to the (110) diagonal, and allows the efficient transfer of momentum to the lower layers. Boundary atoms were reached in lower layers before the boundary atoms in the surface layer were reached. The momentum spread required 2-3 times as many timesteps in the 8x4x8 diamond lattice than it did in an 8x4x8 fcc copper lattice impacted at the same energy. The small amplitude "precursor motions" in the surface layer were found to spread to all directions in the surface layer, rather than along the (110) diagonal as it did in the fcc lattice. The speed at which the "precursor motions" spread to the boundaries was found to be approximately the same in the diamond lattice and the fcc lattice.

Further investigation of the momentum spread in the (110) and (111) may provide additional insight into the dependence of the sputtering ratios upon the atomic arrangement of various lattice types.

Further investigation of the diamond lattice could prove fruitful in the understanding of the problems and mechanisms involved in semiconductor etching, ion implantation, and depth profiling.

APPENDIX A

DIAMOND LATTICE SUBROUTINES

COY
Direction cosine of the bombarding ion's velocity.

DBXMAX, DBZMAX
Upper boundary limits for the target impact area.

DX,DY,DZ
Unscaled displacement distance components of second atom at a given lattice site.

I,J,K
Integer index variables.

ILL
The number of the last atom in the first layer.

IN
Index integer variable in DL111 subroutine atom placement.

IT,JT,KT
Index variables used in the generation of an atom's X,Y,Z coordinates.

ITT
An odd-even integer used to determine atom site location.

IX, IY, IZ

The number of x,y,z, planes in the crystal.

JTS

Variable used in DL111 subroutine to determine the Z coordinate of a given atom.

JTT

Index variable in DL111 subroutine.

L

Number assigned to the second atom at a given lattice site.

LD

Number of the next-to-highest numbered mobile atom.

LL

The highest numbered atom in the entire crystal.

M

Number assigned to the first atom at a given lattice site.

R1

Distance from lattice impact point to the bombarding ion's initial position.

ROE

Lattice nearest-neighbor distance.

RXI (I) ,RYI (I) ,RZI (I)

Initial position of the Ith atom in the lattice (used to reposition the atom before the next impact).

SCX, SCY, SCZ

The x,y,z lattice scale factors used to convert the generated lattice to match a real crystal.

SI

Reciprocal of the square root of 2.0 (used to avoid repeated division).

SPDX, SPDZ

The fraction of the target impact area that the impact points are incremented.

SSPDZ

SPDZ divided by 3.0 (used in DL111 subroutine to avoid repeated division).

SSCZ

SCZ divided by 3.0 (used in DL111 subroutine to avoid repeated division).

ZP

Unscaled Z displacement variable used in DL111 subroutine to center the lower-layer atoms in the equilateral triangles formed by the surface atoms.


```

RY(M)=RY(L)+DY
RZ(M)=RZ(L)+DZ
RXI(M)=RX(M)
RYI(M)=RY(M)
RZI(M)=RZ(M)
M=M+1
39 CONTINUE
IT=IT+1
40 CONTINUE
KT=KT+1
50 CONTINUE
IF(JT.=Q.0) ILL=M-1
JT=JT+1
IF(JT.=Q.IDEEP) LD=M-1
60 CONTINUE
LL=LL-1
IF(LL.=Q.0) LD=LL-1
IF(CDY.EQ.0.0) GO TO 120
R1=RCE/ABS(CDY)
RETURN
120 R1=1.5
RETURN
END

```

SUBROUTINE DL110

DL110 GENERATES A DIAMOND LATTICE IN THE (110) ORIENTATION. A CHAIN OF ATOMS IS FIRST GENERATED IN THE X DIRECTION, AND THEN THE SAME CHAIN IS GENERATED AFTER BEING DISPLACED IN THE Z DIRECTION. WHEN A LAYER IS FILLED, THE SAME CHAINS ARE GENERATED IN THE NEXT LAYER STARTING AT DIFFERENT INITIAL X AND Z POSITIONS

```

COMMON/COM1/RX(600),RY(600),RZ(600),LCUT(600),LL,LD
COMMON/COM2/ROE,ROE2,ROEM,AC,PAC,PPTC,PTC,PFPTC,FPIC,
1FM,PFIV,TPOT
COMMON/COM4/IX,IY,IZ,IXP,IYP,IZP,SCX,SCY,SCZ,IDEEP,
2RFX,RBZ
COMMON/COM7/R1,LSS,SPX,SPZ,CDX,CDY,CDZ,YLAX(20),ILL
COMMON/COM9/IDX,IDY,IDZ,DXT,DYT,DZT,TPDX,TPDY,TPDZ
COMMON/COM11/RXI(600),RYI(600),RZI(600)
COMMON/COM23/SPDX,SPDZ,DBXMAX,DBZMAX
SET IMPACT AREA PARAMETERS

```

```

SI=1.0/SQRT(2.0)
LC=0
SCX=SI
SCY=SI
SCZ=1.0
DBXMAX=1.0
DBZMAX=2.0
SPDX=DBXMAX/5.0
SPDZ=DBZMAX/5.0
DX=SI
DY=J.0
DZ=0.5

```

BEGIN LATTICE GENERATION

```

M=3
JT=0
Y=-SCY
DO 60 J=1,IY

```

```

Y=Y+SCY
KT=0
Z=-SCZ
DC 50 K=1, IZ
Z=Z+SCZ
IT=0
X=-SCX
DC 40 I=1, IX
X=X+SCX
11 IF(IT-(IT/2)*2) 21,11,21
12 IF(JT-(JT/2)*2) 40,12,40
21 IF(KT-(KT/2)*2) 40,30,40
22 IF(JT-(JT/2)*2) 22,40,22
30 IF(KT-(KT/2)*2) 30,40,30
RX(M)=X
RXI(M)=X
RY(M)=Y
RYI(M)=Y
RZ(M)=Z
RZI(M)=Z
L=M
M=M+1
RX(M)=RX(L)+OX
RXI(M)=RX(M)
RY(M)=RY(L)+OY
RYI(M)=RY(M)
RZ(M)=RZ(L)+OZ
RZI(M)=RZ(M)
M=M+1
40 IT=IT+1
KT=KT+1
50 CONTINUE
IF(JT.EQ.0) ILL=M-1
JT=JT+1
IF(JT.EQ.IDEFP) LD=M-1
60 CONTINUE
LL=M-1
IF(LD.EQ.0) LD=LL-1
IF(COY.EQ.0.0) GO TO 120
R1=ROE/ABS(COY)
RETURN
120 R1=1.5
RETURN
END

```

SUBROUTINE DL111

CCCCCCCC

DL111 GENERATES A DIAMOND LATTICE IN THE (111) ORIENTATION. THE ATOMS ARE PLACED IN PAIRS AT EACH LATTICE SITE, WITH GENERATION FIRST IN THE X AND THEN IN THE Z DIRECTION. WHEN THE FIRST LAYER IS COMPLETE THE SECOND LAYER ATOMS ARE PLACED DIRECTLY BENEATH THE CENTROIDS OF THE EQUILATERAL TRIANGLES FORMED BY THE FIRST LAYER ATOMS. THE THIRD LAYER ATOMS ARE PLACED BENEATH THE SECOND LAYER CENTROIDS. THE FOURTH LAYER IS A REPEAT OF THE FIRST LAYER.

```

COMMON/COM1/RX(600),RY(600),RZ(600),LCUT(600),LL,LD
COMMON/COM2/ROE,ROE2,ROEM,AC,PAC,PPTC,PTC,PEPTC,FPTC,
1FM,PFIV,TPOT
COMMON/COM4/IX,IY,IZ,IXP,IYP,IZP,SCX,SCY,SCZ,IDEFP,
2RBX, RBZ
COMMON/COM7/R1,LSS,SPX,SPZ,COX,COY,COZ,YLAX(20),ILL
COMMON/COM9/IDX,IDY,IDZ,DXT,DYT,DZT,TPDX,TPDY,TPOZ

```

```
CCMMON/COM11/RXI(600),RYI(600),RZI(600)
CCMMON/COM23/ SPDZ,SPDX,DBXMAX,DBZMAX
CCMMON/COM26/SSPDZ
```

CC

SET IMPACT AREA PARAMETERS

```
LD=0
SCX=1.0/SQRT(2.0)
SCY=2.0/SQRT(3.0)
SCZ=SQRT(1.5)
SSCZ=SCZ/3.0
DBZMAX=2.0
DBXMAX=1.0
SPDX=DBXMAX/5.0
SPDZ=DBZMAX/10.0
SSPDZ=SPDZ/3.0
DX=0.0
DY=ROE
CZ=0.0
```

CC

BEGIN LATTICE GENERATION

```
JT=0
M=3
Y=-SCY
DC 60 J=1,IY
Y=Y+SCY
KT=0
JTS=JT+JT/3
Z=-SCZ
DC 50 K=1,IZ
Z=Z+SCZ
IT=0
X=-SCX
DC 40 I=1,IX
X=X+SCX
IN=IT+JTS+KT
IF(IN-(IN/2)*2) 39,30,39
30 RX(M)=X
RXI(M)=RX(M)
RY(M)=Y
RYI(M)=RY(M)
IF(JT-3*(JT/3)) 31,35,31
31 JTT=JT
32 JTT=JTT-3
IF(JTT) 33,35,32
33 JTT=JTT+3
ZP=JTT
RZ(M)=Z+ZP*SSCZ
RZI(M)=RZ(M)
GO TO 37
35 RZ(M)=Z
RZI(M)=RZ(M)
37 M=M+1
RX(M)=RX(L)+DX
RXI(M)=RX(M)
RY(M)=RY(L)+DY
RYI(M)=RY(M)
RZ(M)=RZ(L)+DZ
RZI(M)=RZ(M)
M=M+1
39 CONTINUE
IT=IT+1
4) CONTINUE
KT=KT+1
50 CONTINUE
IF(JTT.EQ.0) ILL=M-1
JT=JT+1
IF(JT.EQ.IDEFP) LD=M-1
60 CONTINUE
LL=M-1
```

```
IF(LD.EC.0) LD=LL-1
IF(COY.EQ.0.0) GO TO 120
R1=ROE/ABS(COY)
RETURN
120 R1=1.5
RETURN
END
```

APPENDIX B

ENERGY SUBROUTINE

A

Exponential Bohr potential parameter in Si-Si interaction.

B

Exponential Bohr potential parameter in Si-Si interaction.

DIST

Variable used alternately as the square of the distance between two atoms, and as the distance between two atoms.

DRX,DRY,DRZ

X,Y,Z components of the displacement vector between two atoms.

EXA,EXB

Exponential Born-Mayer potential parameters in Si-Si interaction.

I

Index.

IP

Index.

J

Index.

LCUT (I)

Integer which indicates whether the Ith atom has exited the sides or bottom of the crystal, has risen from the crystal surface, or is still within the crystal.

LD

Number of the next-to-highest numbered mobile atom.

LL

Highest numbered atom in the lattice.

PA,PB

Bohr exponential coefficients in Ar-Si interaction.

PAD,PBD

Transition potential exponential coefficients in Ar-Si interaction.

PEXA,PEXB

Born-Mayer exponential coefficients in Ar-Si interaction.

PPIV

0.5

POT

Potential energy generated between atoms by their interaction.

PPE(I)

Potential energy of the Ith atom.

PPTC

Ar-Si interaction potential evaluated at nearest-neighbor separation.

PTC

Si-Si interaction potential evaluated at nearest-neighbor separation.

PVBM

Born-Mayer term of the Ar-Si interaction potential.

ROE

Nearest-neighbor distance.

ROE2

Nearest-neighbor distance squared.

ROEA

Cross-over point of the Bohr and Born-Mayer portions of the Si-Si interaction approximation.

ROEB

Cross-over point of the Bohr and Born-Mayer portions of the Ar-Si interaction potential approximation.

ROEC

Truncation distance of the Ar-Si interaction potential (set at nearest-neighbor distance).

ROEC2

Ar-Si truncation distance squared.

SAVE

One-half of the potential energy generated by the interaction of two atoms.

RX(I),RY(I),RZ(I)

X,Y,Z coordinates of the Ith atom.

TPOT

Total potential energy of all atoms.

XMAX,YMAX,ZMAX

Maximum X,Y,Z coordinates of any atom which could interact with the atom being evaluated.

XMIN,YMIN,ZMIN

Minimum X,Y,Z coordinates of any atom which could interact with the atom being evaluated.

SLBROUTINE ENERGY

THIS SUBROUTINE CALCULATES THE MUTUAL POTENTIAL ENERGIES OF INTERACTING ATOMS. THIS SUBROUTINE IS AN ADAPTION OF THE MUNDKUR HIGH-SPEED VERSION WITH TWO-BRANCH APPROXIMATIONS OF THE POTENTIALS.

COMMON/COM1/RX(600),RY(600),RZ(600),LCUT(600),LL,LD
COMMON/COM2/ROE,ROE2,ROEM,AC,PAC,PPTC,PTC,PEPTC,FPTC,
1 FM,PFIV,TPOT
COMMON/COM3/FXA,FXB,FXA,PEXA,PEXB,PEXA,THERM
COMMON/COM5/FX(600),FY(600),FZ(600),PPE(600)
COMMON/COM22/ROEA,ROEB,ROEC,ROEC2,CPO,CP1,CP2,CP3,CF0,
2 CF1,CF2,CG01,CG02,CGB1,CGB2
COMMON/COM24/PA,PB,PAD,PBD,A,B,PFAD,CVED

SCATTERING ION-LATTICE ATOM INTERACTION COMPUTATION

I=1
IF(LCUT(I).NE.0) GO TO 200
XMIN=RX(I)-ROEC
XMAX=RX(I)+ROEC
YMIN=RY(I)-ROEC
YMAX=RY(I)+ROEC
ZMIN=RZ(I)-ROEC
ZMAX=RZ(I)+ROEC
DO 195 J=2,LL
IF(LCUT(J).NE.0) GO TO 195
IF(RY(J).GE.YMAX) GO TO 195
IF(RY(J).LE.YMIN) GO TO 195
IF(RX(J).GE.XMAX) GO TO 195
IF(RX(J).LE.XMIN) GO TO 195
IF(RZ(J).GE.ZMAX) GO TO 195
IF(RZ(J).LE.ZMIN) GO TO 195
DRX=RX(J)-RX(I)
DRY=RY(J)-RY(I)
DRZ=RZ(J)-RZ(I)
DIST=DRX**2+DRY**2+DRZ**2
IF(DIST.GE.ROEC2) GO TO 195
DIST=SQRT(DIST)
PVBM=EXP(PEXA+PEXB#DIST)-PPTC
IF(DIST.GT.ROEB) GO TO 175
POT=EXP(PA+PB#DIST)/DIST+PVBM
GO TO 180
175 PCT=EXP(PAD+PBD#DIST)+PVBM
180 TPOT=TPOT+POT
SAVE=PFIV#POT
PPE(I)=PPE(I)+SAVE
PPE(J)=PPE(J)+SAVE
195 CONTINUE
200 CONTINUE

LATTICE ATOM INTERACTION COMPUTATION.

DO 300 I=2,LD
IF(LCUT(I).NE.0) GO TO 300
IP=I+1
XMAX=RX(I)+ROE
XMIN=RX(I)-ROE
YMAX=RY(I)+ROE
YMIN=RY(I)-ROE
ZMAX=RZ(I)+ROE
ZMIN=RZ(I)-ROE
DO 295 J=IP,LL
IF(LCUT(J).NE.0) GO TO 295
IF(RY(J).GE.YMAX) GO TO 295
IF(RY(J).LE.YMIN) GO TO 295
IF(RX(J).GE.XMAX) GO TO 295
IF(RX(J).LE.XMIN) GO TO 295
IF(RZ(J).GE.ZMAX) GO TO 295

```

IF(RZ(J).LE.ZMIN) GO TO 295
DRX=RX(J)-RX(I)
DRY=RY(J)-RY(I)
DRZ=RZ(J)-RZ(I)
DIST=DRX**2+DRY**2+DRZ**2
IF(DIST.GE.RDE2) GO TO 295
DIST=SQRT(DIST)
POT=EXP(EXA+EXB*DIST)-PTC
IF(DIST.GT.RDEA) GO TO 280
PCT=EXP(A+B*DIST)/DIST+POT
280 TPCT=TPCT+PCT
SAVE=PFIV*PCT
PPE(I)=PPE(I)+SAVE
PPE(J)=PPE(J)+SAVE
295 CONTINUE
300 CONTINUE
DO 310 I=1,LL
IF(LCUT(I).EQ.0) GO TO 310
TPOT=TPOT+PPE(I)
310 CONTINUE
RETURN
END

```

APPENDIX C

STEP SUBROUTINE

A
Exponential Bohr potential parameter in Si-Si interaction.

AC
Si-Si exponential force coefficient obtained by differentiation of the Born-Mayer potential term.

B
Exponential Bohr potential parameter in Si-Si interaction.

CVED
Ratio used to convert forces to MKS units.

DFF
Difference between the separation distance of two atoms and force truncation distance (ROEC-DIST).

DIST
Variable used alternately as the square of the distance between two atoms, and as the distance between two atoms.

DRX, DRY, DRZ
X, Y, Z components of the displacement vector between two atoms.

EYA, EXB

Exponential Born-Mayer potential parameters in Si-Si interaction.

FA

Directional force component (force multiplied by direction cosine).

FBM

Force term obtained by differentiation of the Born-Mayer term in the Ar-Si interaction.

FM

Minimum force given to an atom, atoms having forces exerted on them which are less than FM have their forces set to zero.

FOD

Force divided by distance.

FORCE

Magnitude of the repulsive force between two atoms.

FPTC

Si-Si force evaluated at nearest-neighbor distance.

FX(I), FY(I), FZ(I)

X, Y, Z force components exerted on the Ith atom.

FXA

Si-Si exponential force coefficient obtained by differentiation of the Bohr potential term.

I Index.

IP Index.

J Index.

LCUT (I) Integer which indicates whether the Ith atom has exited the sides or bottom of the crystal, has risen from the crystal surface, or is still within the crystal.

LD Number of the next-to-highest numbered mobile atom.

LL Highest numbered atom in the lattice.

PA,PB Bohr exponential coefficients in Ar-Si interaction.

PAC Ar-Si exponential force coefficient obtained from differentiation of Born-Mayer interaction potential.

PAD,PBD Transition potential exponential coefficients in Ar-Si interaction.

PEXA,PEXB

Born-Mayer exponential coefficients in Ar-Si interaction.

PFAD

Ar-Si Born-Mayer force exponential coefficient obtained from differentiation of the Born-Mayer transition potential.

PFIV

0.5

PFPTC

Ar-Si force evaluated at truncation point (ROEC).

PFXA

Ar-Si force exponential coefficient obtained by differentiation of the Bohr potential term.

PPE(I)

Potential energy of the Ith atom.

POT

Potential energy generated between atoms by their interaction.

PPTC

Ar-Si interaction potential evaluated at nearest-neighbor separation.

PTC

Si-Si interaction potential evaluated at nearest-neighbor separation.

PVBM Born-Mayer term of the Ar-Si interaction potential.

ROE Nearest-neighbor distance.

ROE2 Nearest-neighbor distance squared.

ROEA Cross-over point of the Bohr and Born-Mayer portions of the Si-Si interaction approximation.

ROEB Cross-over point of the Bohr and Born-Mayer portions of the Ar-Si interaction potential approximation.

ROEC Truncation distance of the Ar-Si interaction potential (set at nearest-neighbor distance).

ROEC2 Ar-Si truncation distance squared.

ROEM Atomic separation distance at which average, rather than instantaneous force between atoms is calculated.

SAVE One-half of the potential energy generated by the interaction of two atoms.

RX(I) ,RY(I) ,RZ(I)

X,Y,Z coordinates of the Ith atom.

TPOT

Total potential energy of all atoms.

XMAX,YMAX,ZMAX

Maximum X,Y,Z coordinates of any atom which could interact with the atom being evaluated.

XMIN,YMIN,ZMIN

Minimum X,Y,Z coordinates of any atom which could interact with the atom being evaluated.

SLBROUTINE STEP

THIS SUBROUTINE CALCULATES THE FORCE BETWEEN ATOMS
THIS IS THE DIAMOND LATTICE ADAPTION OF THE MUNDKUR
HIGH-SPEED VERSION WITH THREE-BRANCH APPROXIMATIONS
OF THE FORCE FUNCTIONS.

COMMON/COM1/RX(600),RY(600),RZ(600),LCUT(600),LL,LD
COMMON/COM2/ROE,ROE2,ROEM,AC,PAC,PPTC,PTC,PEPTC,FPTC,
IFM,PFIV,TPOT
COMMON/COM3/FXA,EXB,FXA,PEXA,PEXB,PEXA,THERM
COMMON/COM5/FX(600),FY(600),FZ(600),PPF(600)
COMMON/COM22/ROFA,ROFB,ROEC,ROFC2,CP0,CP1,CP2,CP3,CF0,
ZCF1,CF2,CGD1,CGD2,CGB1,CGB2
COMMON/COM24/PA,PB,PAD,PBD,A,B,PFAD,CVED

BOBARDING ION-LATTICE ATOM INTERACTION COMPUTATION

I=1
IF(LCUT(I).NE.0) GO TO 200
XMAX=RX(I)+ROEC
XMIN=RX(I)-ROEC
YMAX=RY(I)+ROEC
YMIN=RY(I)-ROEC
ZMAX=RZ(I)+ROEC
ZMIN=RZ(I)-ROEC
DO 195 J=2,LL
IF(LCUT(J).NE.0) GO TO 195
IF(RY(J).GE.YMAX) GO TO 195
IF(RY(J).LE.YMIN) GO TO 195
IF(RX(J).GE.XMAX) GO TO 195
IF(RX(J).LE.XMIN) GO TO 195
IF(RZ(J).GE.ZMAX) GO TO 195
IF(RZ(J).LE.ZMIN) GO TO 195
DRX=RX(J)-RX(I)
DRY=RY(J)-RY(I)
DRZ=RZ(J)-RZ(I)
DIST2=DPX**2+DRY**2+DRZ**2
IF(DIST2.GE.ROEC2) GO TO 195
DIST=SQRT(DIST2)
IF(DIST.GT.ROEM) GO TO 165
FBM=EXP(PEXA+PEXB*DIST)
IF(DIST.GT.ROEB) GO TO 175
FORCE=CVED*(1-PB*DIST)*EXP(PA+PB*DIST)/DIST2+FBM
GO TO 180
175 FORCE=EXP(PFAD+PBD*DIST)+FBM
GO TO 180
165 DFF=ROEC-DIST
IF(DFF.LT.1.0E-10) GO TO 195
FORCE=(EXP(PAC+PEXB*DIST)-PEPTC)/DFF
IF(FM.GT.FORCE) GO TO 195
130 FCD=FORCE/DIST
FA=FCD*DRX
FX(I)=FX(I)-FA
FX(J)=FX(J)+FA
FA=FCD*DRY
FY(I)=FY(I)-FA
FY(J)=FY(J)+FA
FA=FCD*DRZ
FZ(I)=FZ(I)-FA
FZ(J)=FZ(J)+FA
195 CONTINUE
200 CONTINUE

LATTICE ATOM INTERACTION COMPUTATION.

DO 300 I=2,LD
IF(LCUT(I).NE.0) GO TO 300
IP=I+1
XMAX=RX(I)+ROE

AD-A041 152

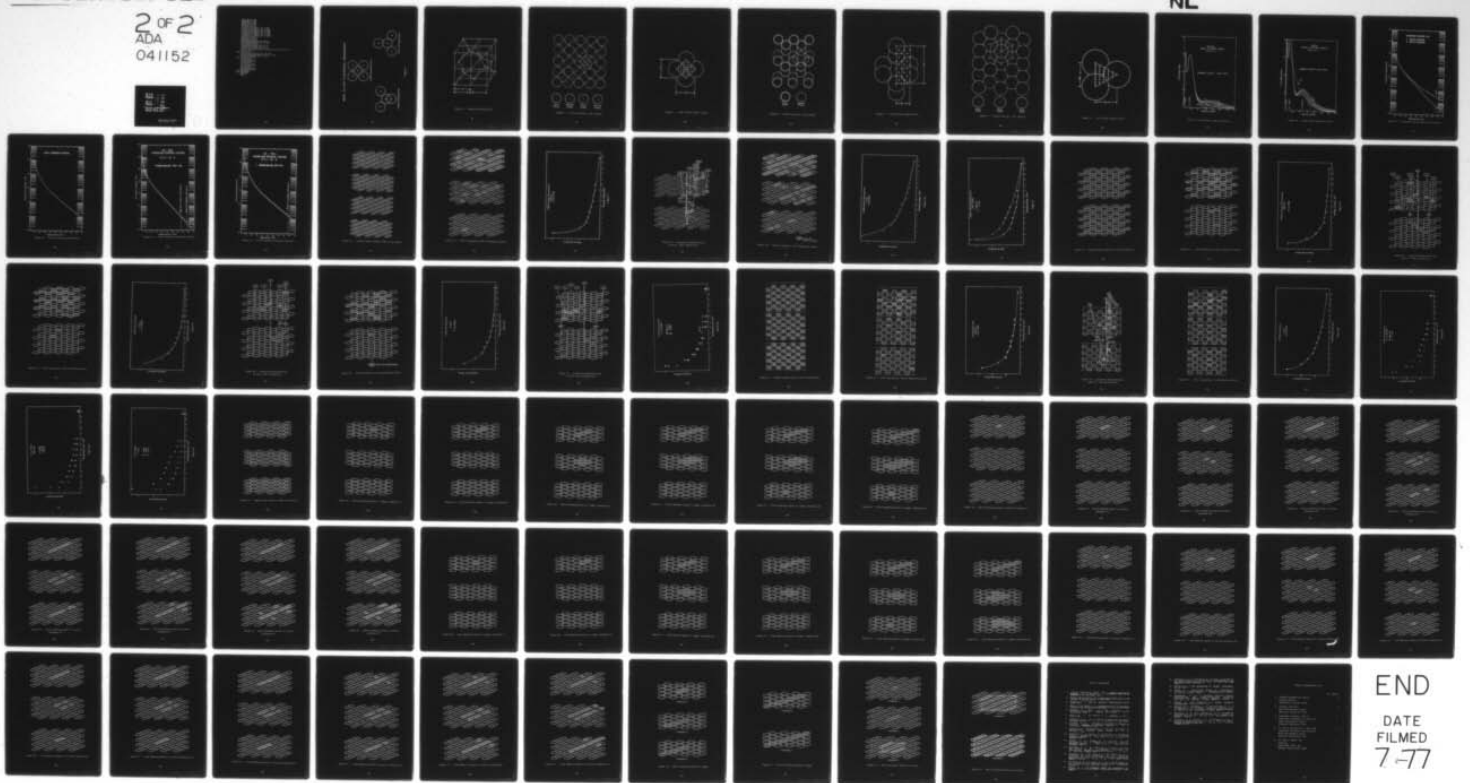
NAVAL POSTGRADUATE SCHOOL MONTEREY CALIF
COMPUTER SIMULATION OF THE SPUTTERING OF SILICON.(U)
JUN 77 G L SMITH

F/G 13/8

UNCLASSIFIED

2 OF 2
ADA
041152

NL



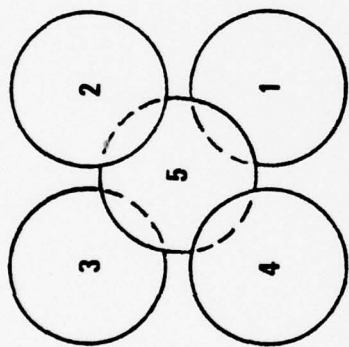
END
DATE
FILMED
7-77

```

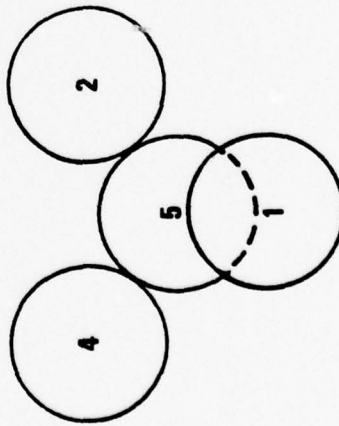
XMIN=RX(I)-ROE
YMAX=RY(I)+ROE
YMIN=RY(I)-ROE
ZMAX=RZ(I)+ROE
ZMIN=RZ(I)-ROE
DO 295 J=IP,LL
IF(LCUT(J).NE.0) GO TO 295
IF(RY(J).GE.YMAX) GO TO 295
IF(RY(J).LE.YMIN) GO TO 295
IF(RX(J).GE.XMAX) GO TO 295
IF(RX(J).LE.XMIN) GO TO 295
IF(RZ(J).GE.ZMAX) GO TO 295
IF(RZ(J).LE.ZMIN) GO TO 295
DRX=RX(J)-RX(I)
DRY=RY(J)-RY(I)
DRZ=RZ(J)-RZ(I)
DIST2=DRX**2+DRY**2+DRZ**2
IF(DIST2.GE.ROE2) GO TO 295
DIST=SQRT(DIST2)
IF(DIST.GT.ROEM) GO TO 265
FORCE=EXP(FXA+FXB*DIST)
IF(DIST.GT.ROEA) GO TO 275
FORCE=CVED*(1-B*DIST)*EXP(A+B*DIST)/DIST2+FORCE
GO TO 275
265 DFF=ROE-DIST
IF(DFF.LT.1-JE-1J) GO TO 295
FORCE=(EXP(AC+FXB*DIST)-FPTC)/DFF
IF(FM.GT.FORCE) GO TO 295
275 FOD=FORCE/DIST
FA=FOD*DRX
FX(J)=FX(J)+FA
FX(I)=FX(I)-FA
FA=FOD*DRY
FY(J)=FY(J)+FA
FY(I)=FY(I)-FA
FA=FOD*DRZ
FZ(J)=FZ(J)+FA
FZ(I)=FZ(I)-FA
295 CONTINUE
300 CCNTINUE
RETURN
END

```

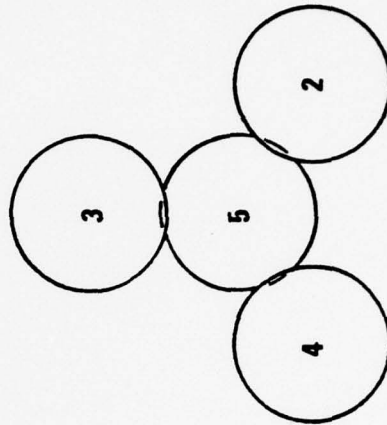
BASIC SILICON TETRAHEDRAL ARRANGEMENT



(100) Orientation



(110) Orientation



(111) Orientation

Figure 1

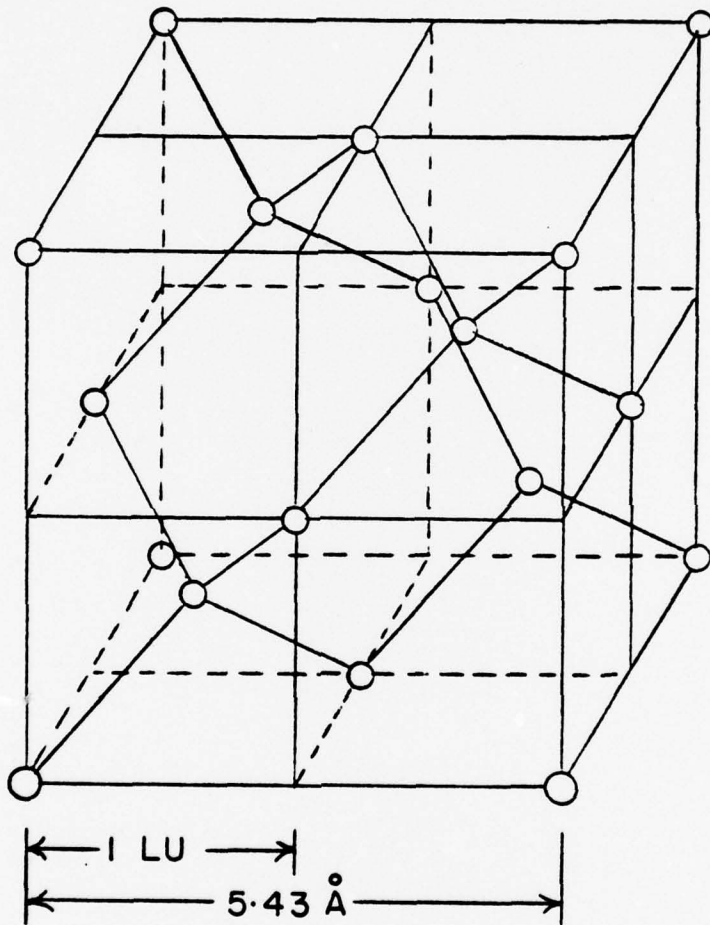


Figure 2 - Diamond Microcrystalite

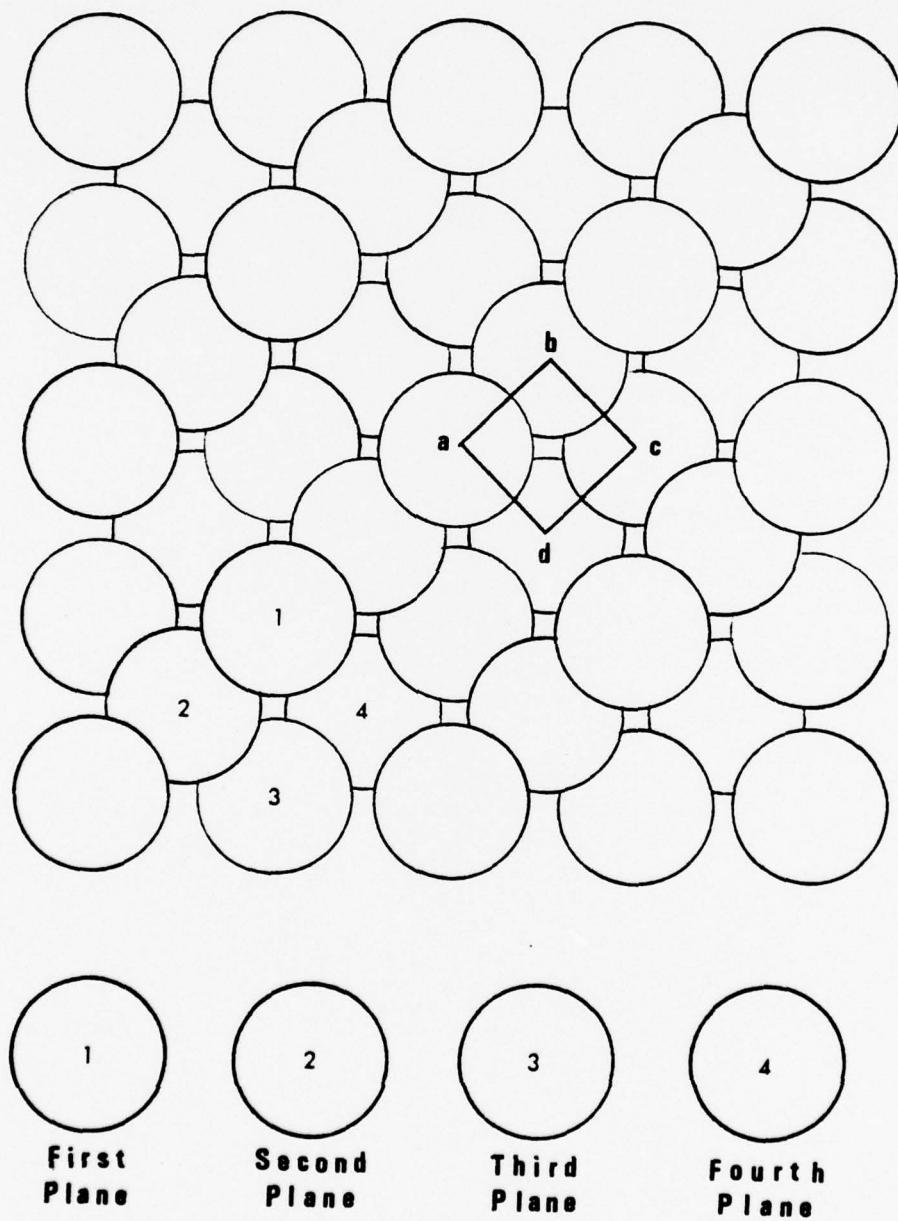


Figure 3 - Silicon Lattice, (100) Surface

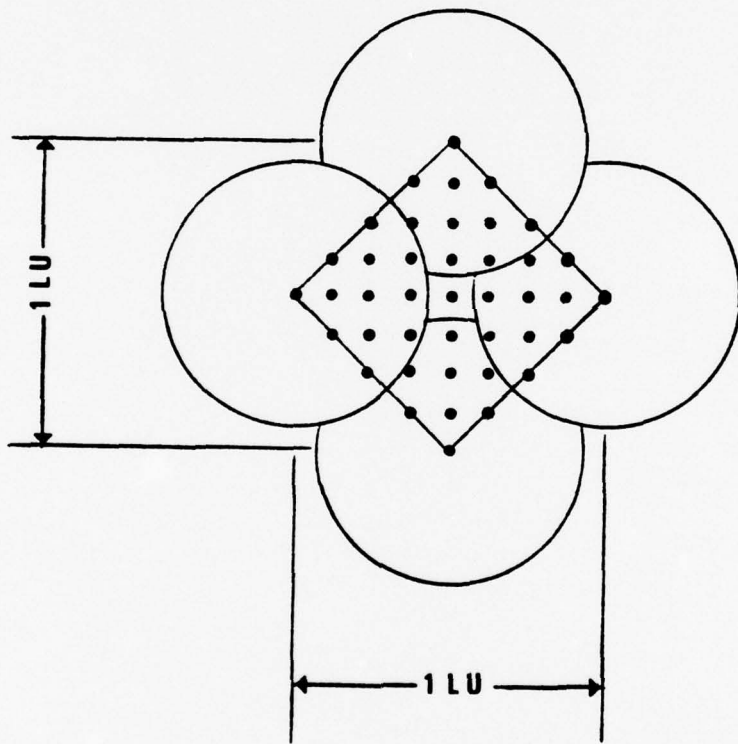


Figure 4 - (100) Surface Impact Points

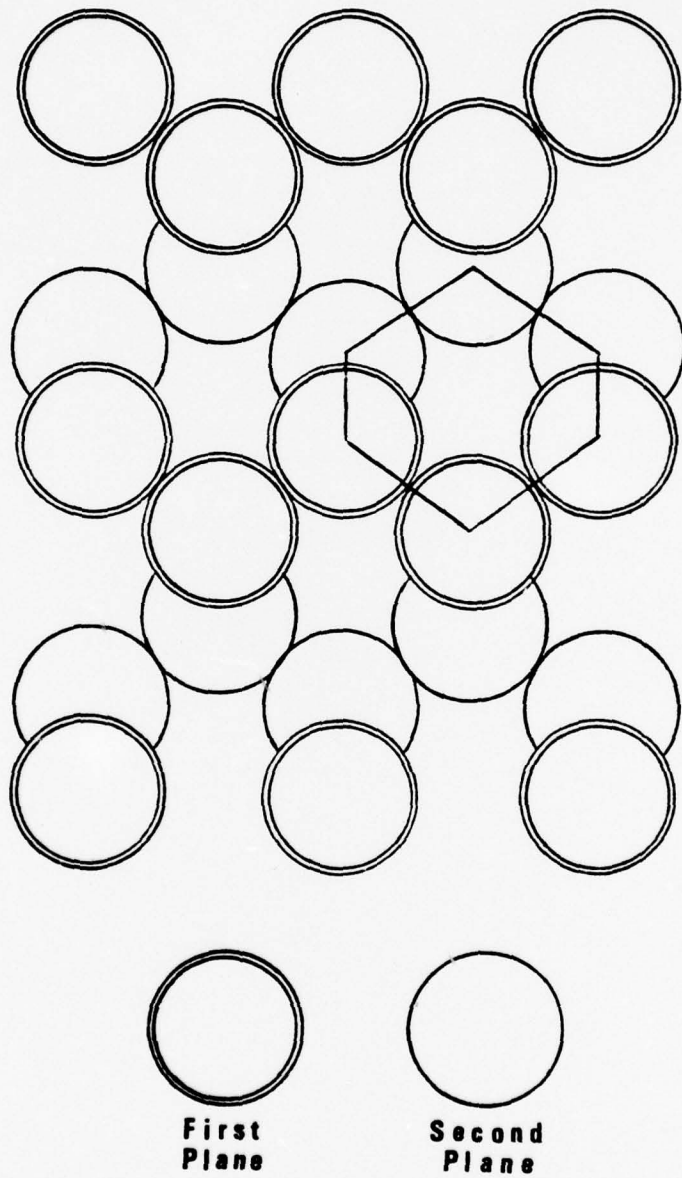


Figure 5 - Silicon Lattice, (110) Surface

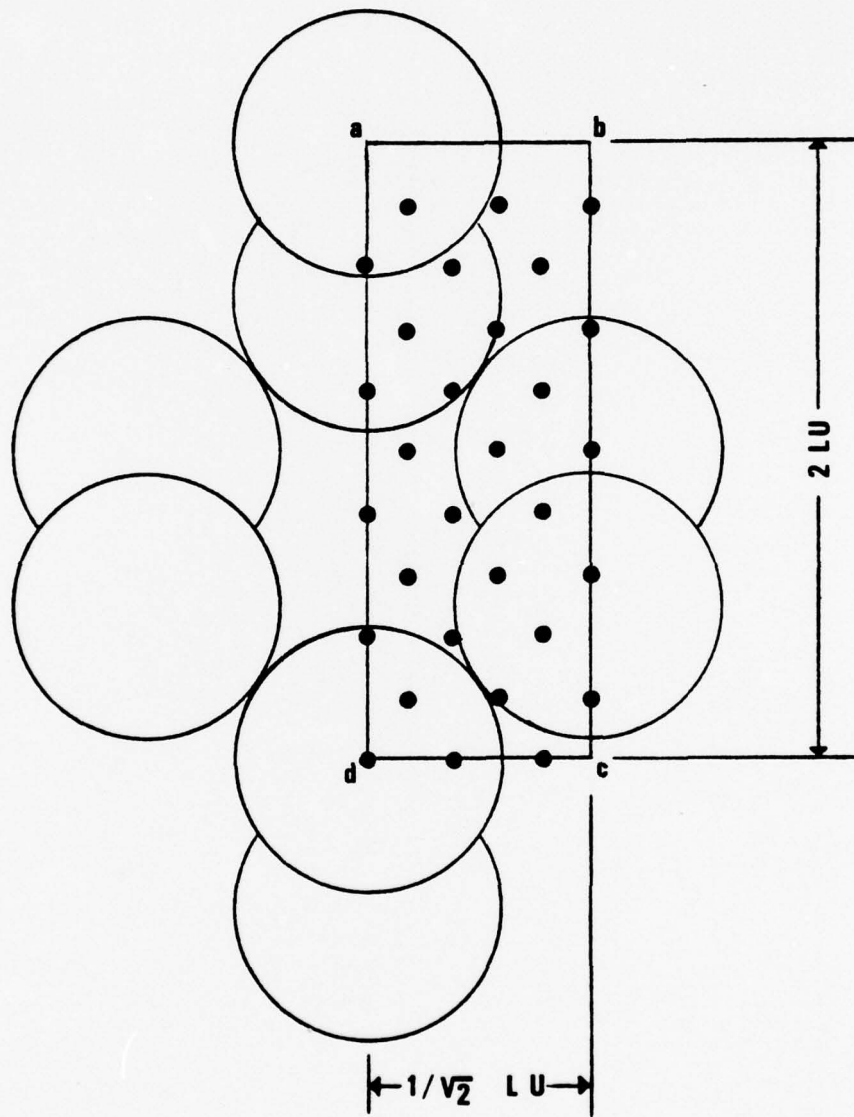


Figure 6 - (110) Surface Impact Points

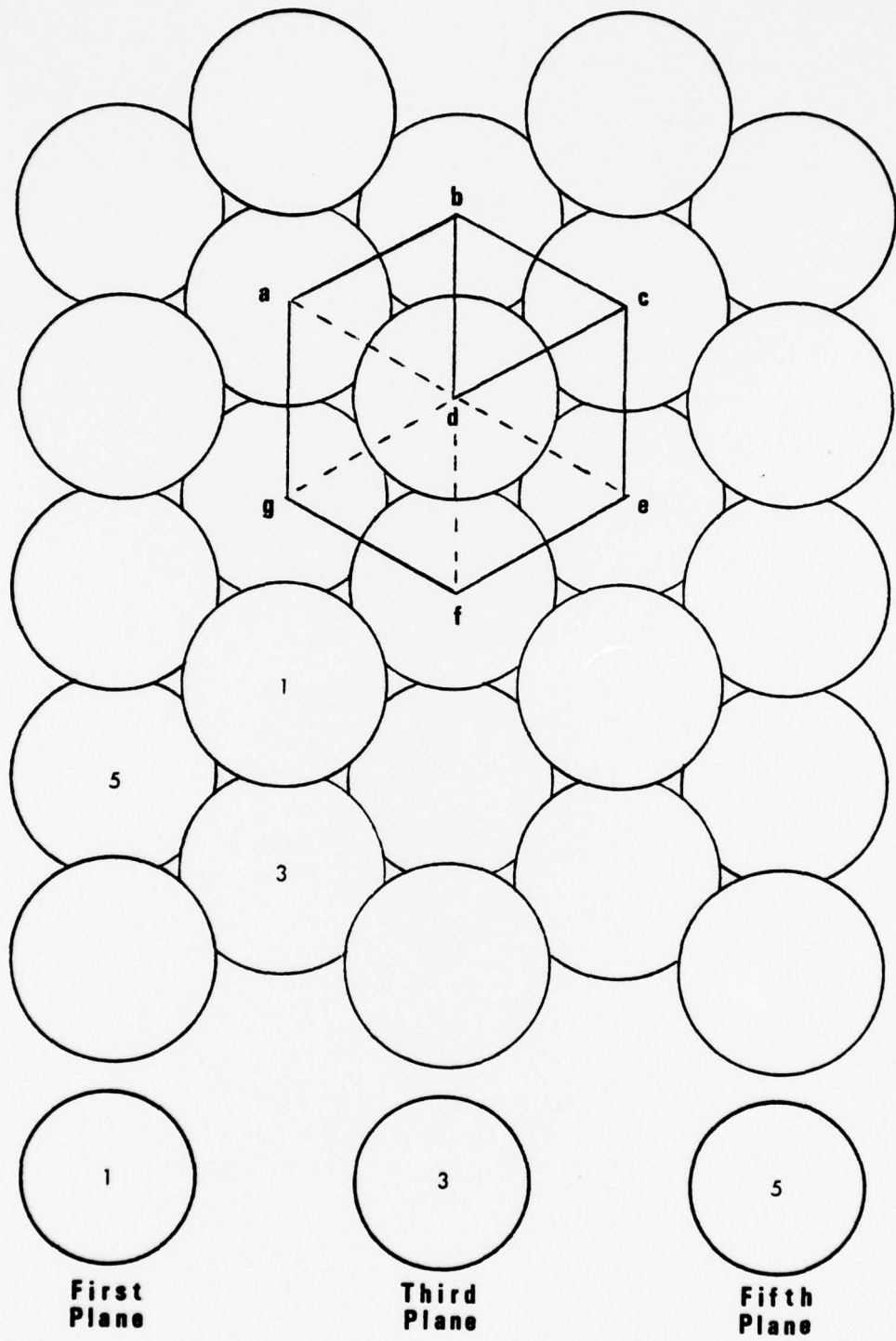


Figure 7 - Silicon Lattice, (111) Surface

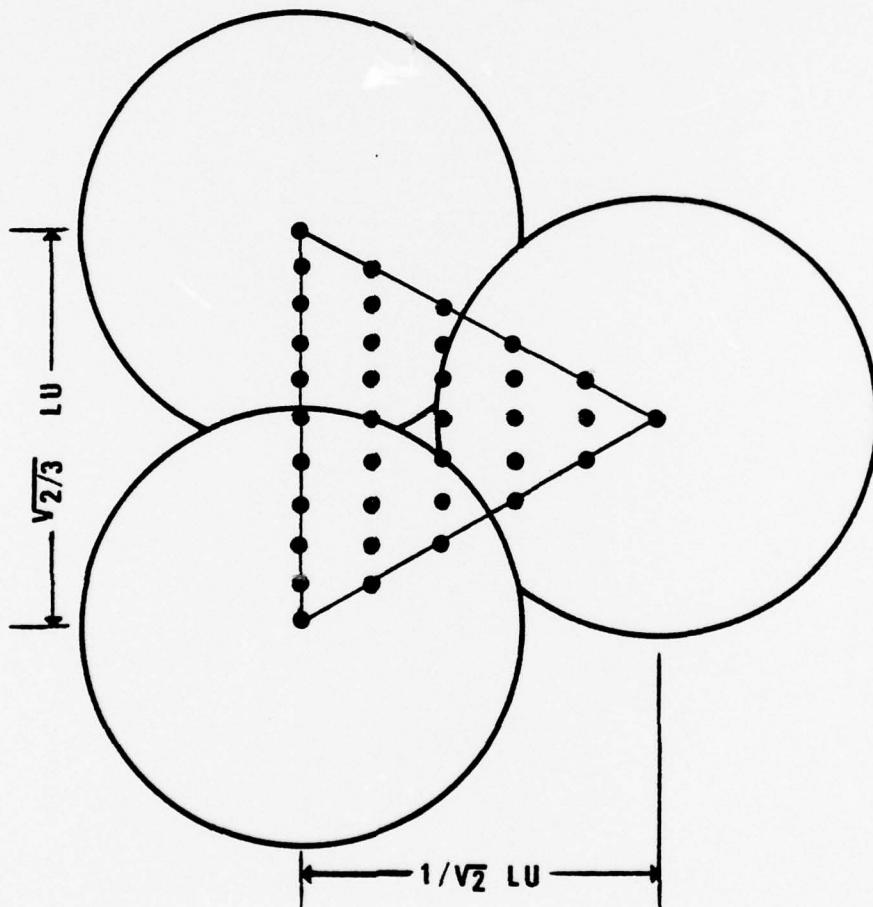


Figure 8 - (111) Surface Impact Points

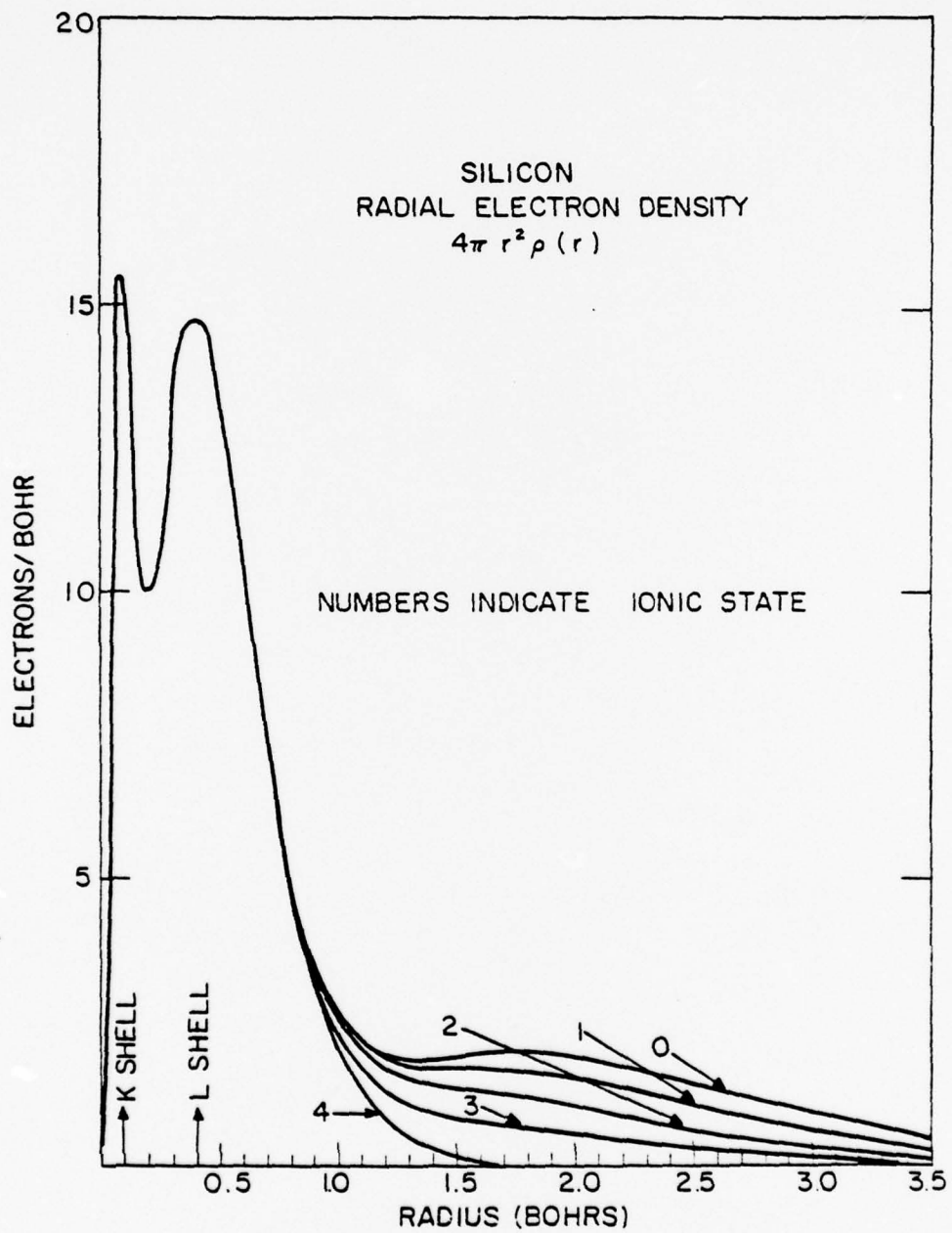


Figure 9 - Silicon Radial Electron Density

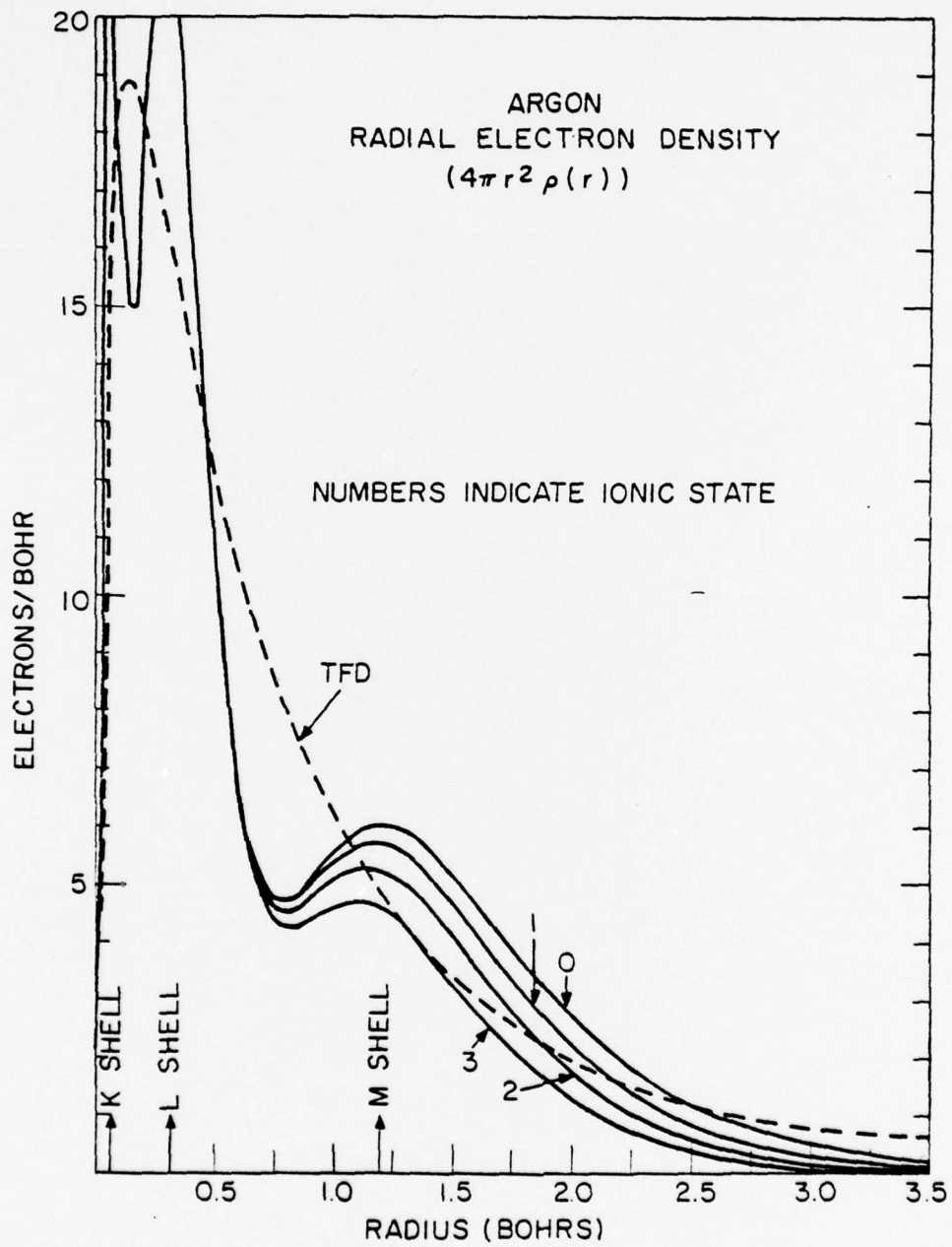


Figure 10 - Argon Radial Electron Density

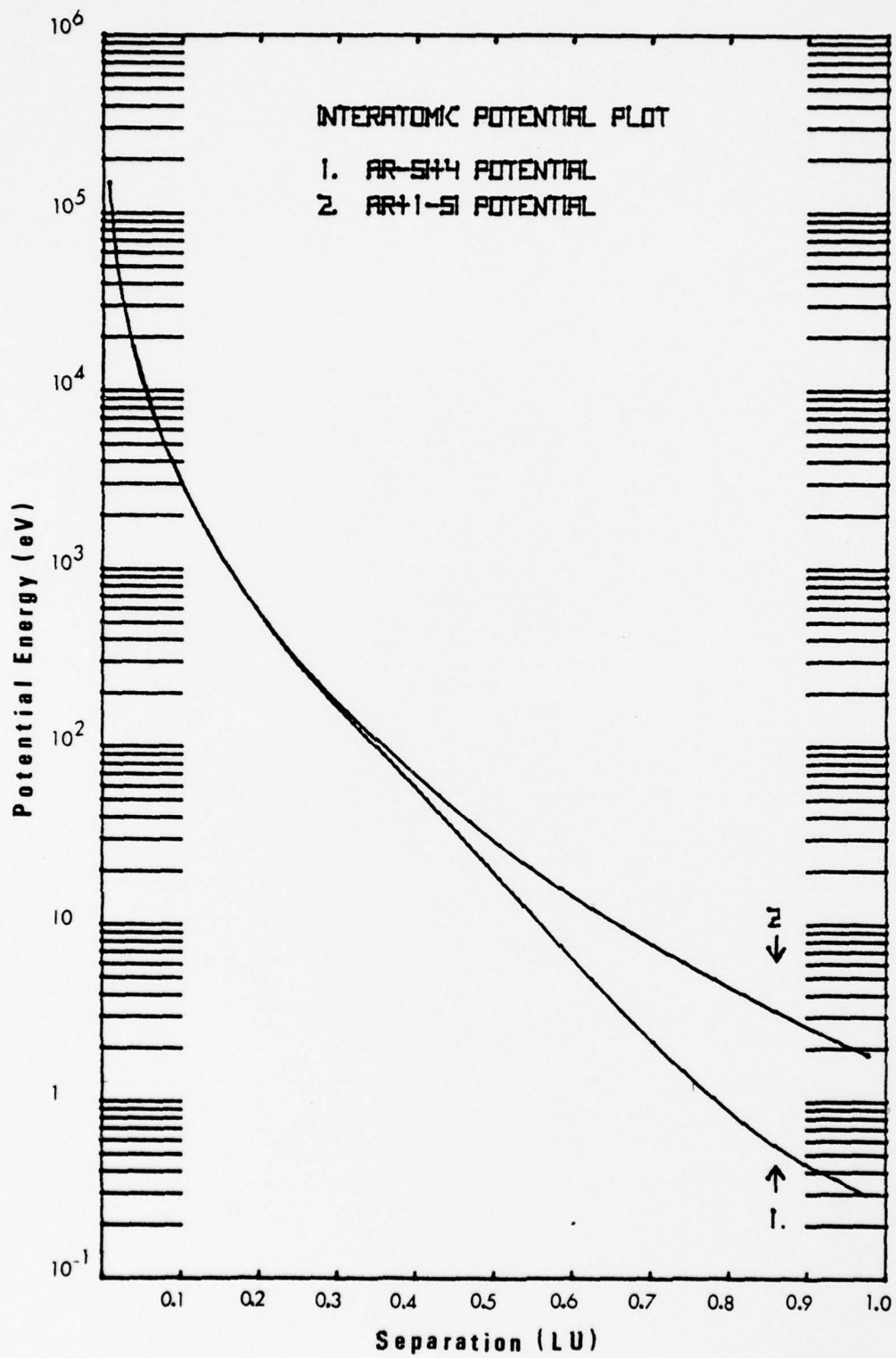


Figure 11 - Argon-Silicon Interaction Potentials

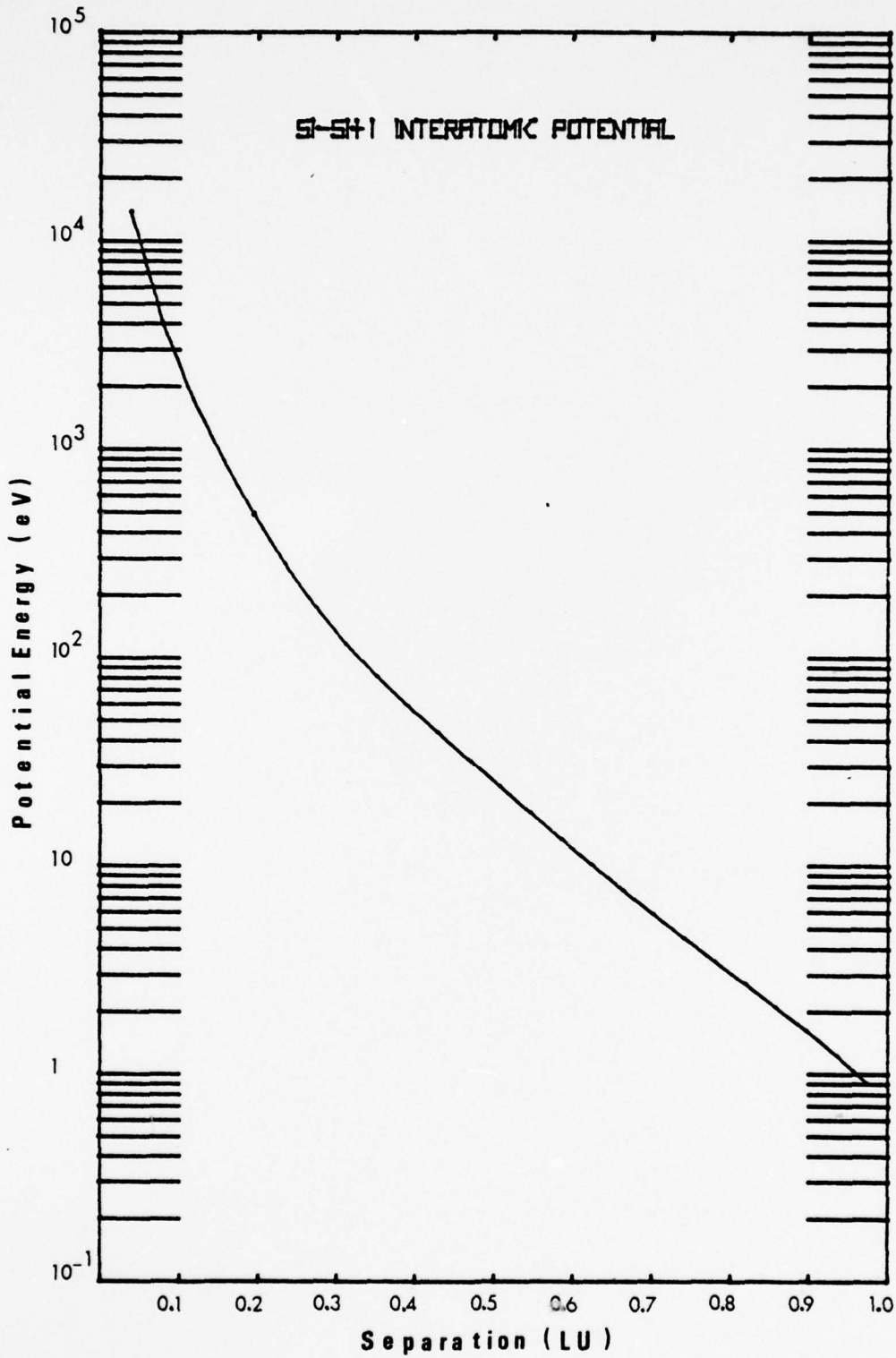


Figure 12 - Si-Si⁺ Interaction Potential

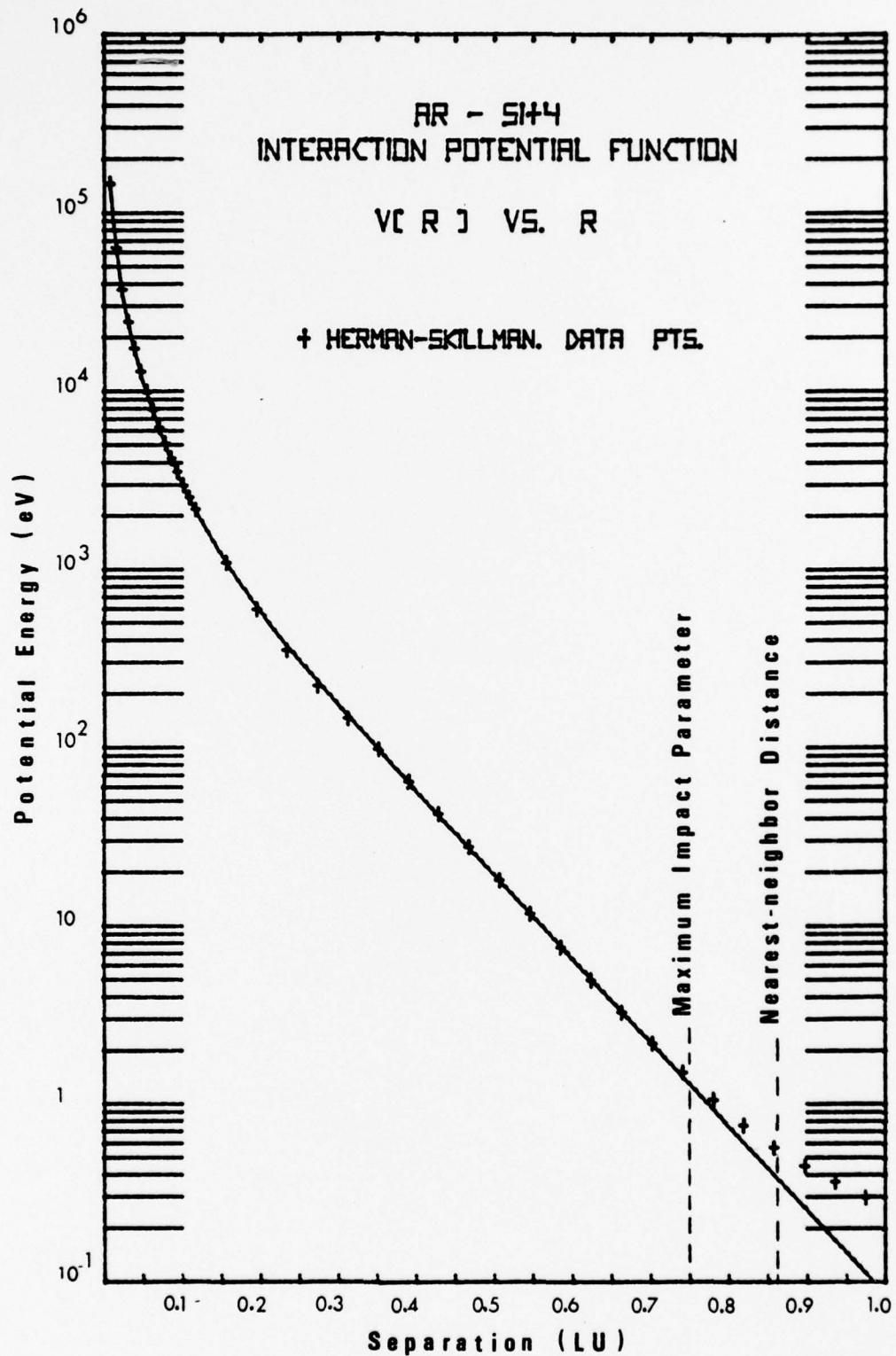


Figure 13 - Ar-Si⁴⁺ Analytic Potential Function

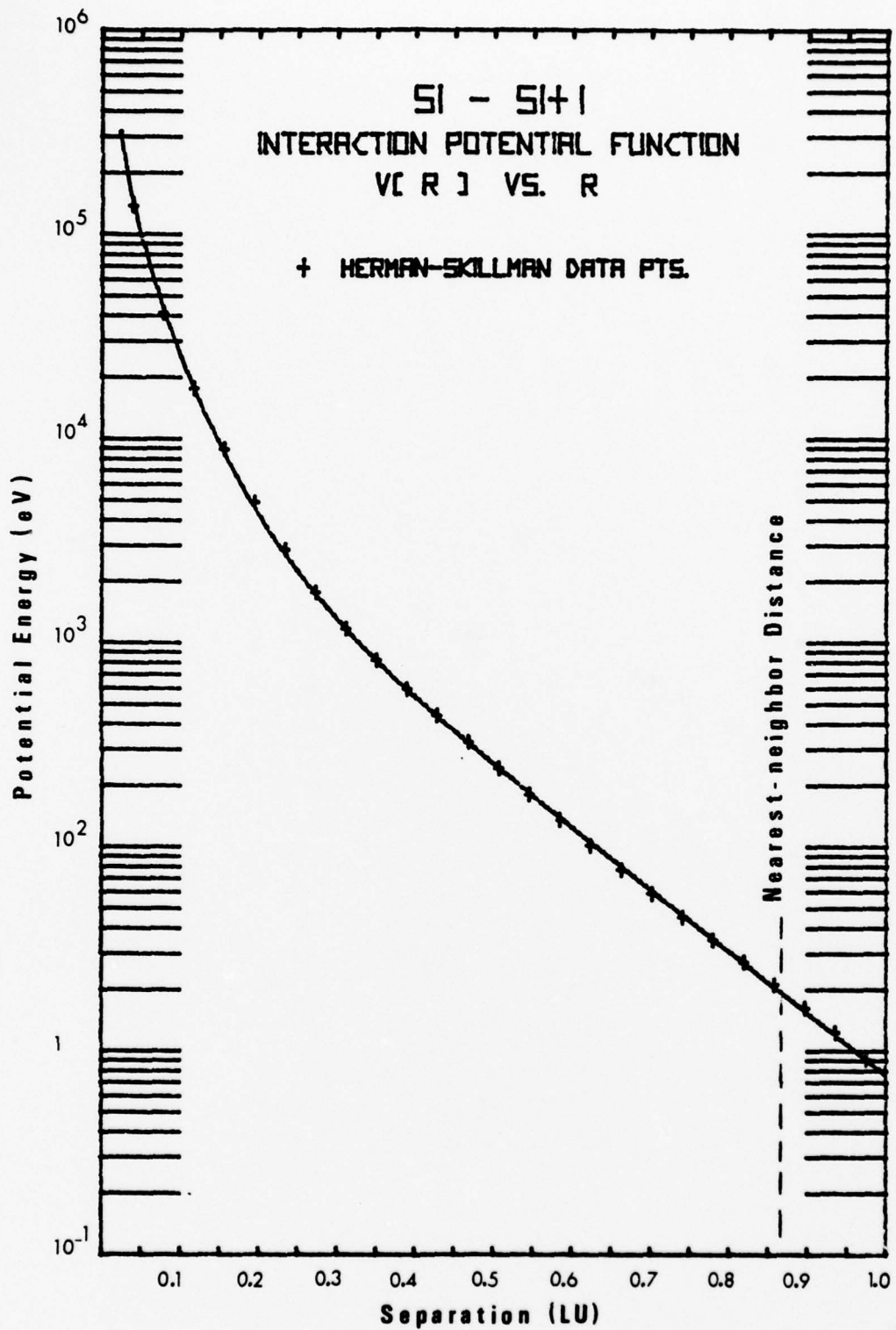


Figure 14 - Si-Si⁺1 Analytic Potential Function

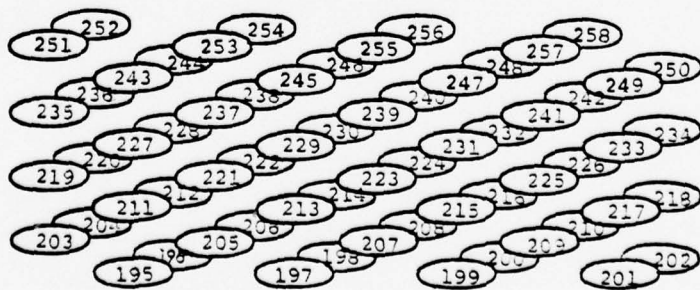
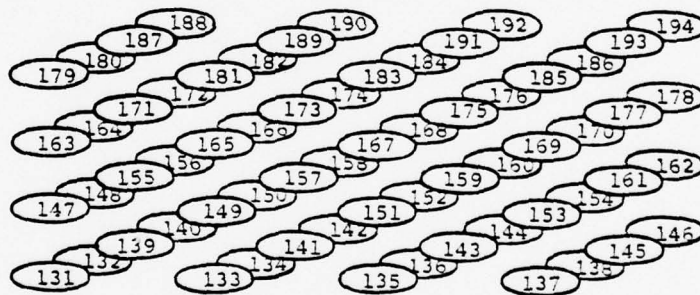
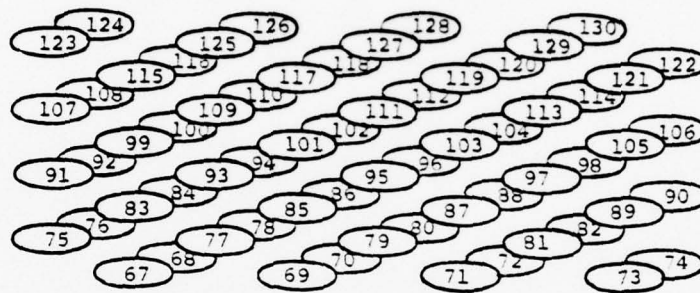
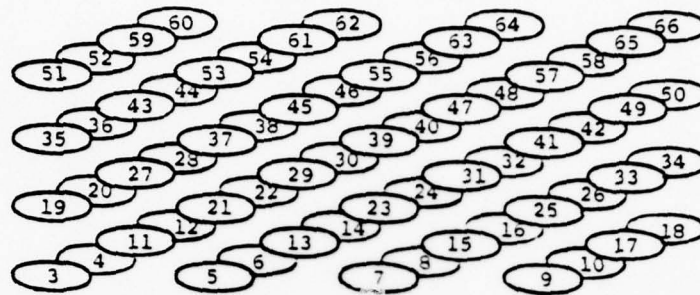


Figure 15 - Silicon Single Crystal [(100) Orientation]

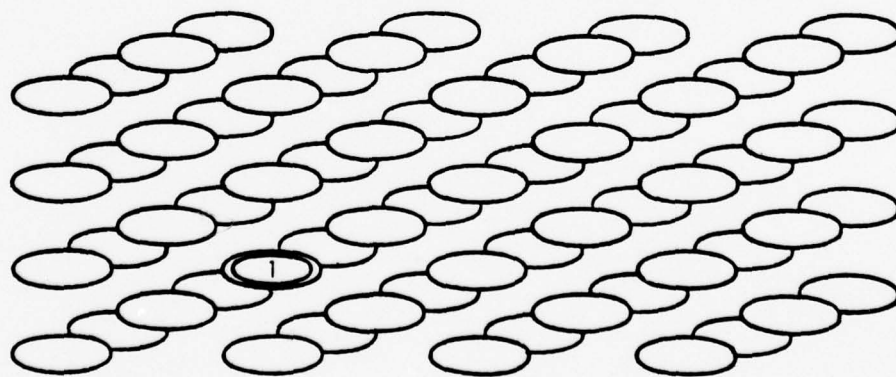
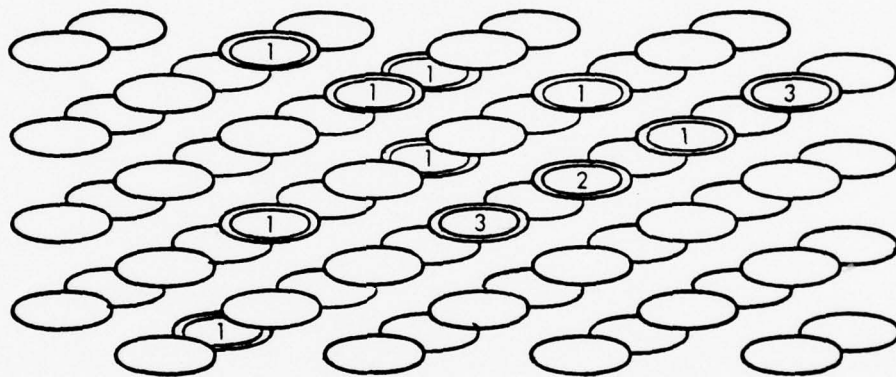
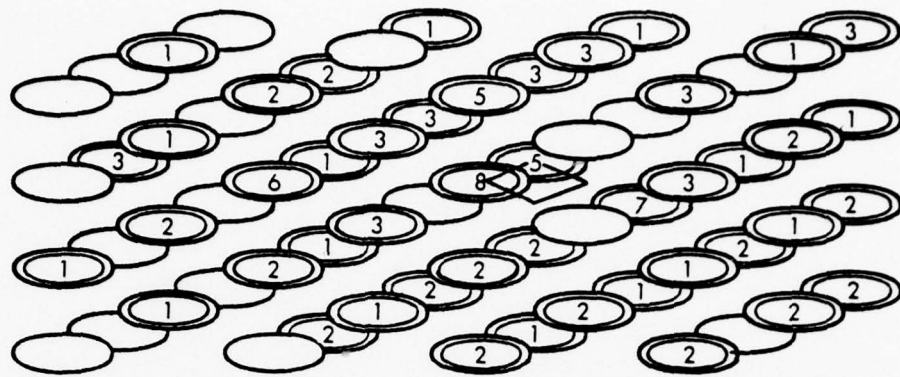


Figure 16 - (100) Orientation, 600-eV Sputtering Events

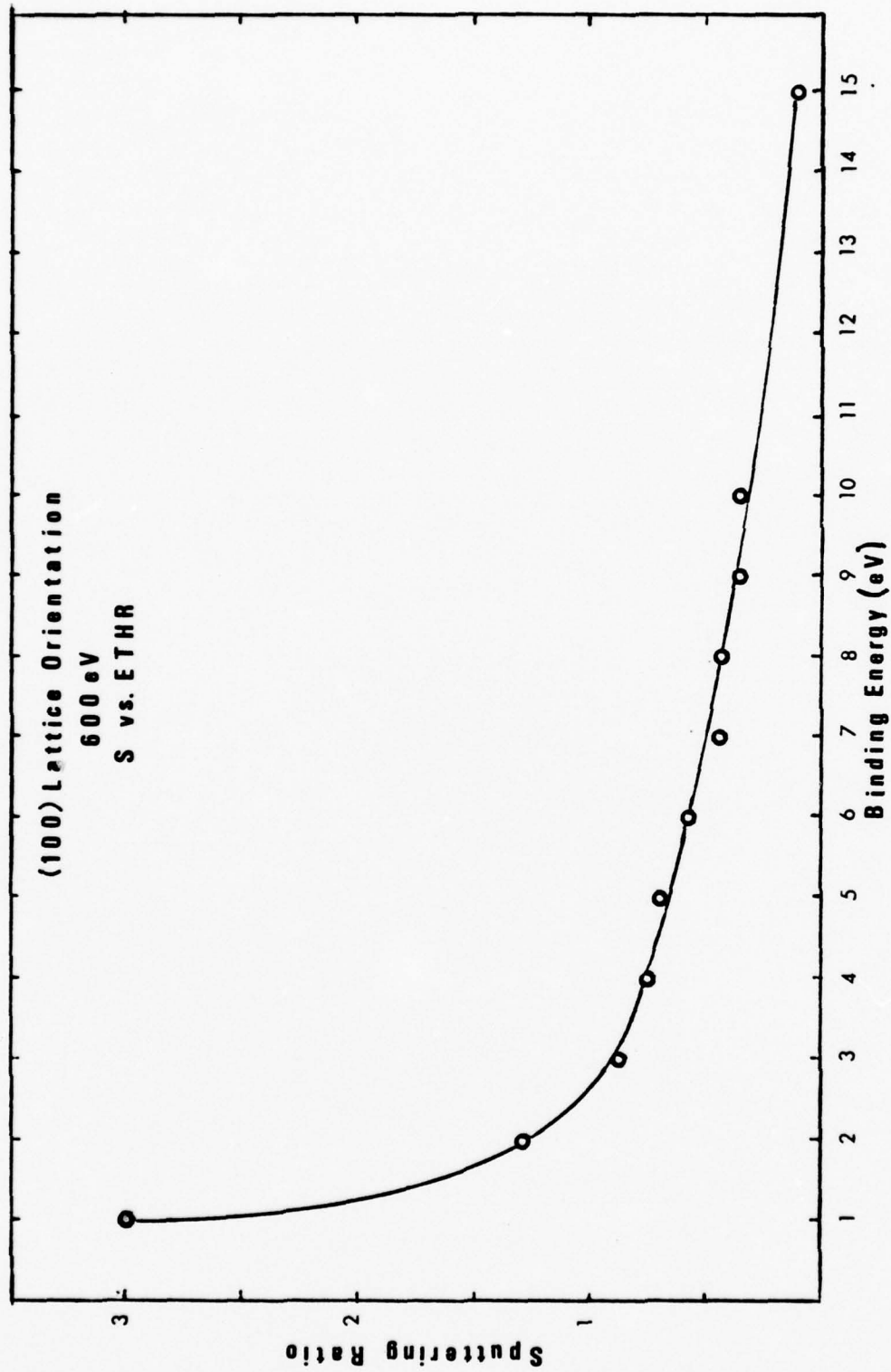


Figure 17

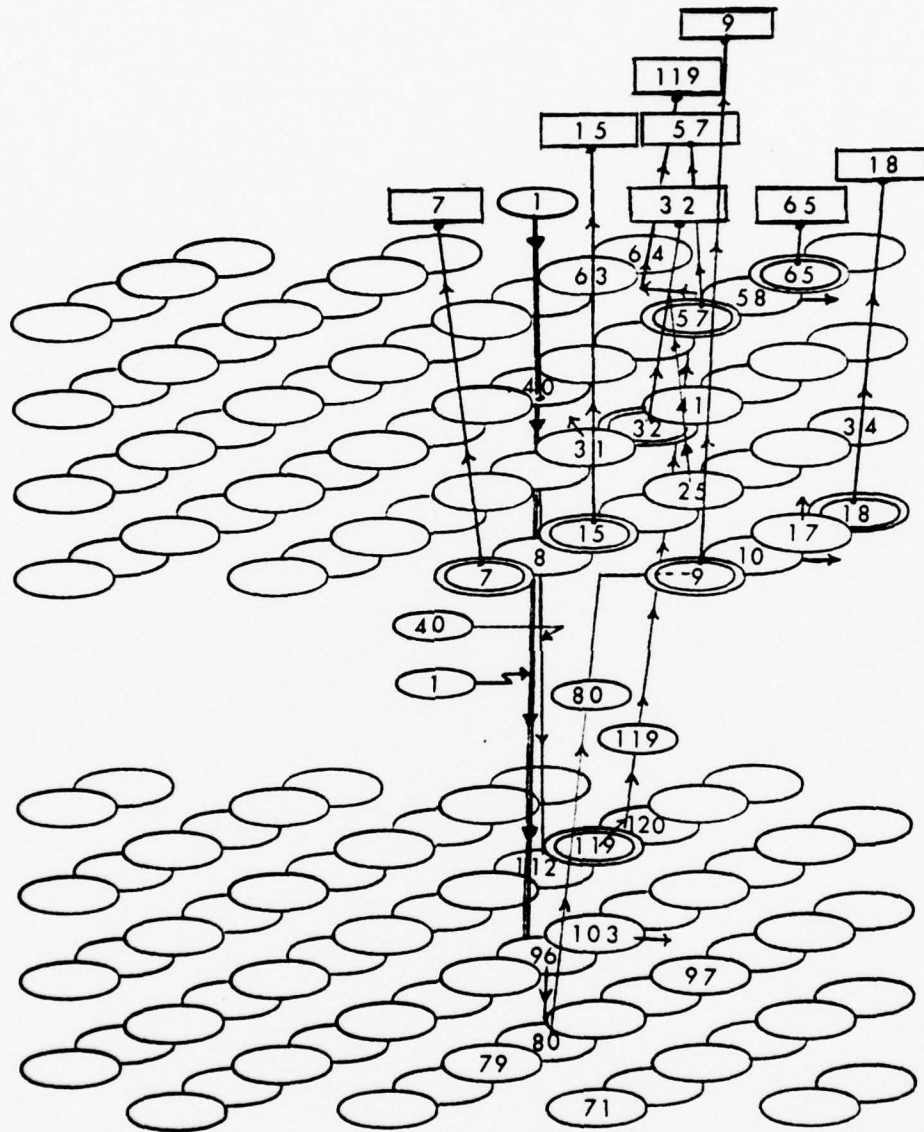
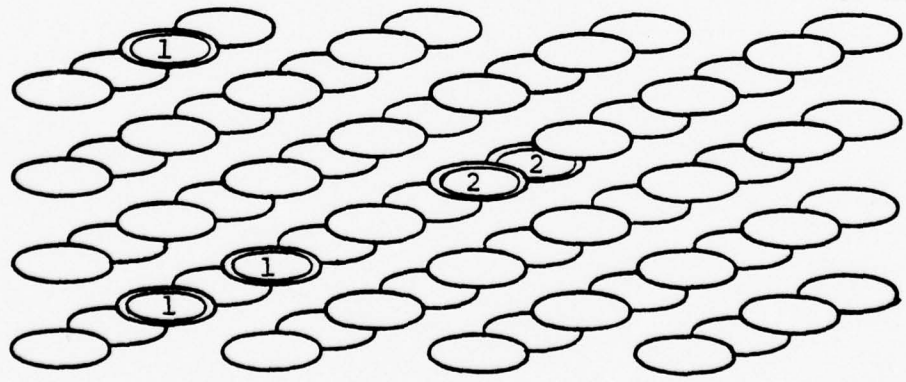
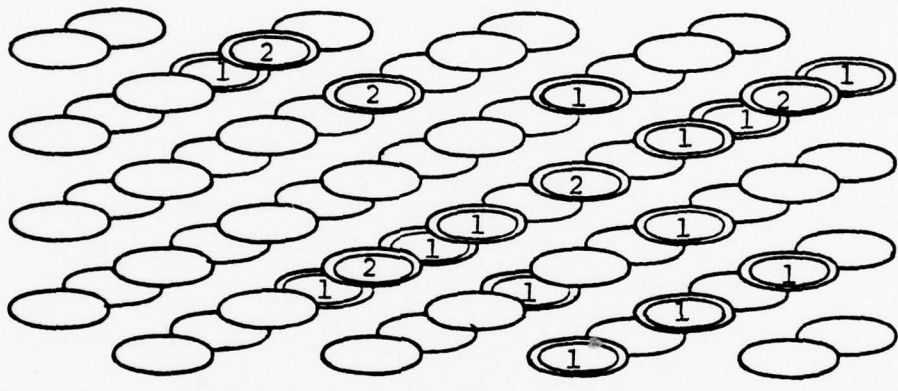
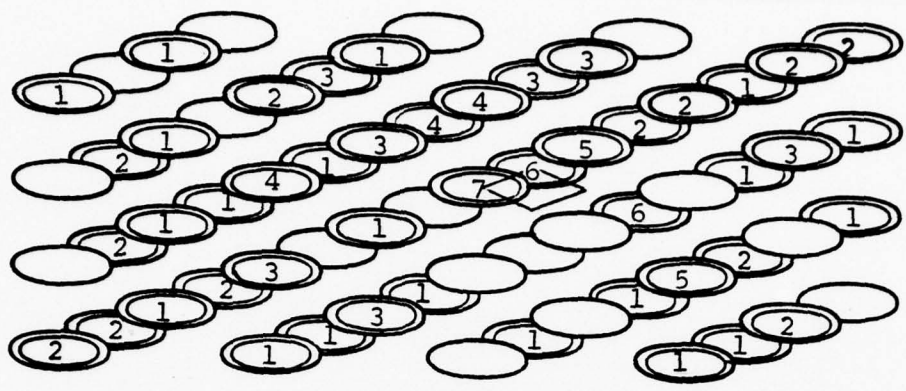


Figure 18 - Sputtering Mechanism Trace
 [600 eV, (100) Orientation]



① Atom 225
(fourth layer)

Figure 19 - (100) Orientation, 1-keV Sputtering Events

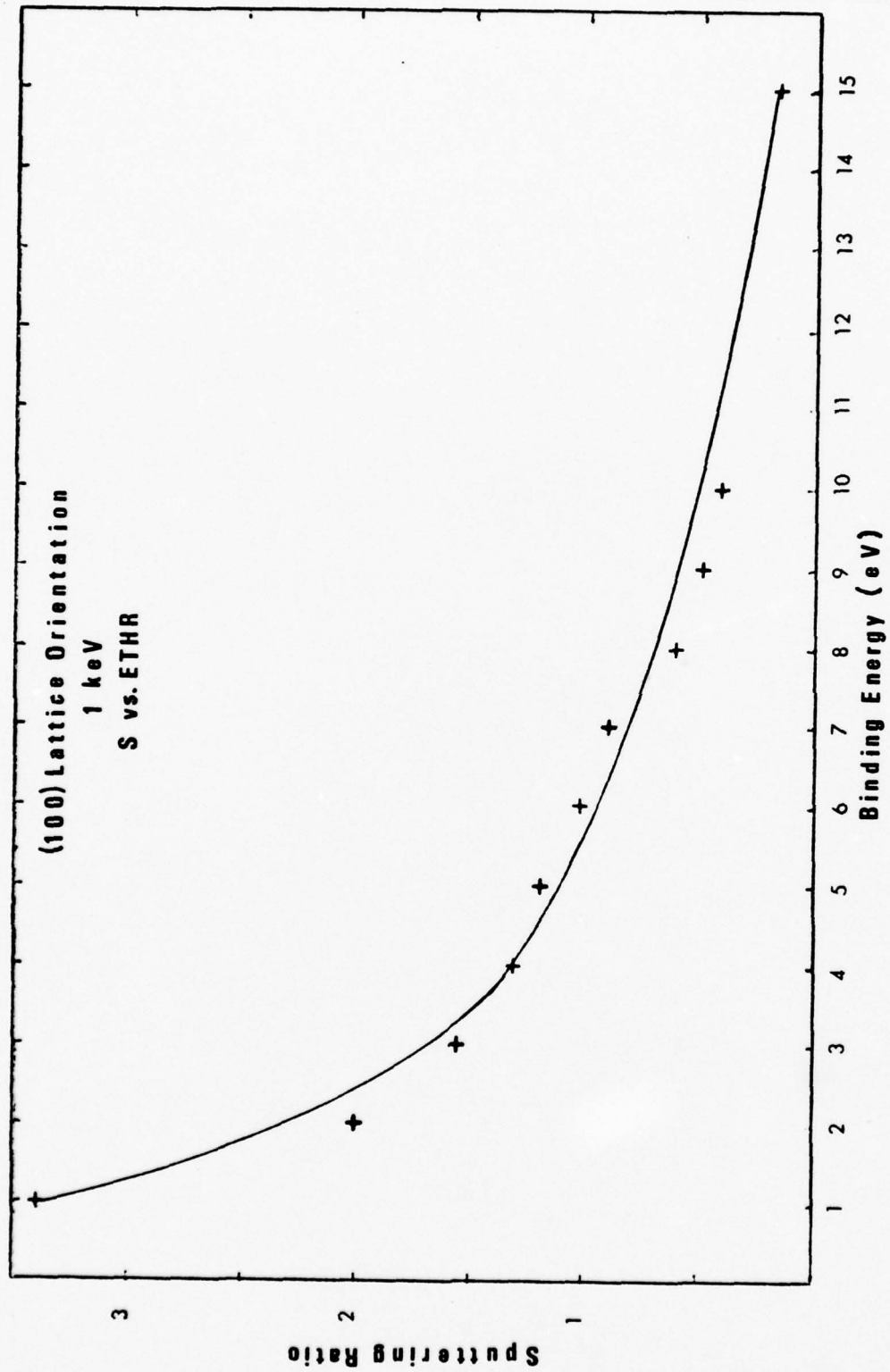


Figure 20

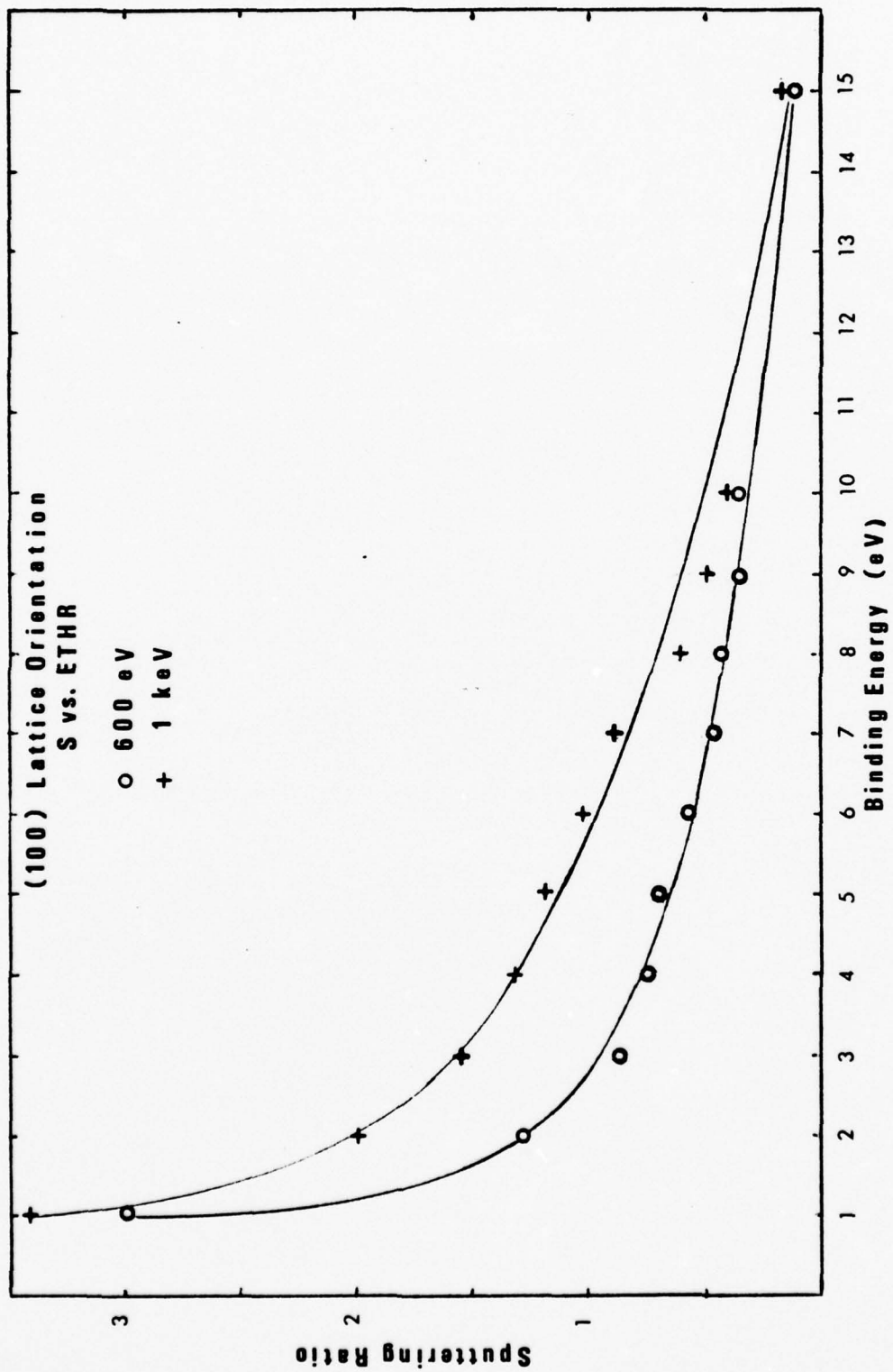


Figure 21

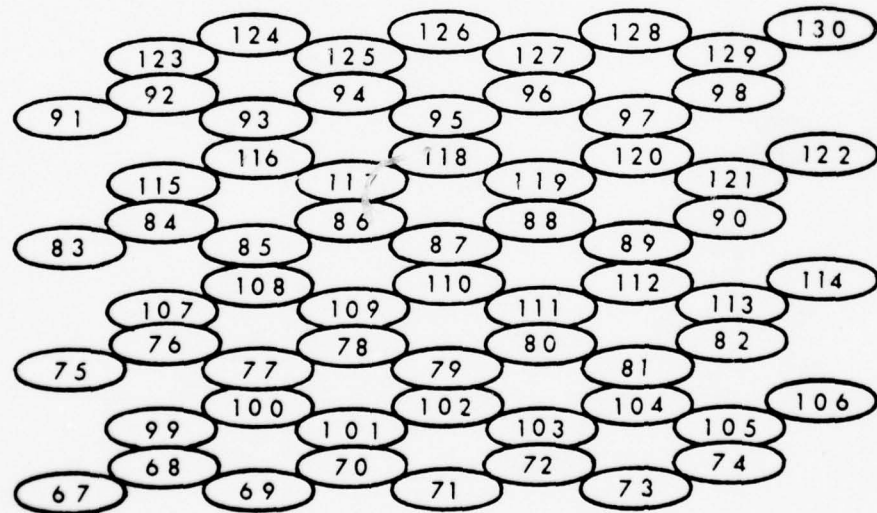
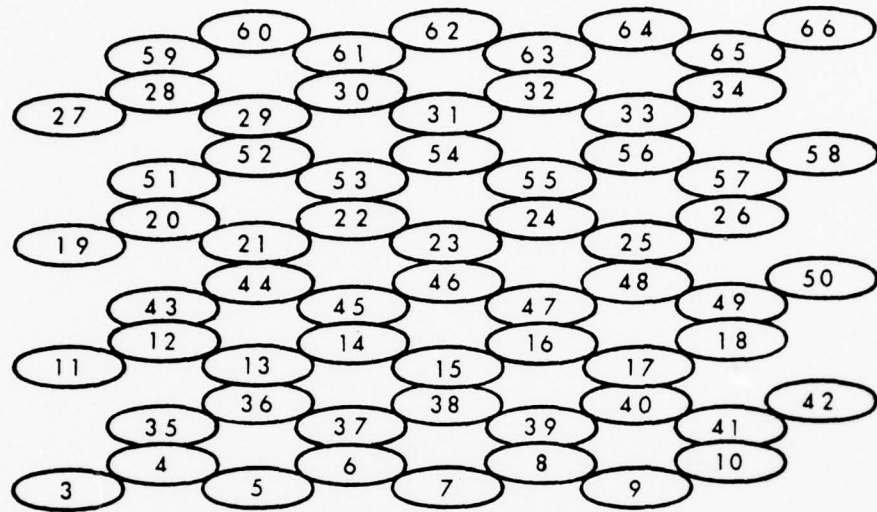


Figure 22 - Silicon Single Crystal [(110) Orientation]

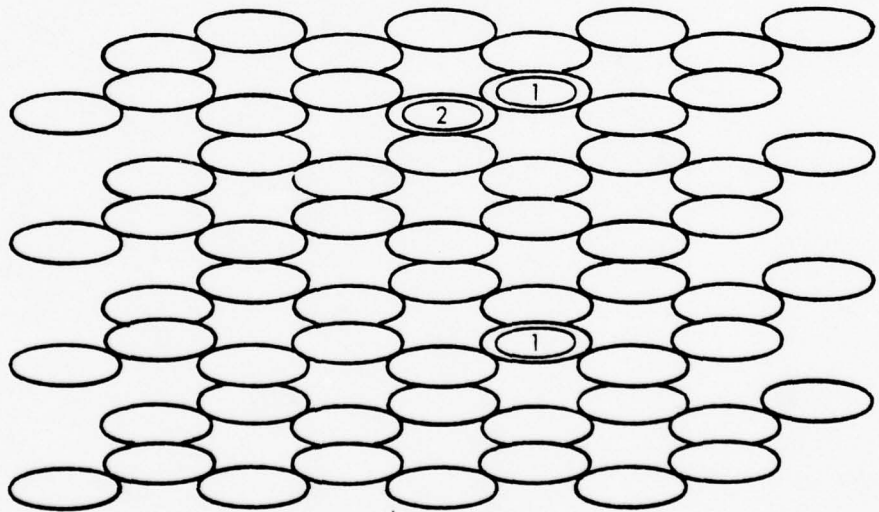
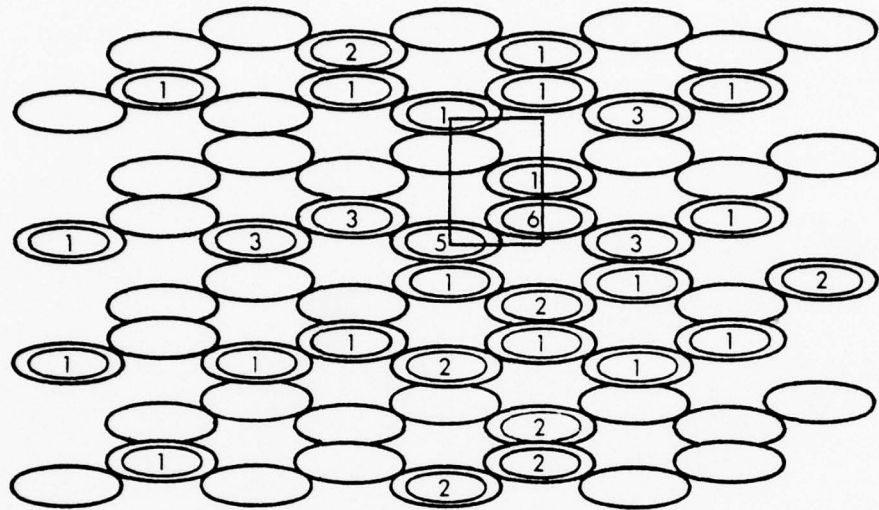


Figure 23 - (110) Orientation, 600-eV Sputtering Events

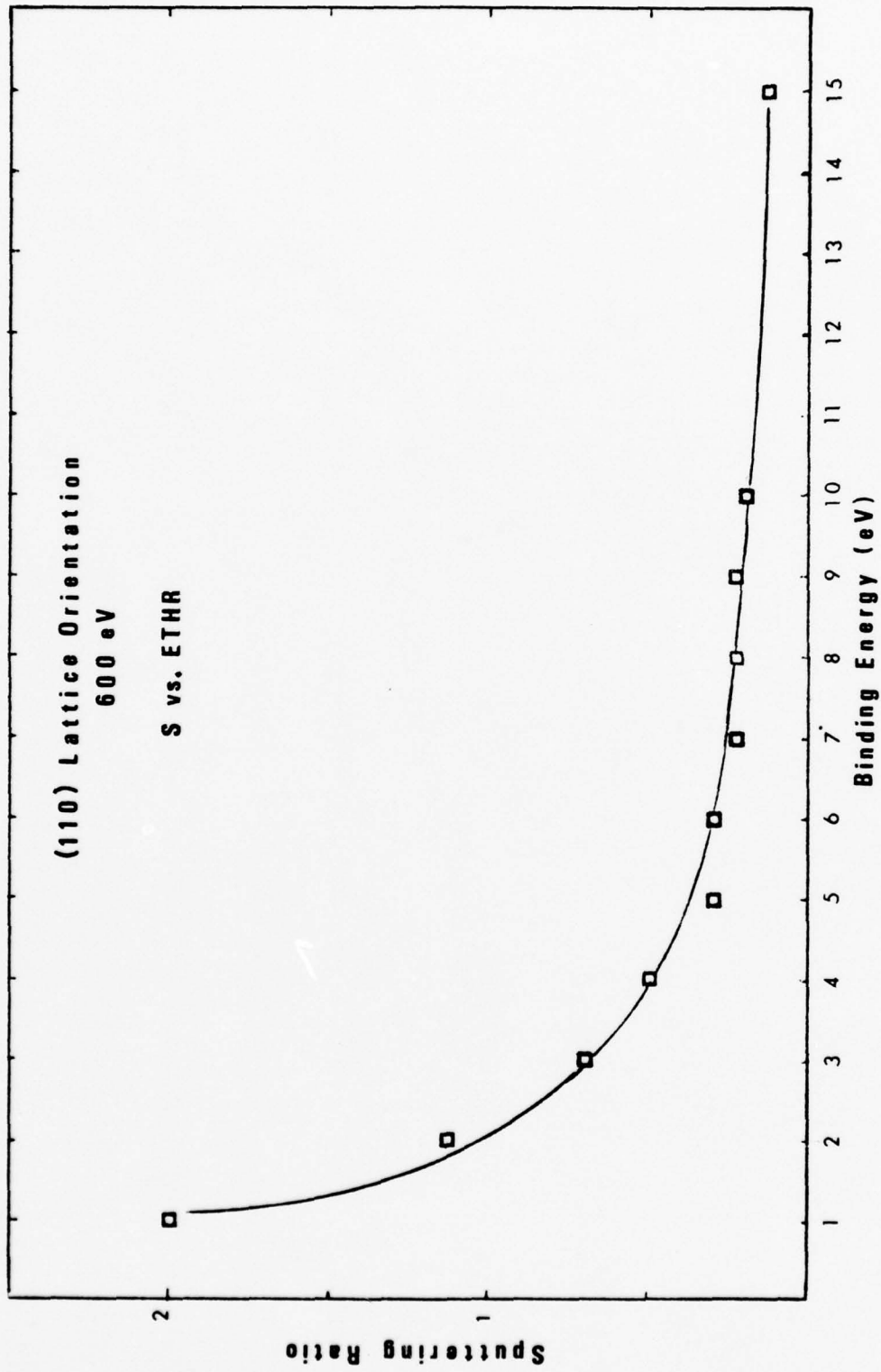


Figure 24

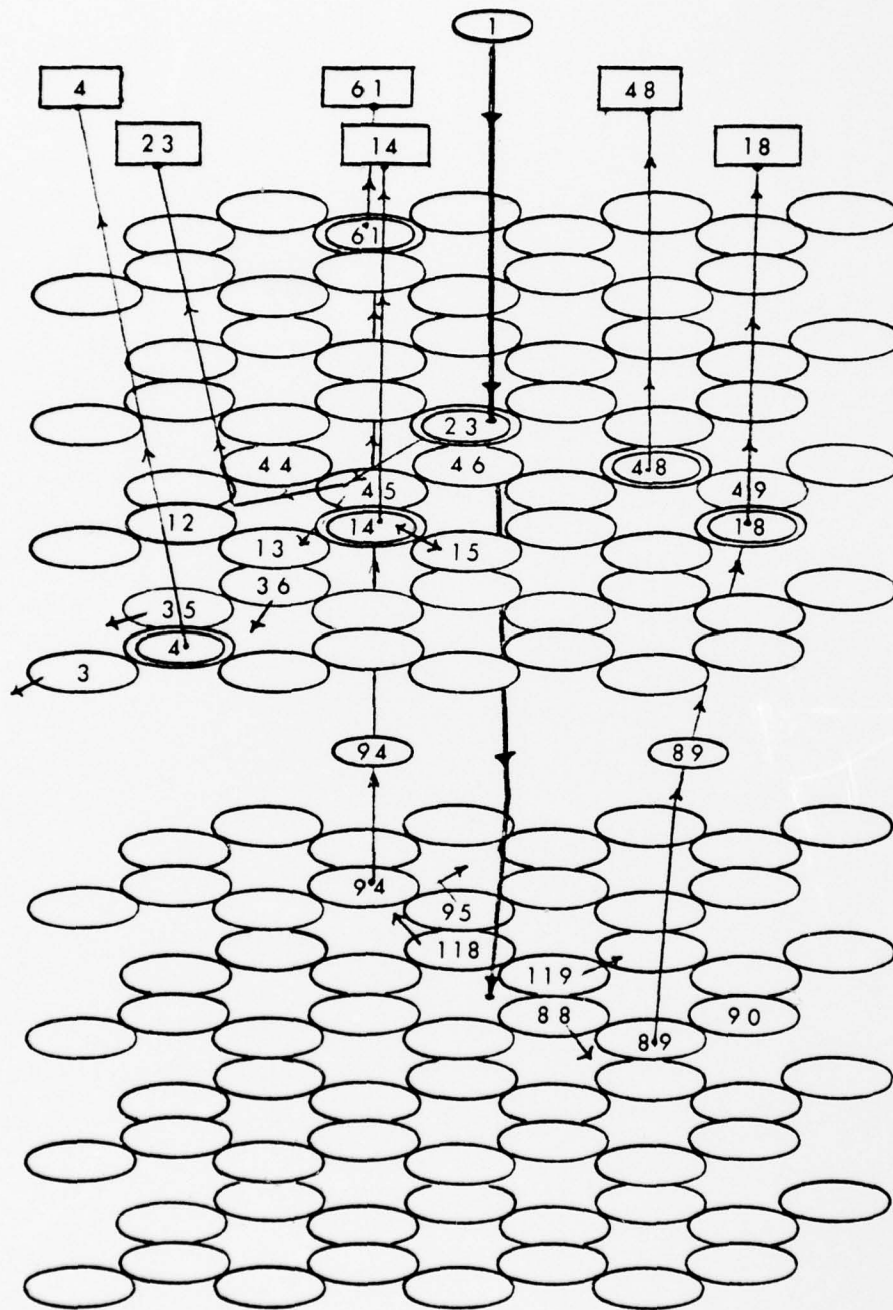


Figure 25 - Sputtering Mechanism Trace
 [600 eV, (110) Orientation]

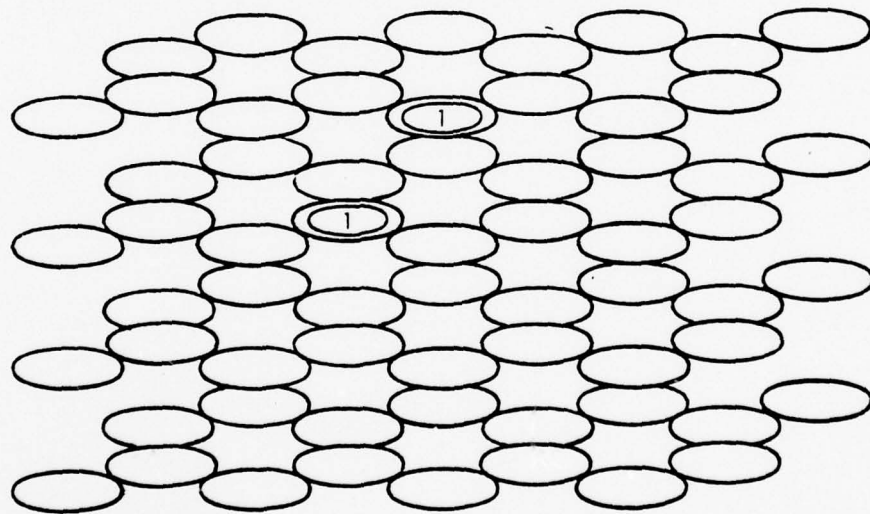
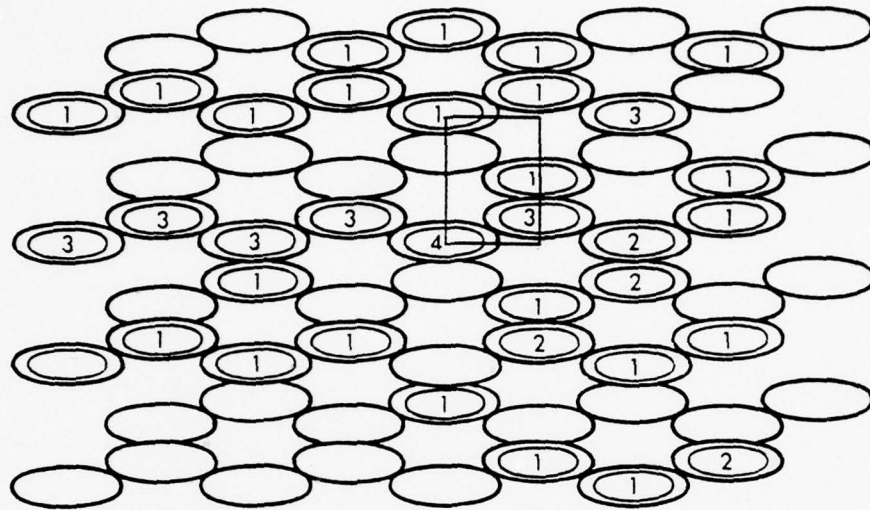


Figure 26 - (110) Orientation, 1-keV Sputtering Events

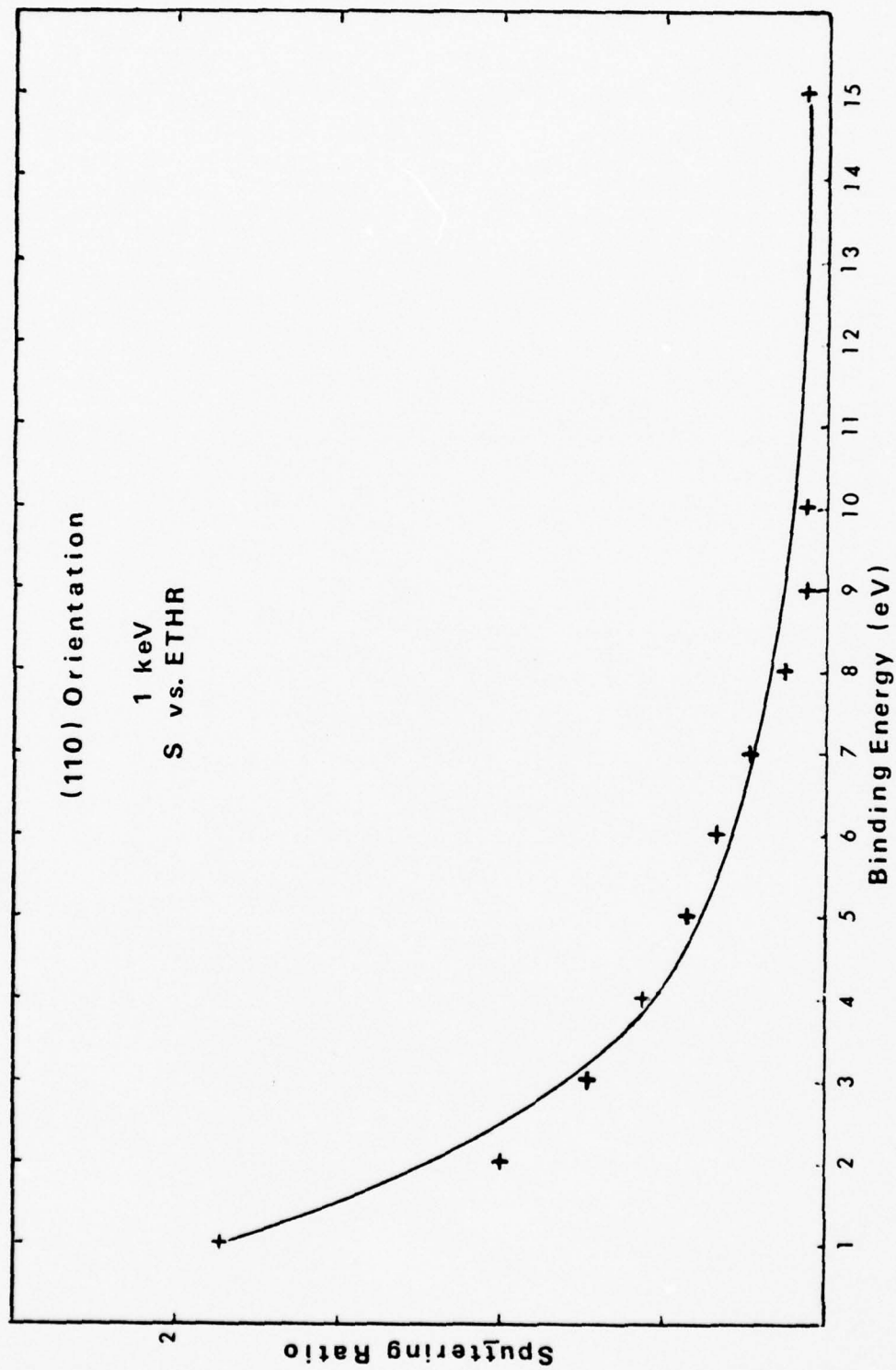


Figure 27

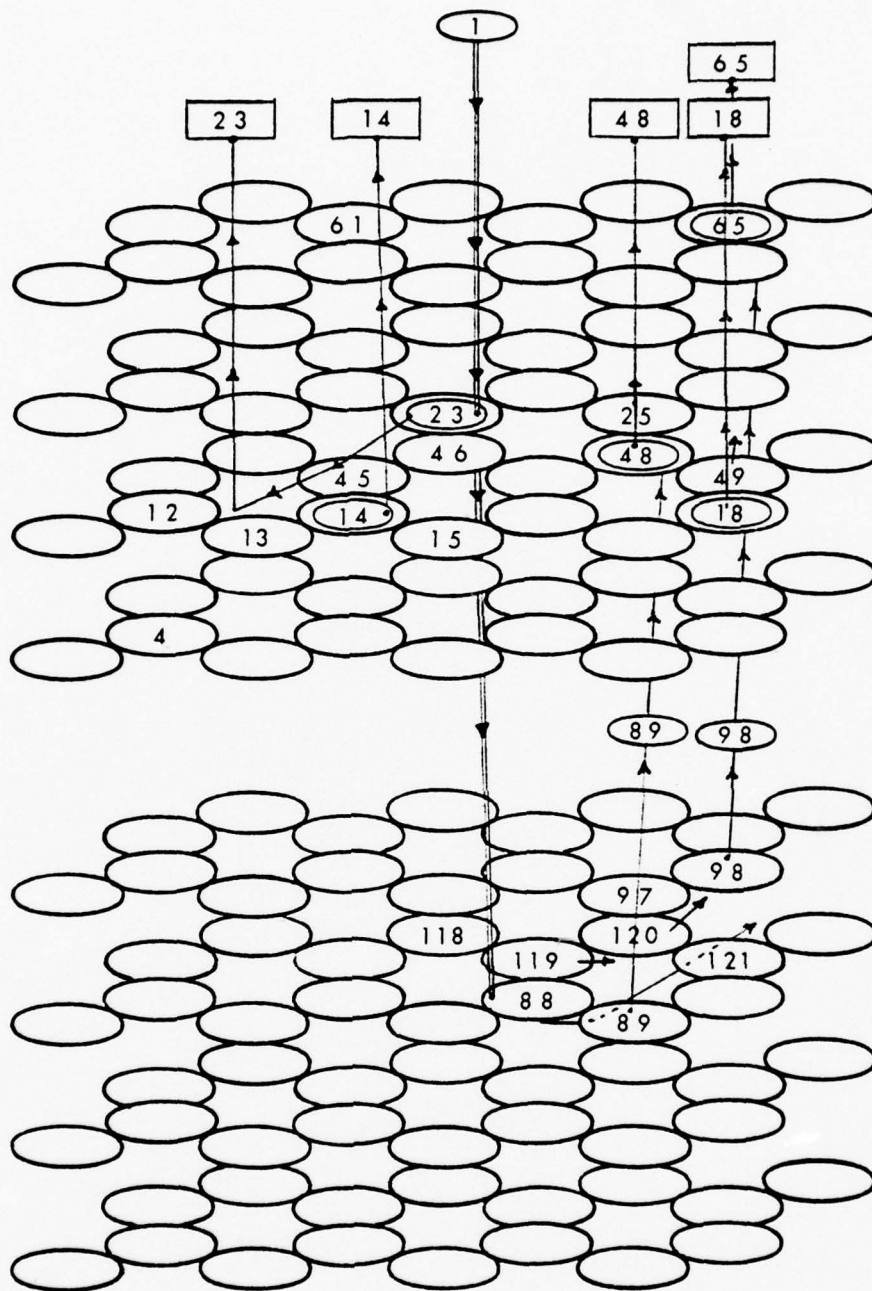
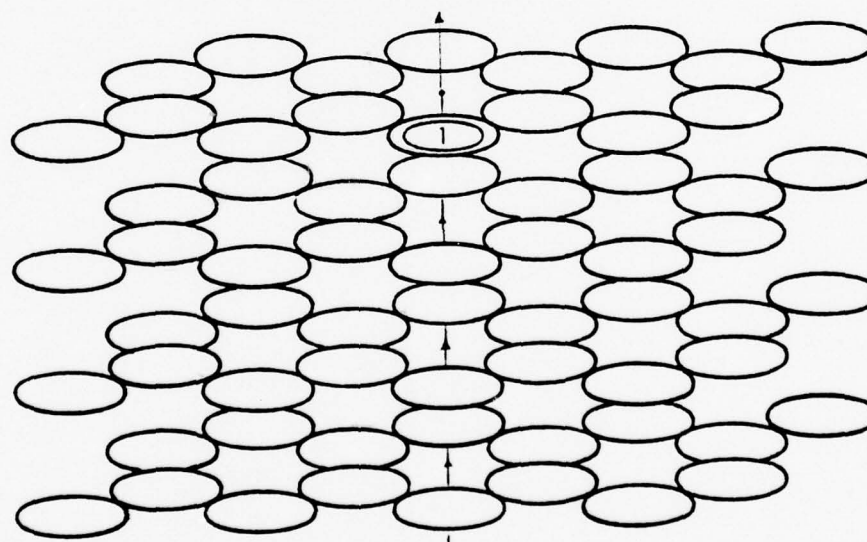
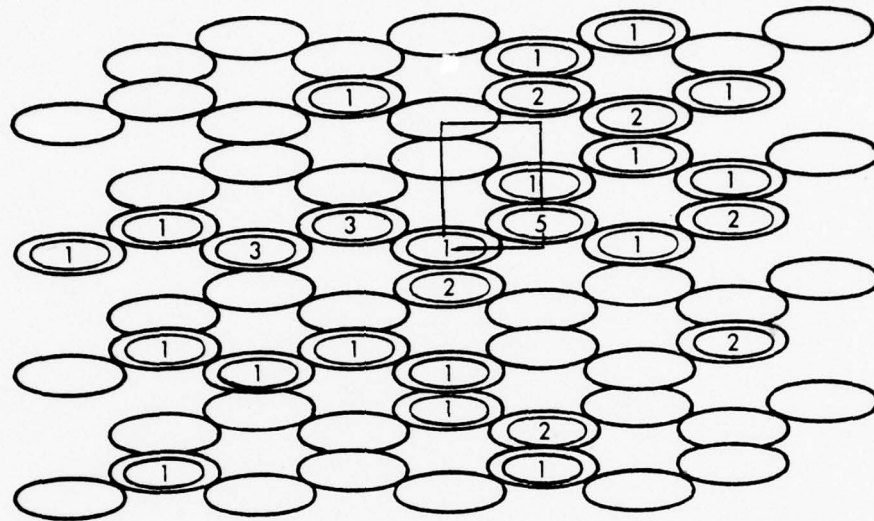


Figure 28 - Sputtering Mechanism Trace
 [1 keV, (110) Orientation]



Atom 223 (fourth layer)

Figure 29 - (110) Orientation, 2-keV Sputtering Events

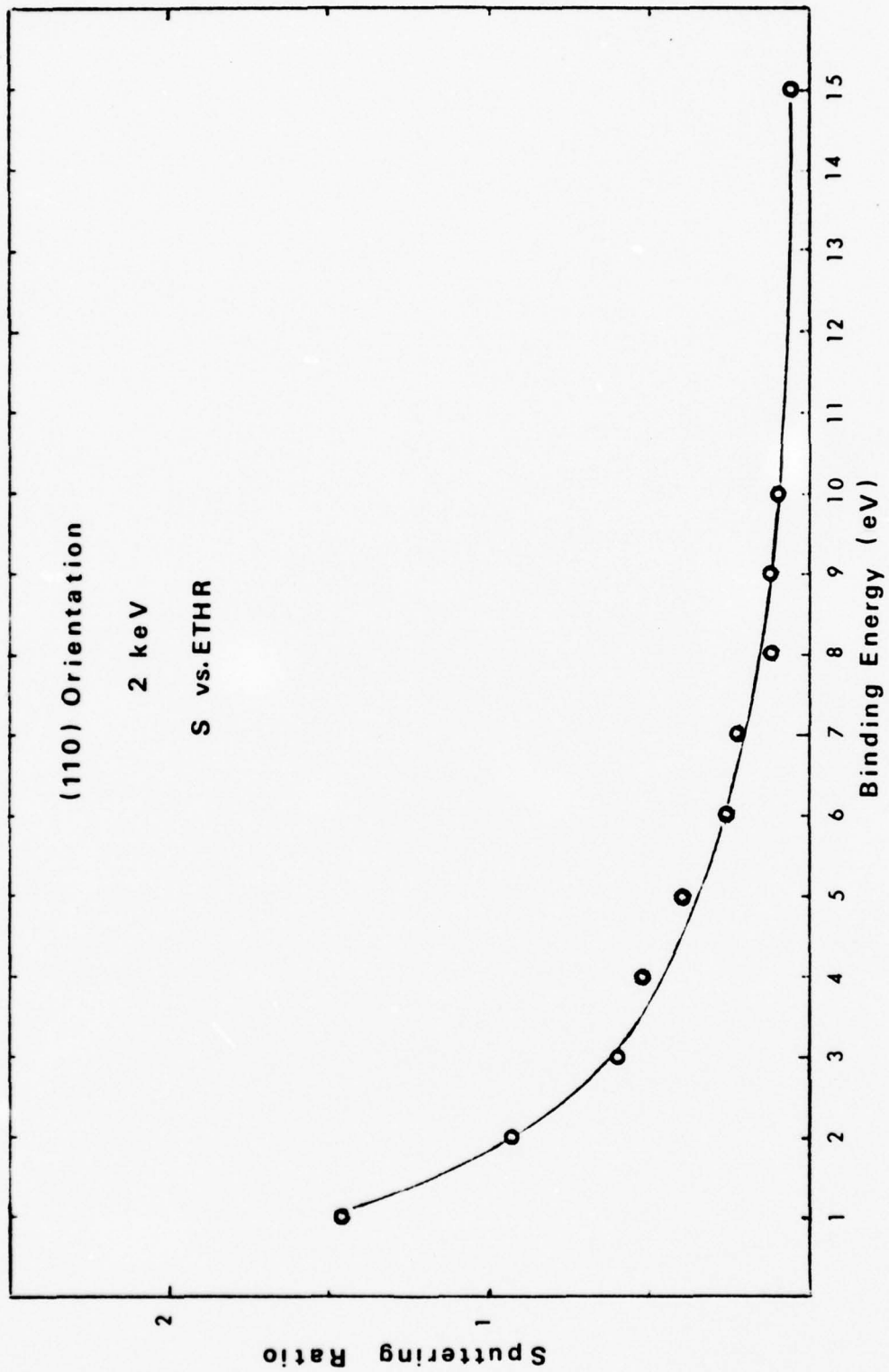


Figure 30

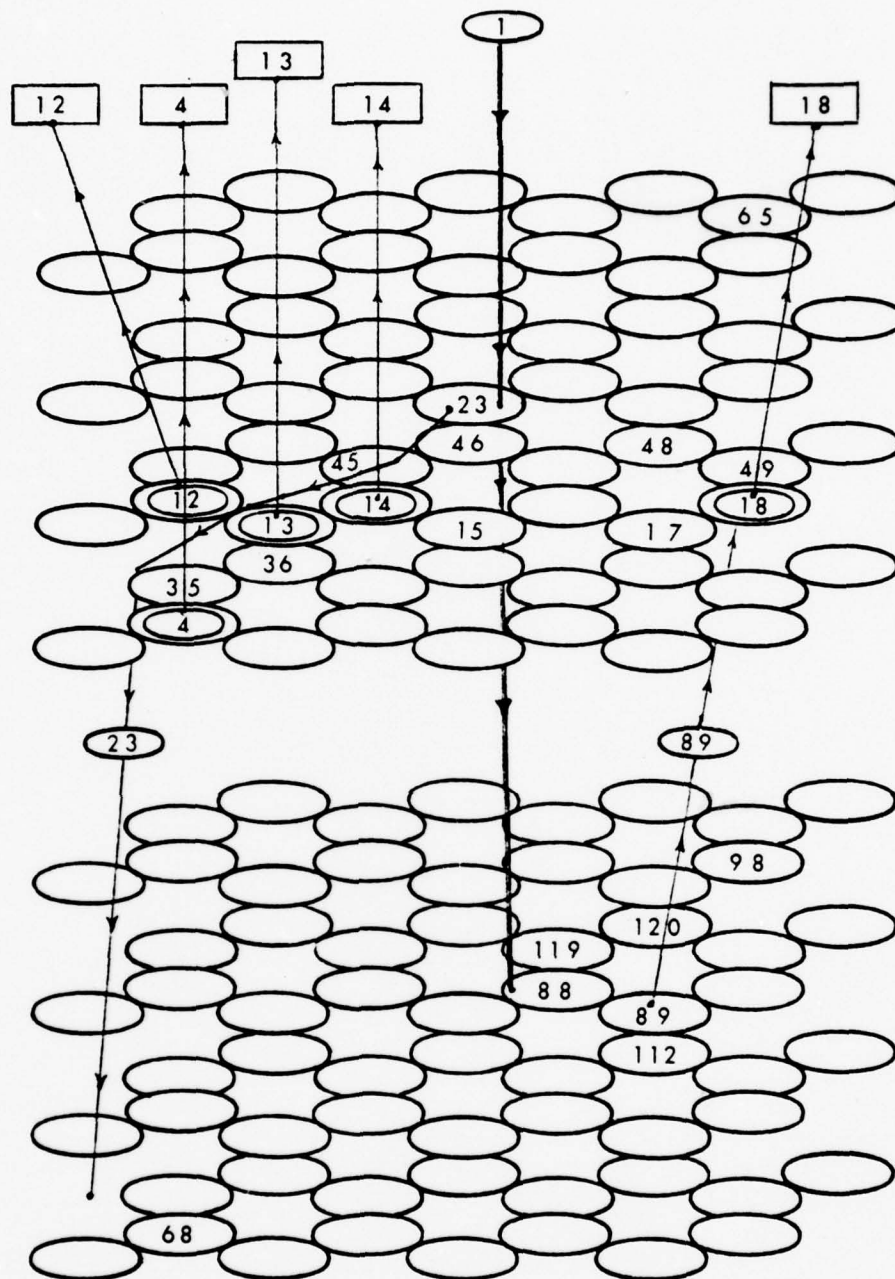


Figure 31 - Sputtering Mechanism Trace
 [2 keV, (110) Orientation]

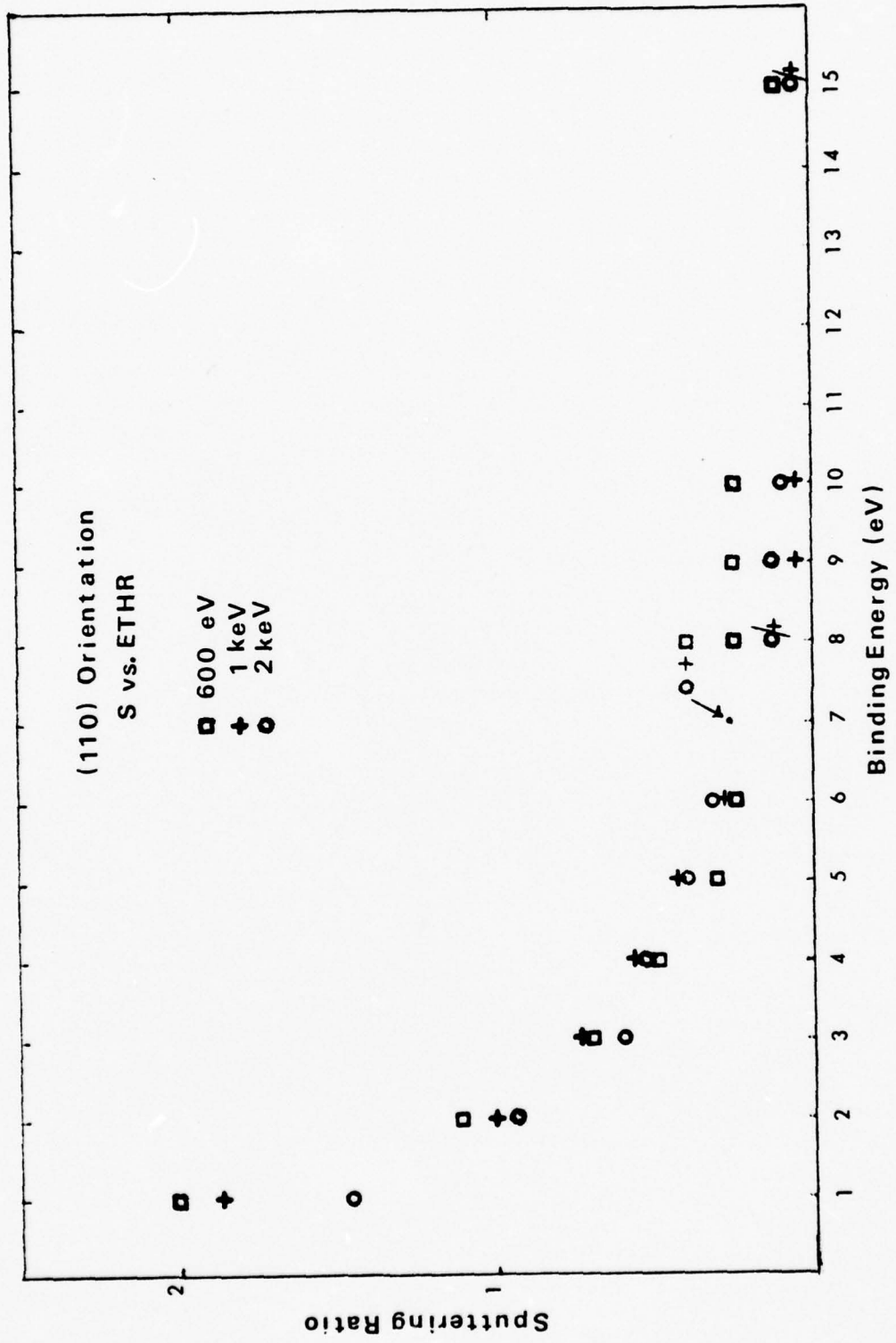


Figure 32

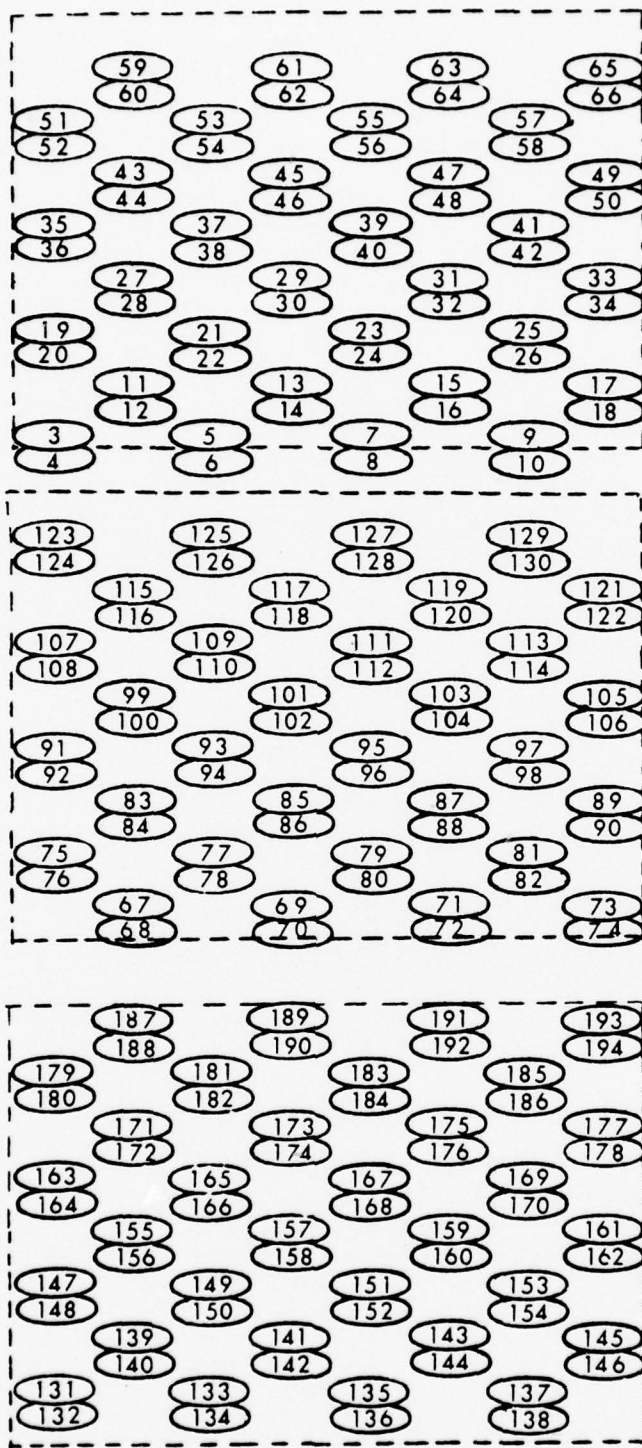


Figure 33 - Silicon Single Crystal [(111) Orientation]

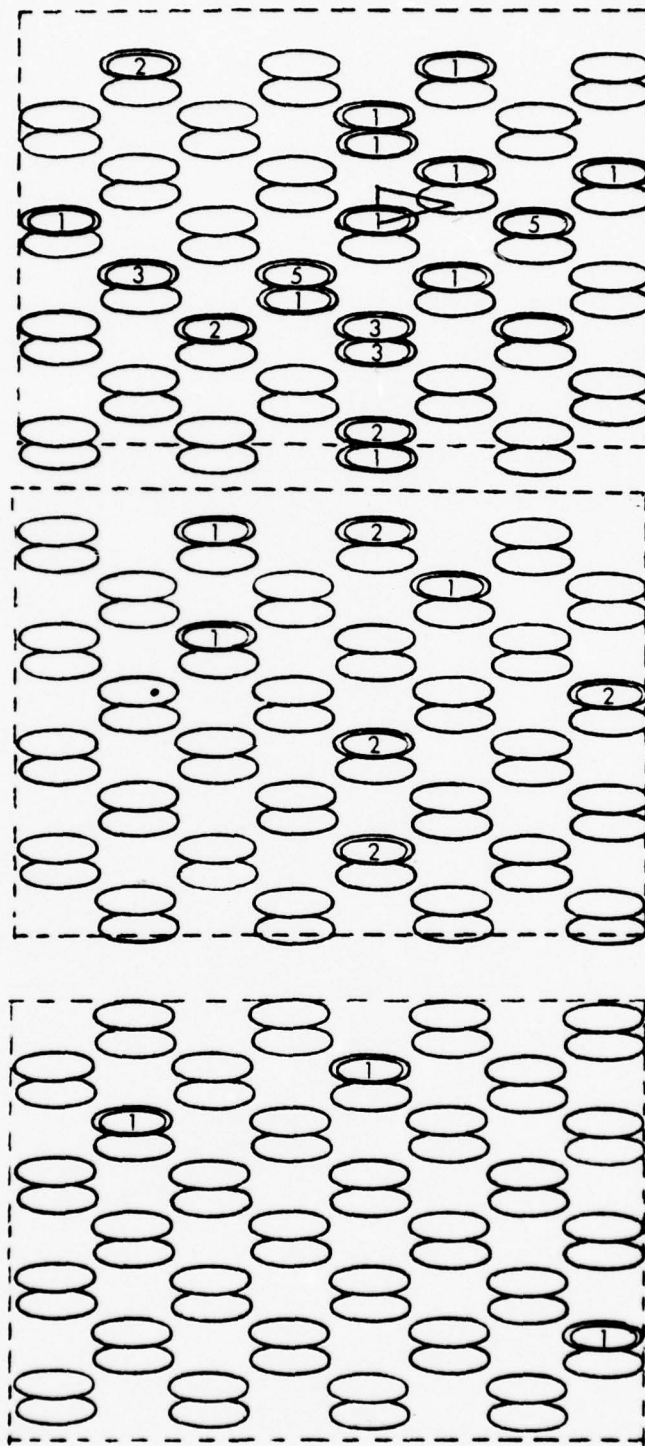


Figure 34. - (111) Orientation, 600-eV Sputtering Events

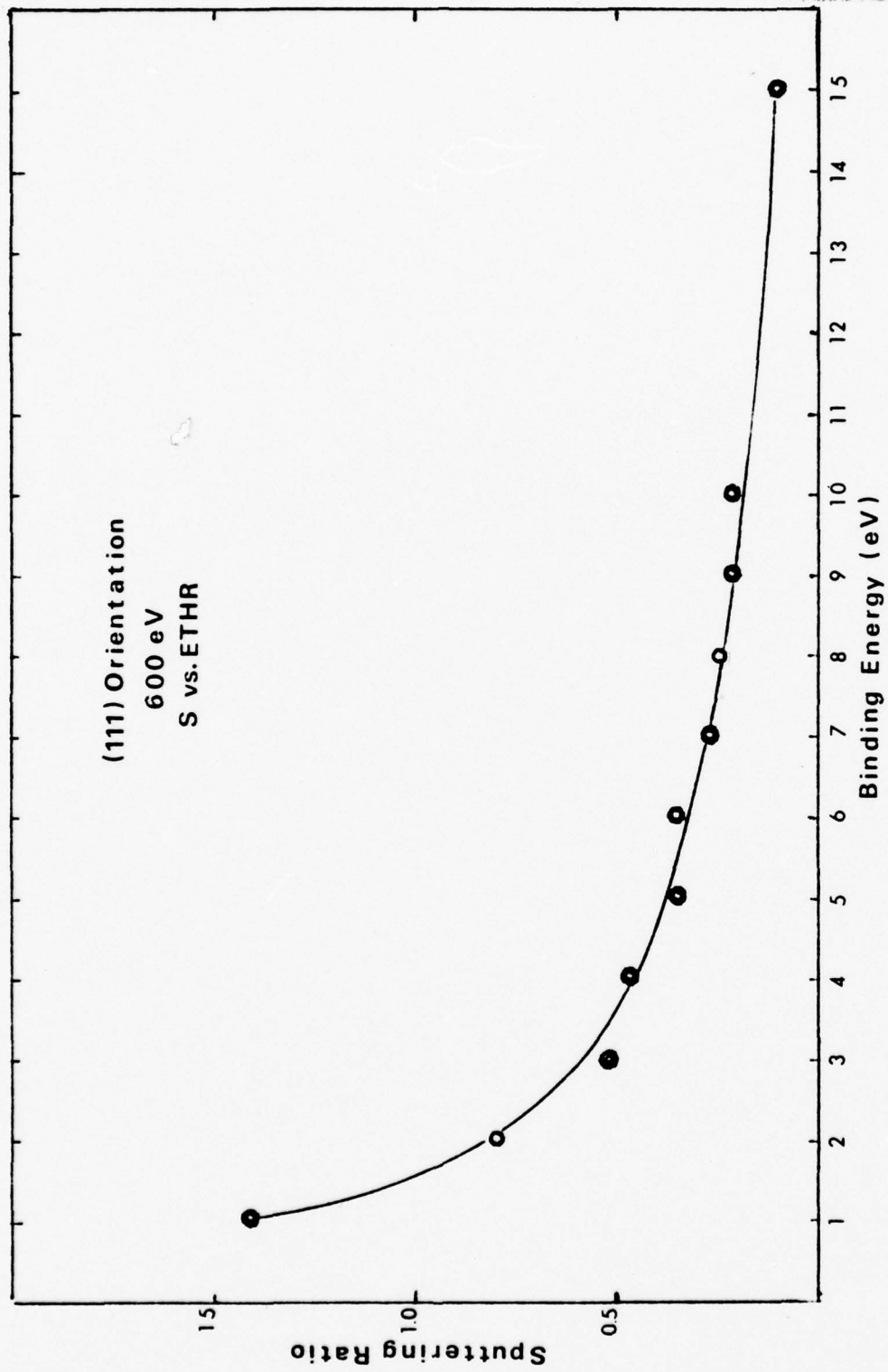


Figure 35

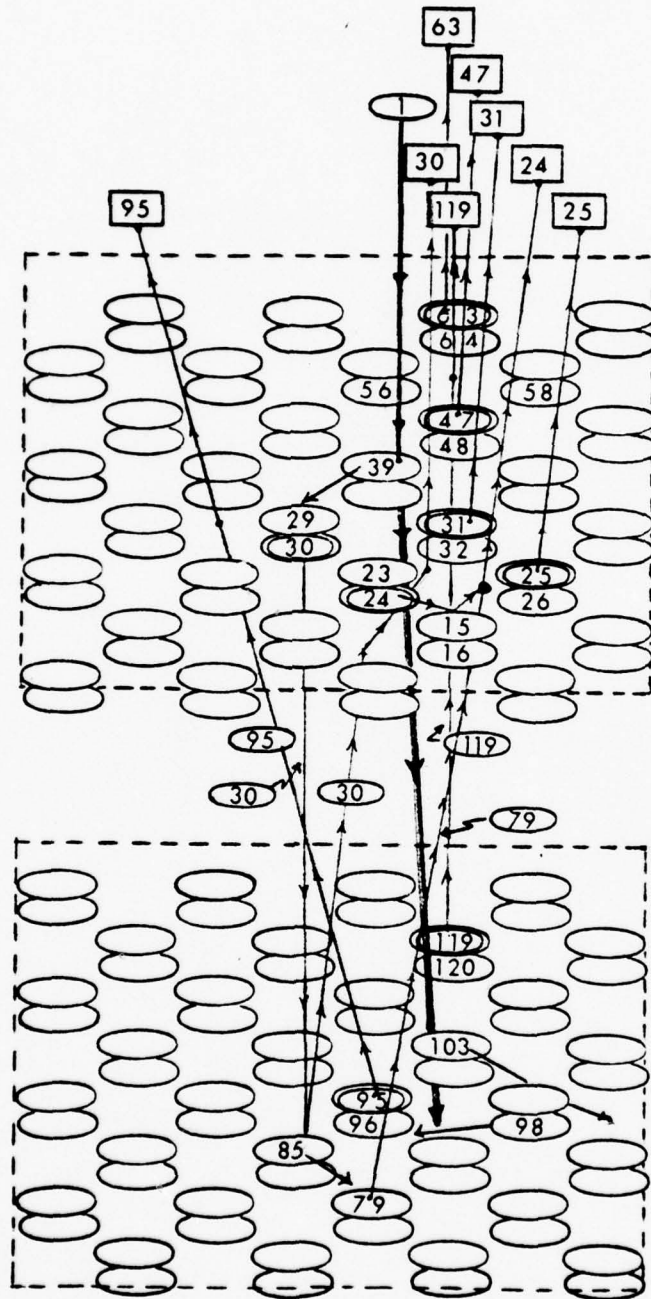


Figure 36 - Sputtering Mechanism Trace
[600 eV, (111) Orientation]

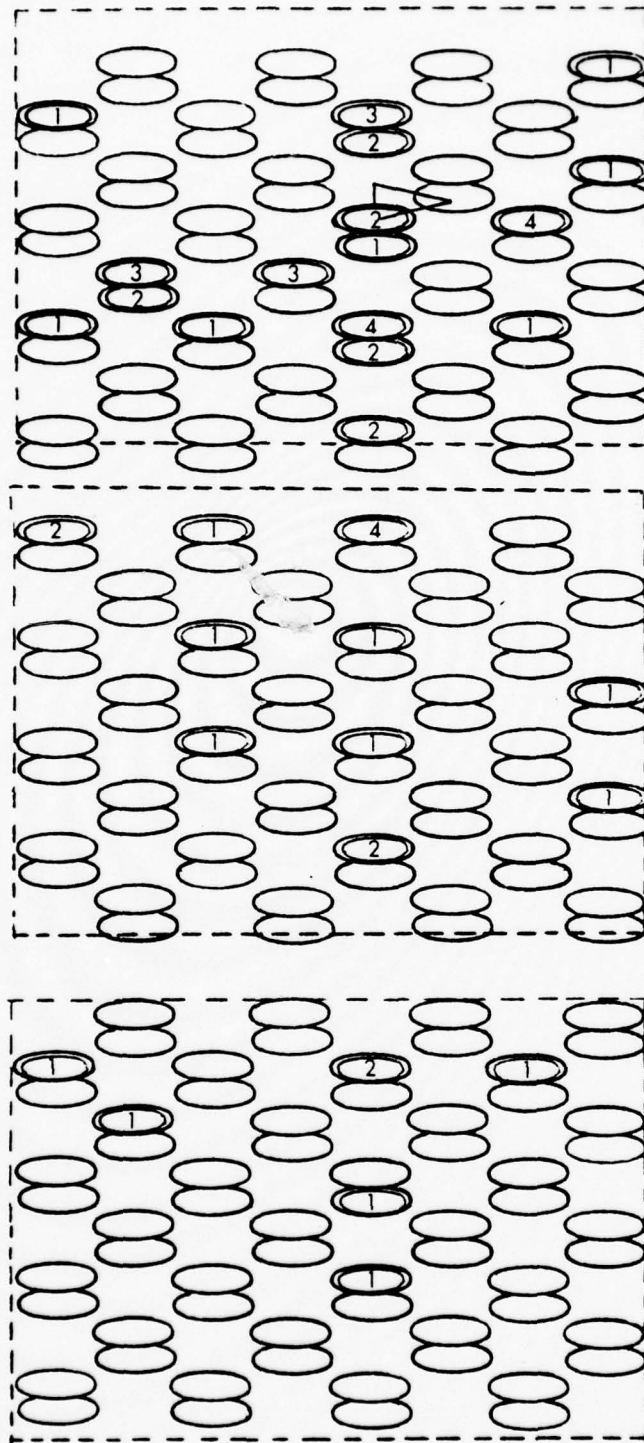


Figure 37 - (111) Orientation, 1-keV Sputtering Events

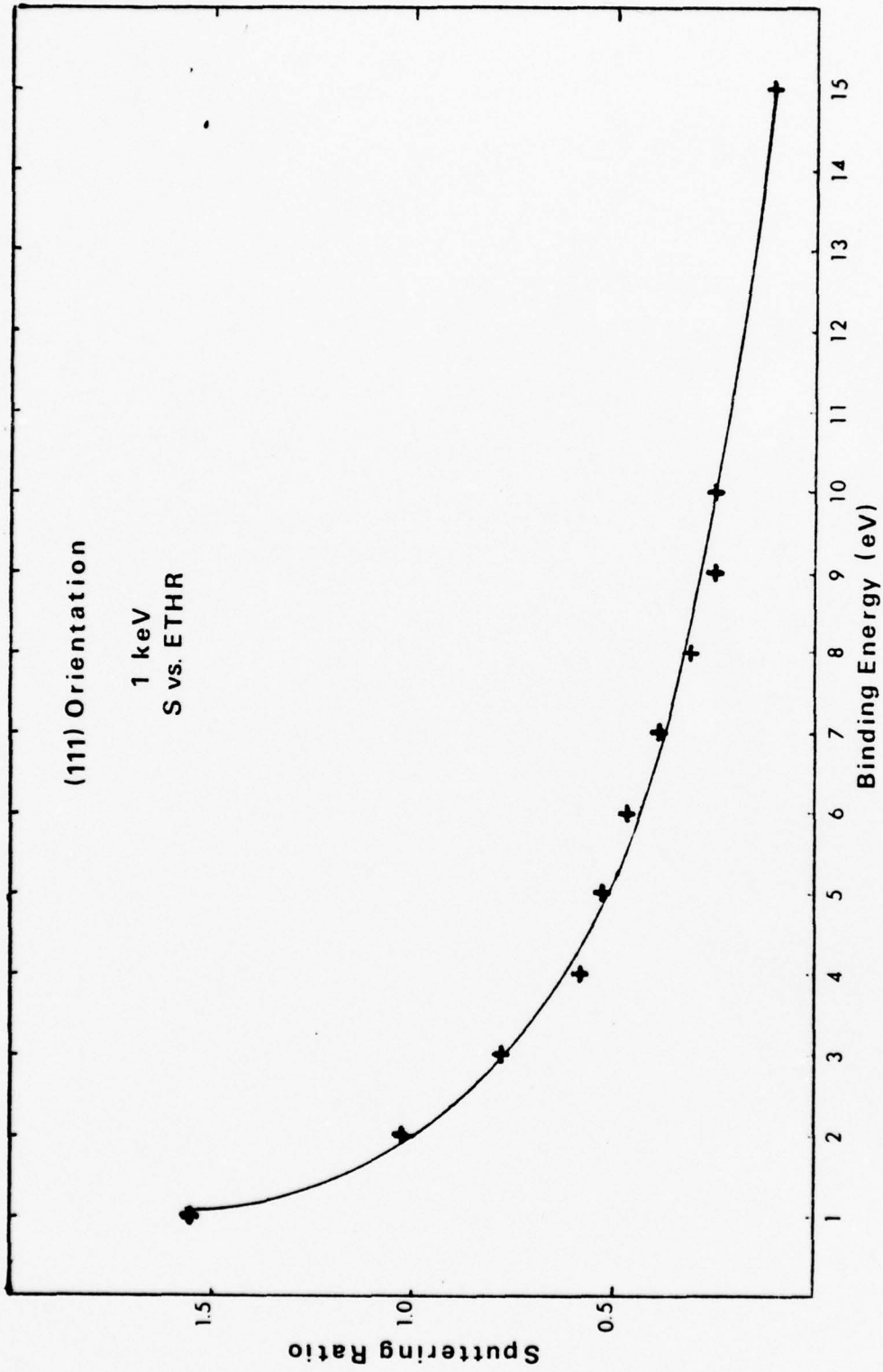


Figure 38

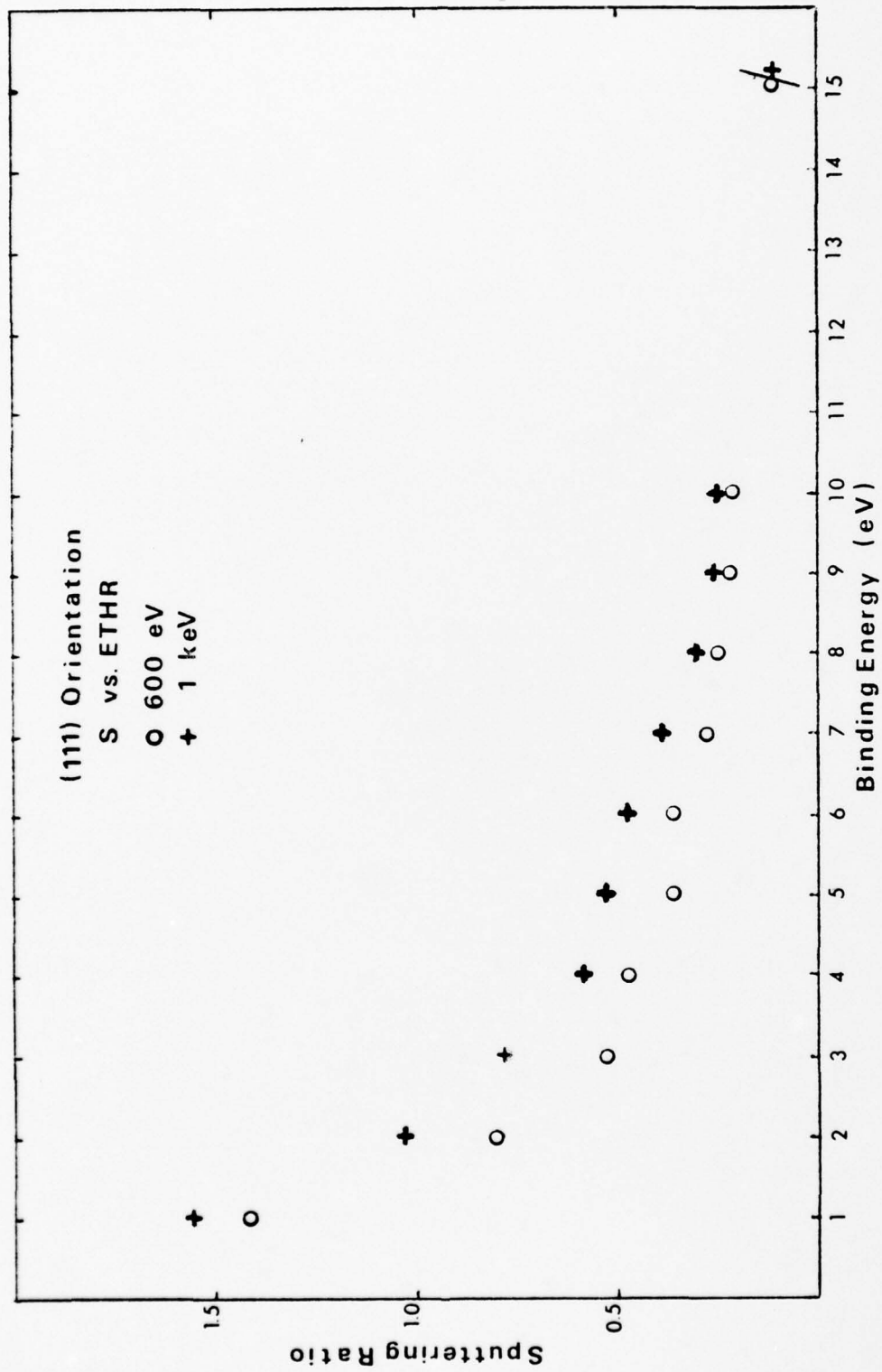


Figure 39

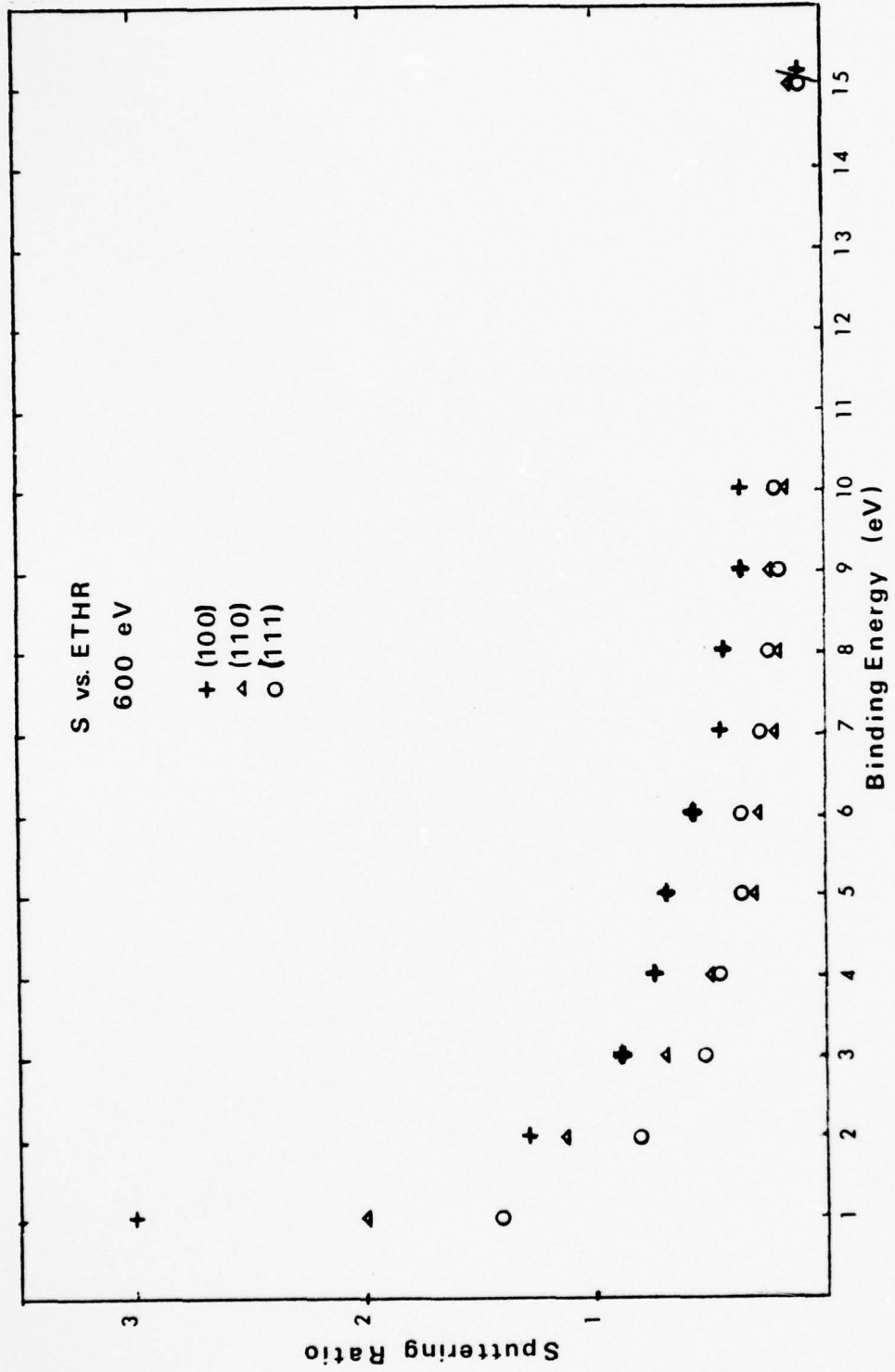


Figure 40

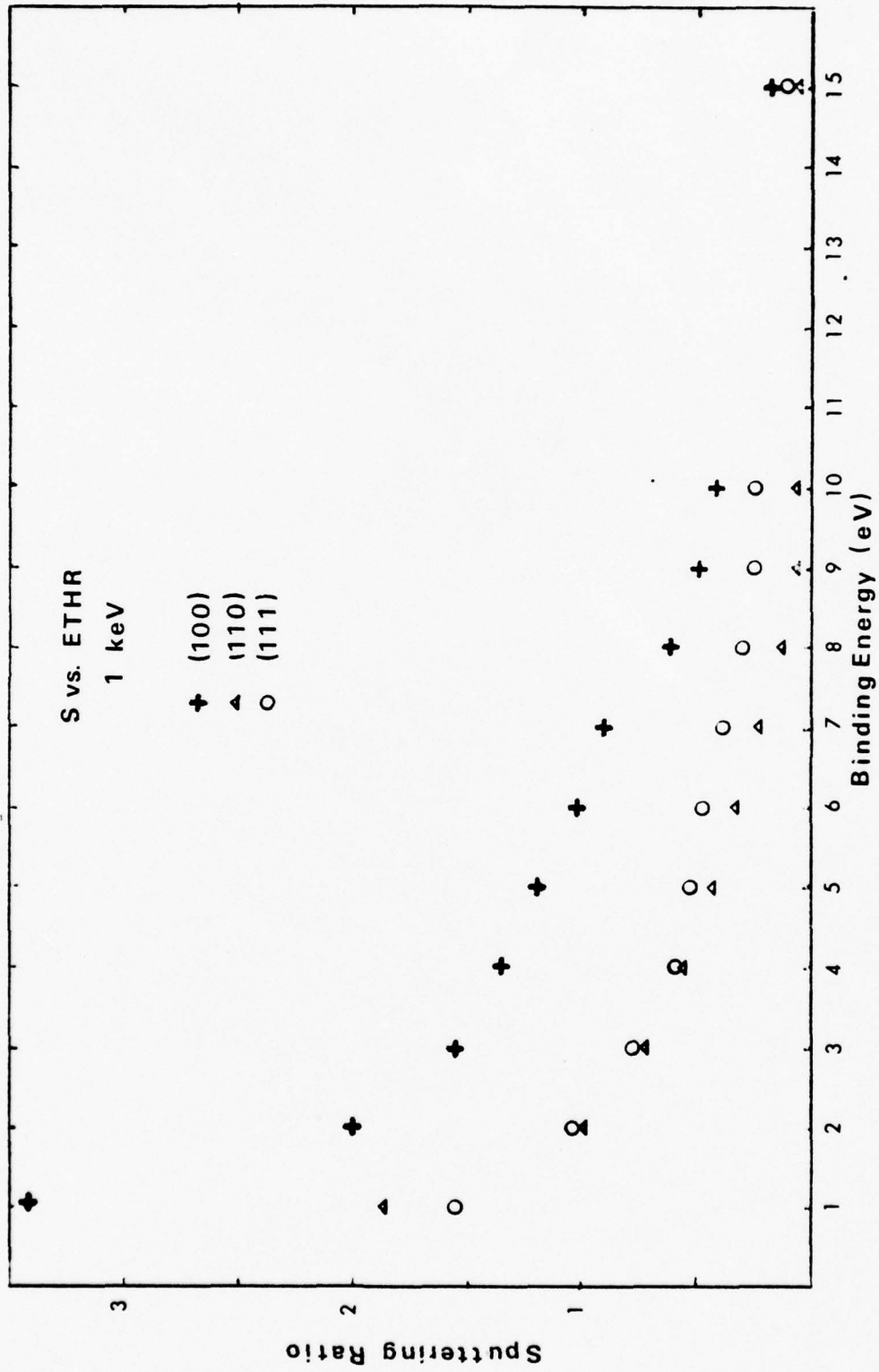


Figure 41

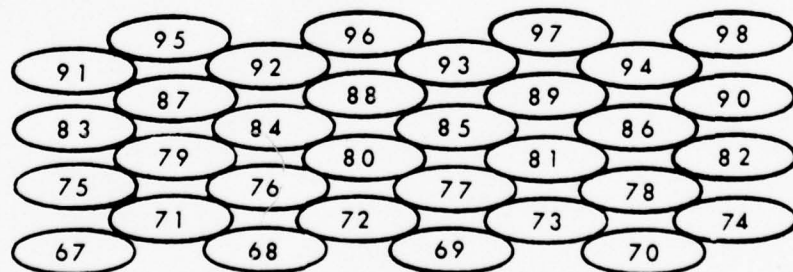
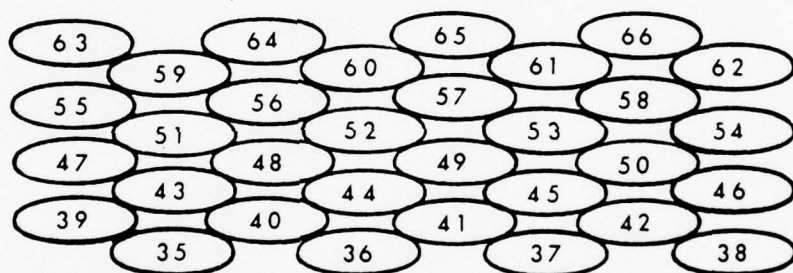
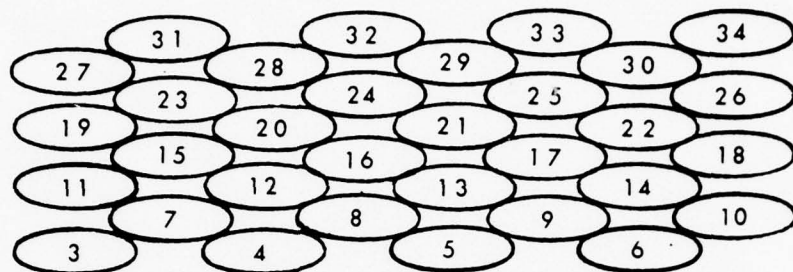


Figure 42 - Copper Single Crystal [(100) Orientation]

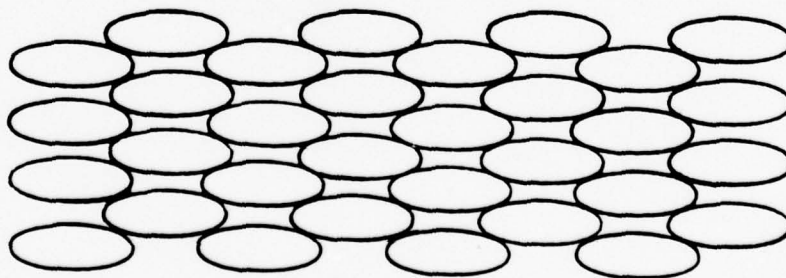
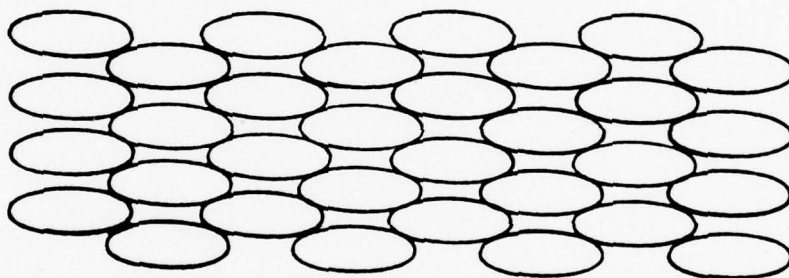
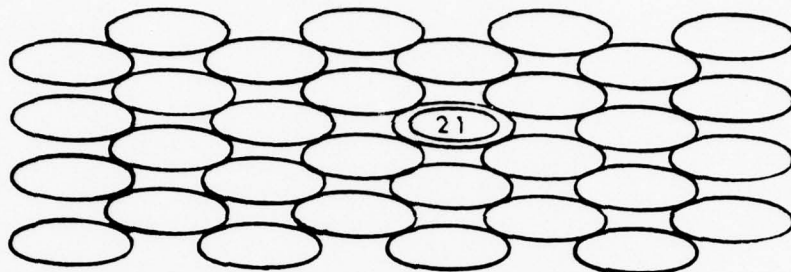


Figure 43 - 600-eV Momentum Spread in Copper (Timestep 1)

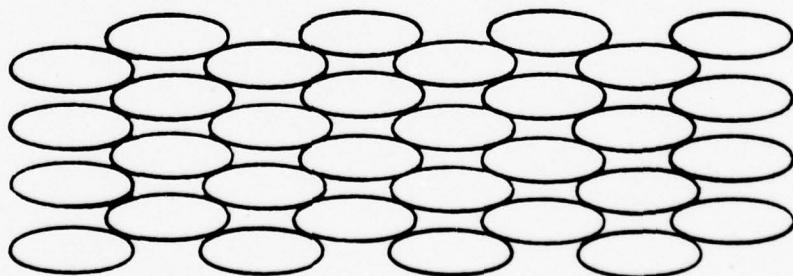
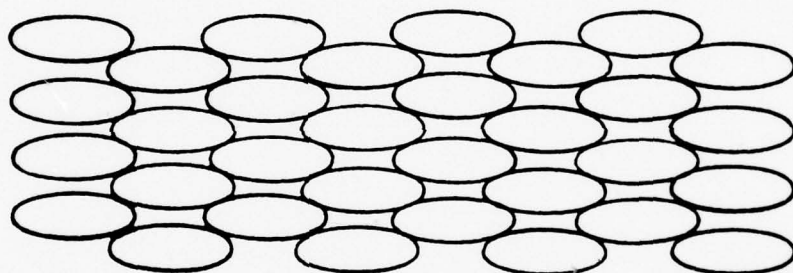
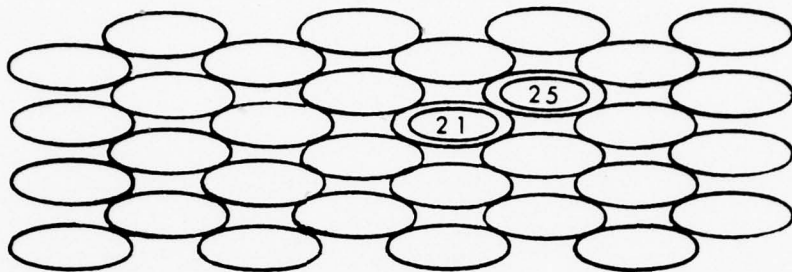


Figure 44 - 600-eV Momentum Spread in Copper (Timestep 5)

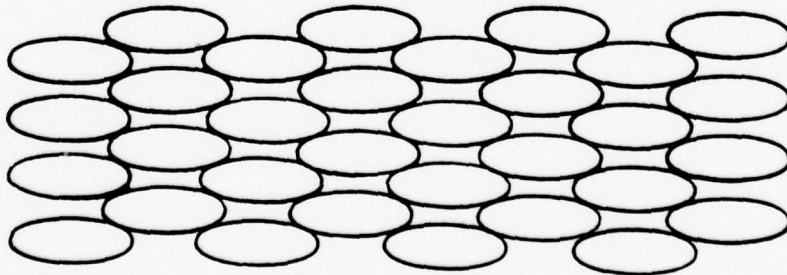
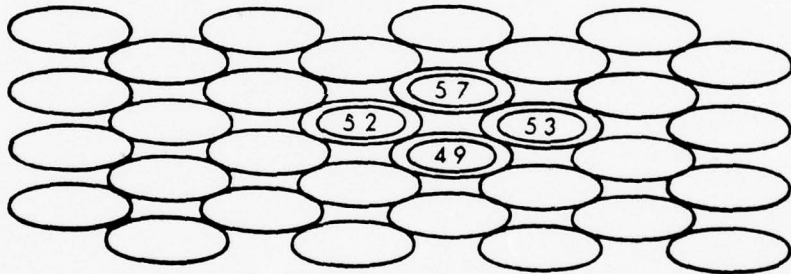
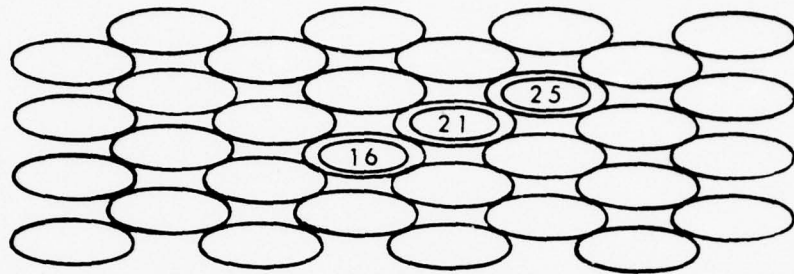


Figure 45 - 600-eV Momentum Spread in Copper (Timestep 15)

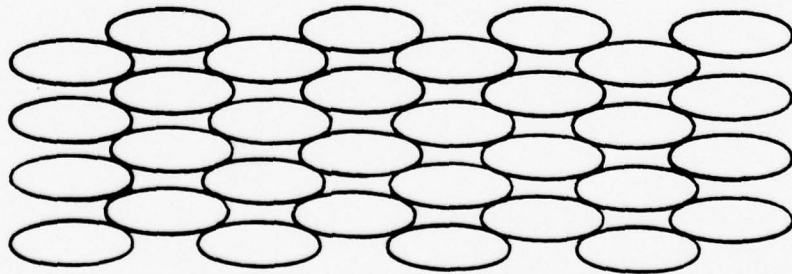
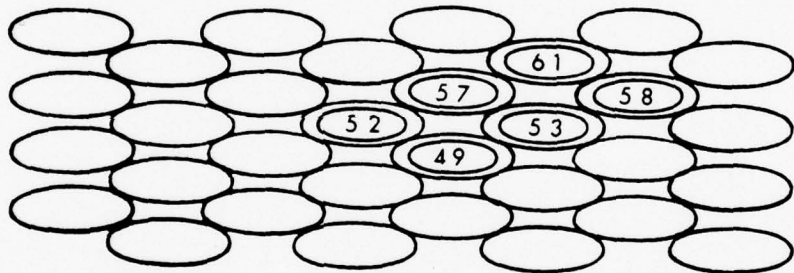
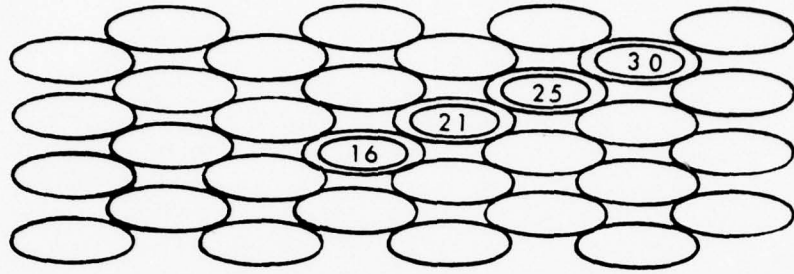


Figure 46 - 600-eV Momentum Spread in Copper (Timestep 20)

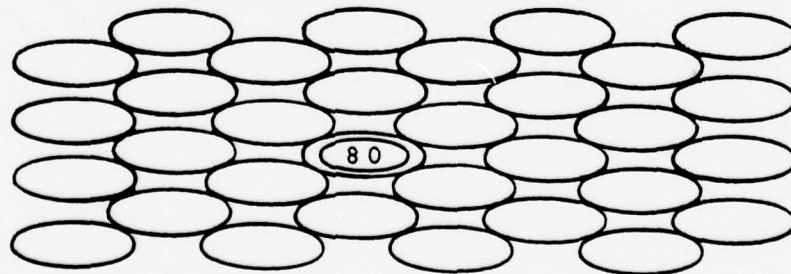
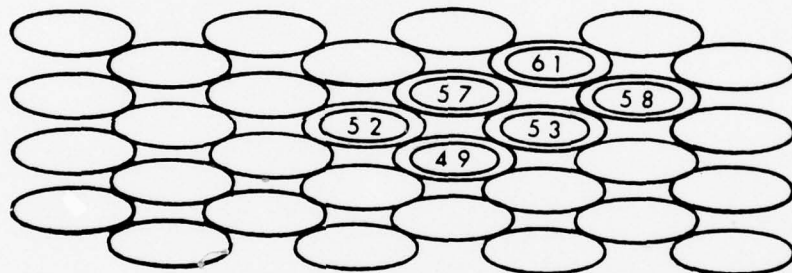
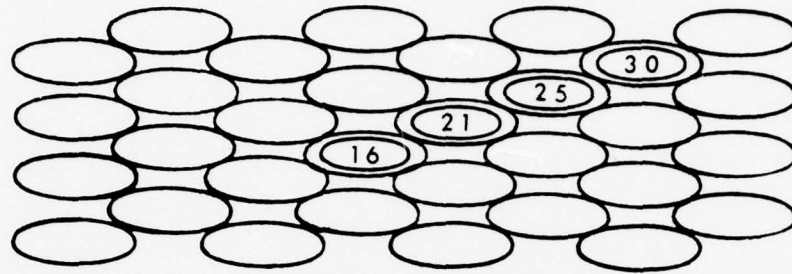


Figure 47 - 600-eV Momentum Spread in Copper (Timestep 25)

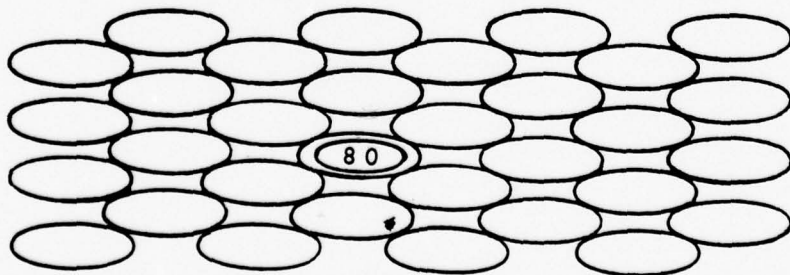
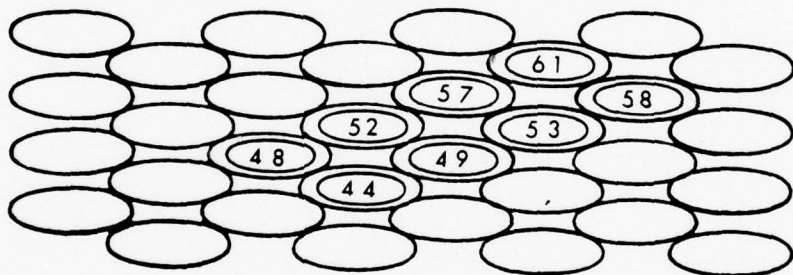
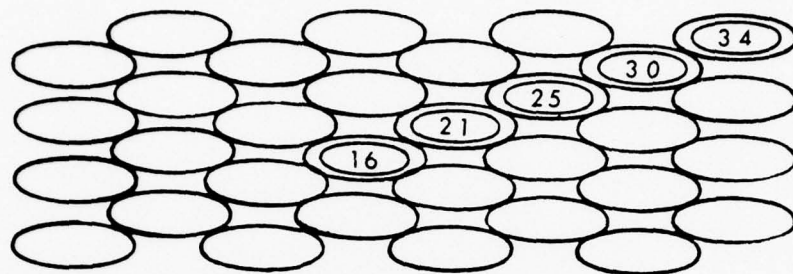


Figure 48 - 600-eV Momentum Spread in Copper (Timestep 27)

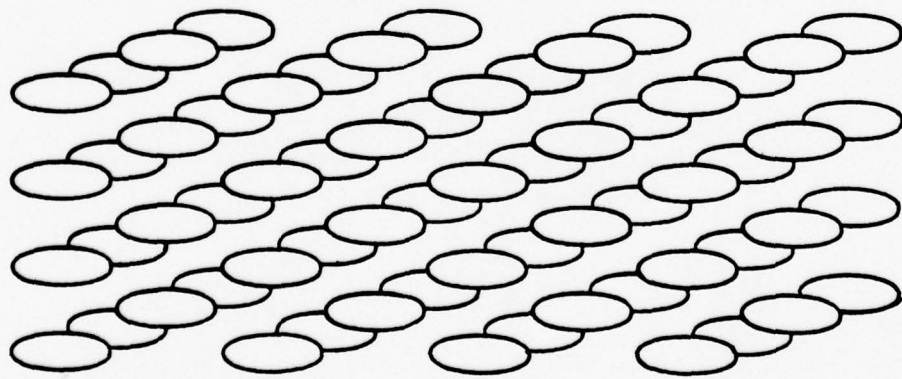
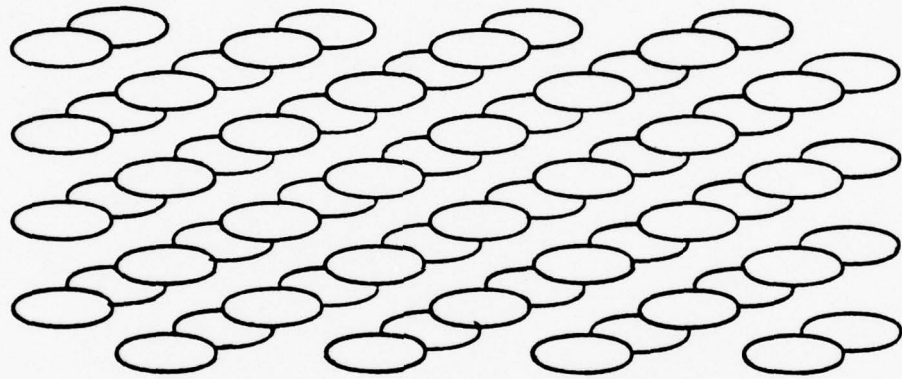
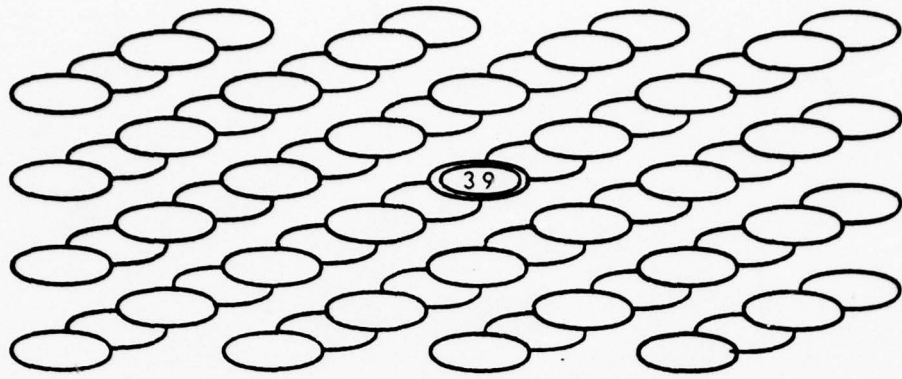


Figure 49 - 600-eV Momentum Spread in Silicon (Timestep 1)

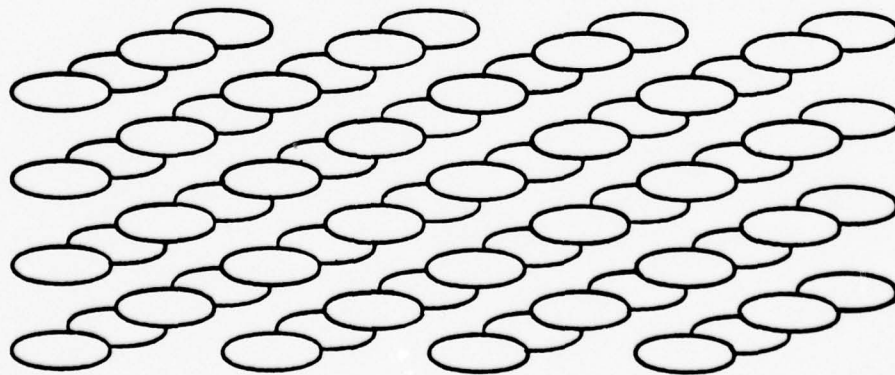
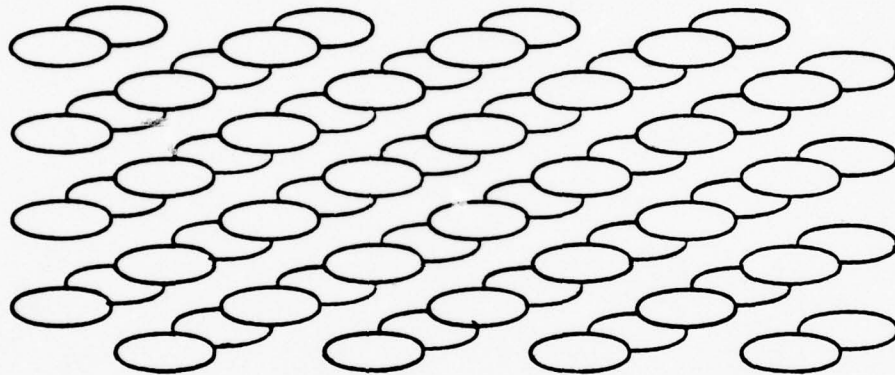
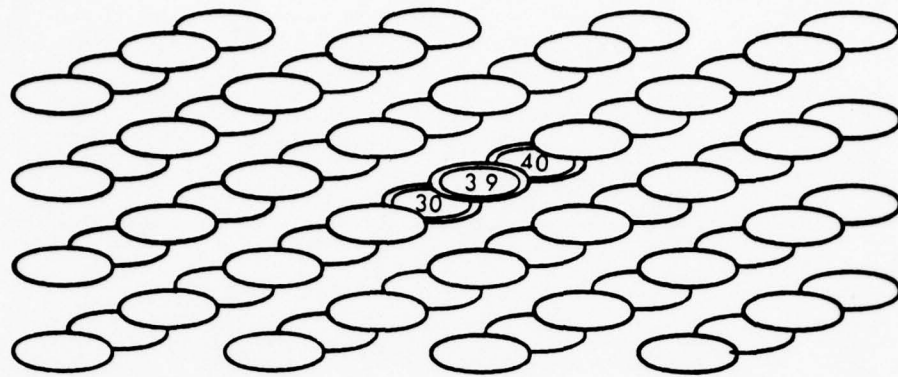


Figure 50 - 600-eV Momentum Spread in Silicon
(Timestep 10)

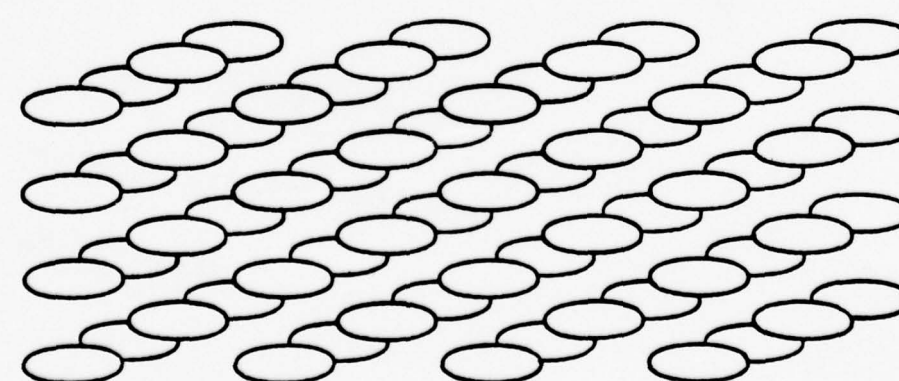
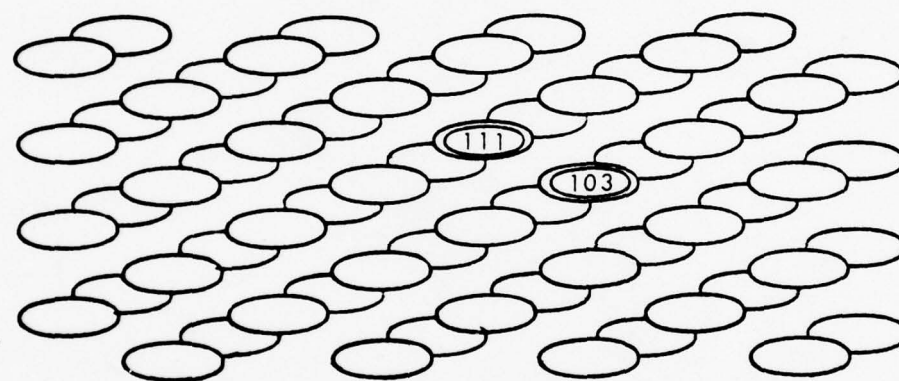
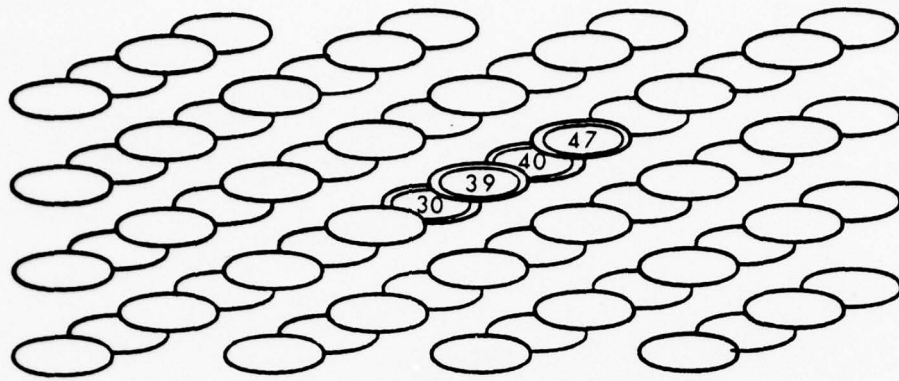


Figure 51 - 600-eV Momentum Spread in Silicon
(Timestep 20)

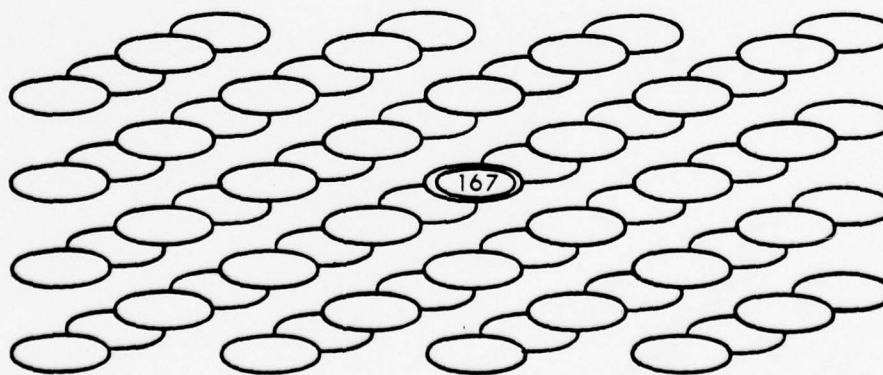
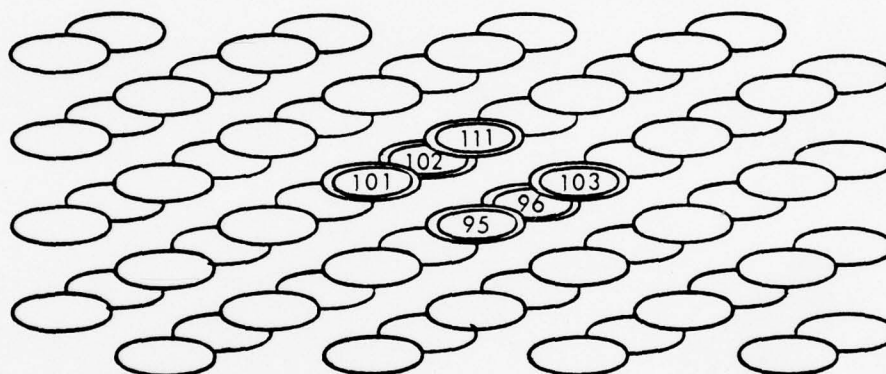
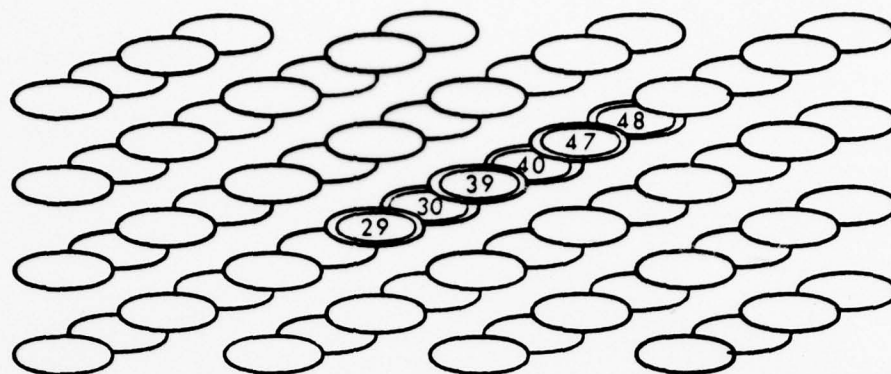


Figure 52 - 600-eV Momentum Spread in Silicon
(Timestep 30)

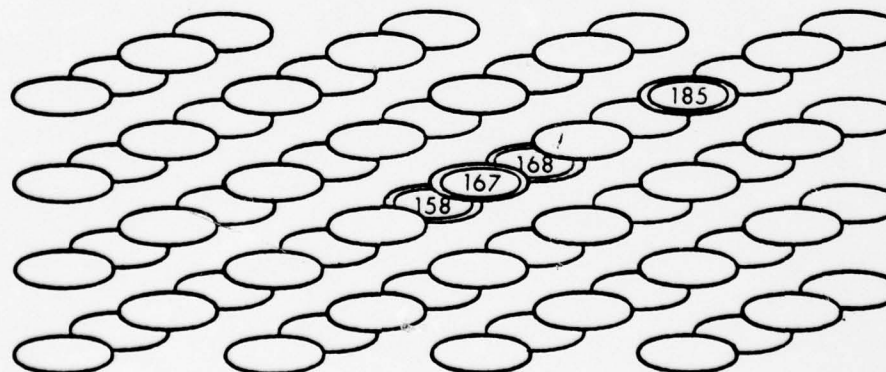
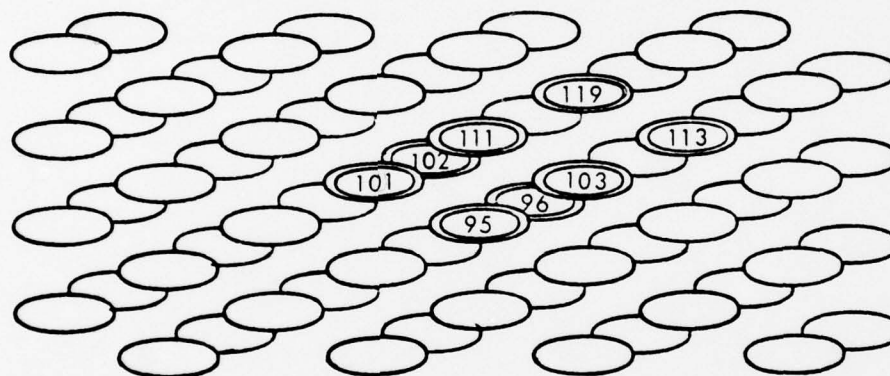
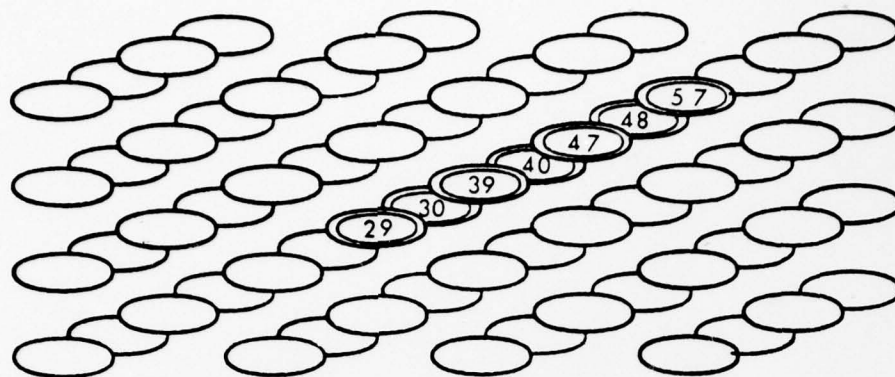


Figure 53 - 600-eV Momentum Spread in Silicon
(Timestep 40)

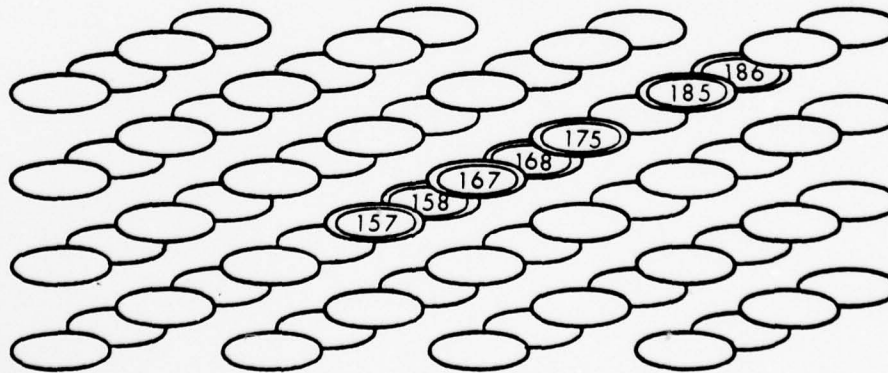
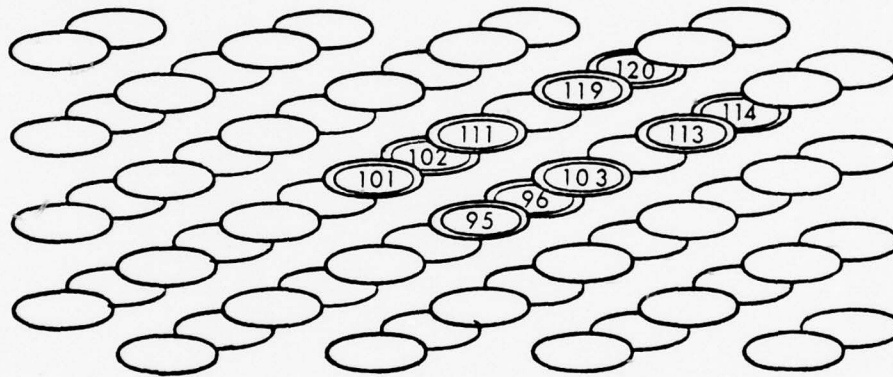
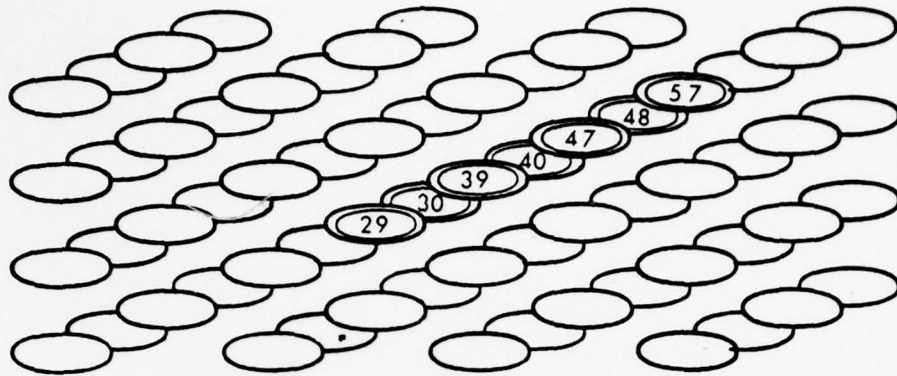


Figure 54 - 600-eV Momentum Spread in Silicon
(Timestep 50)

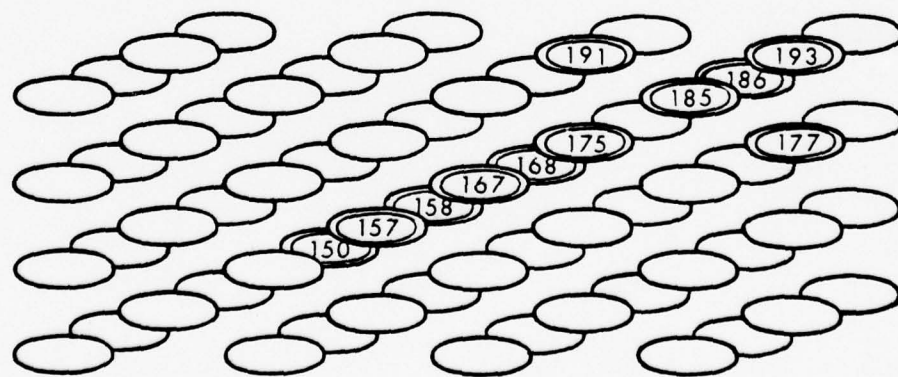
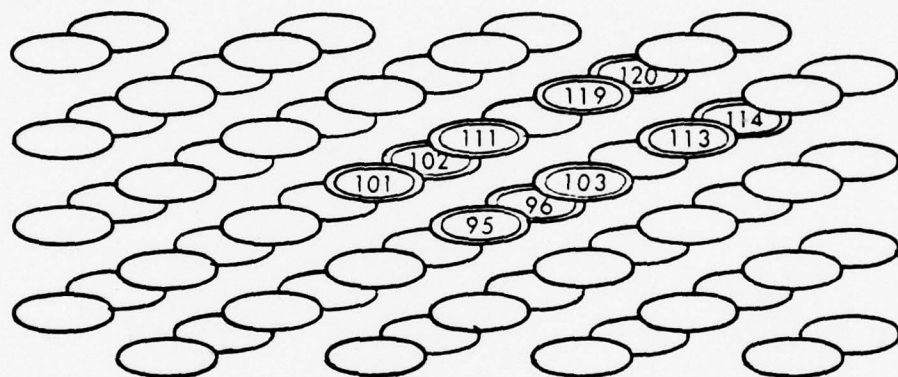
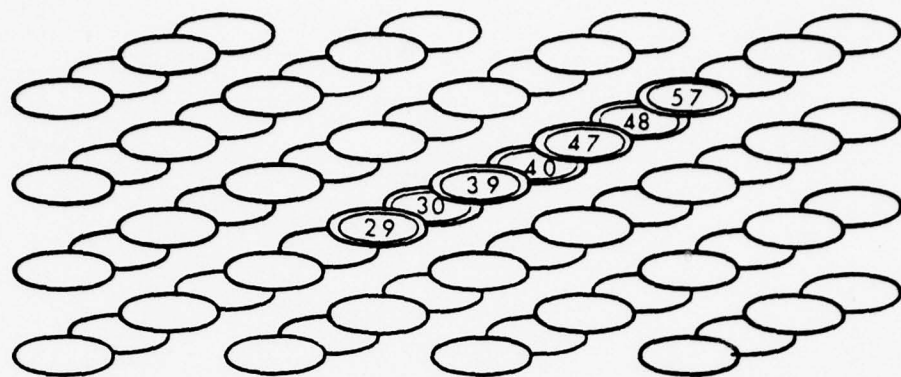


Figure 55 - 600-eV Momentum Spread in Silicon
(Timestep 60)

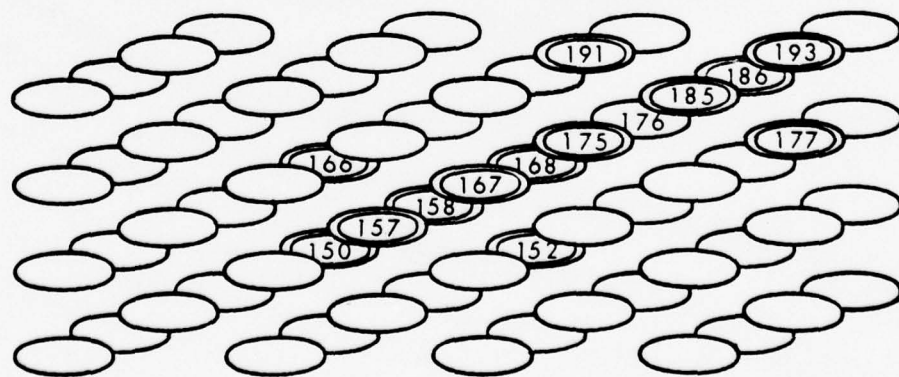
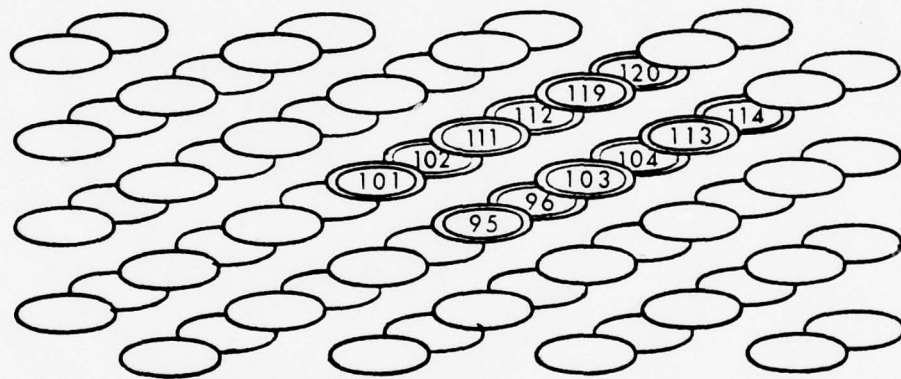
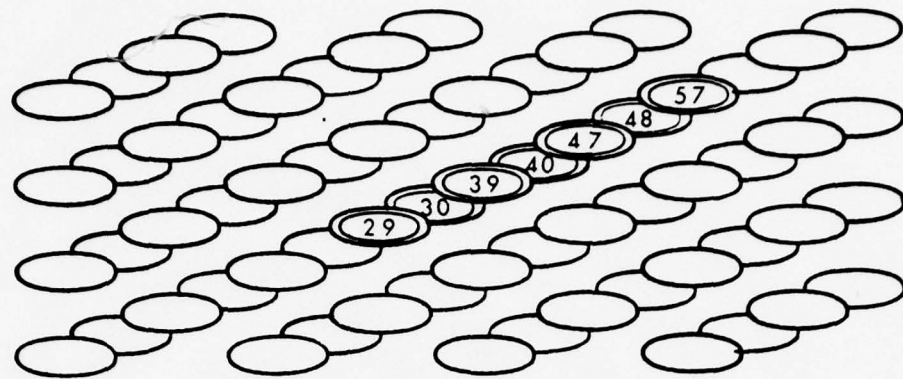


Figure 56 - 600-eV Momentum Spread in Silicon
(Timestep 70)

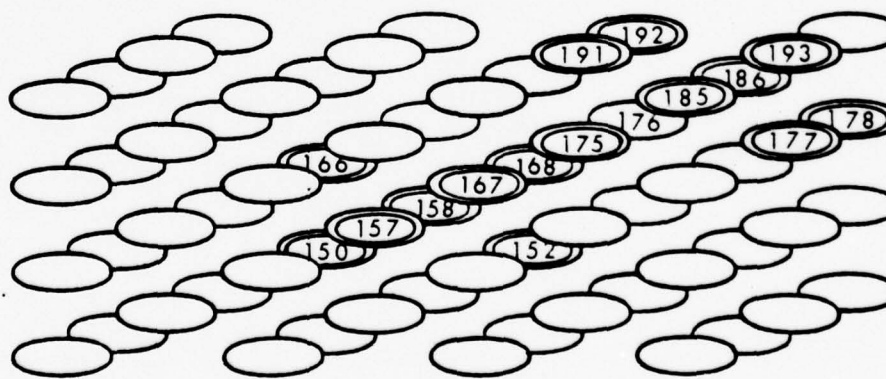
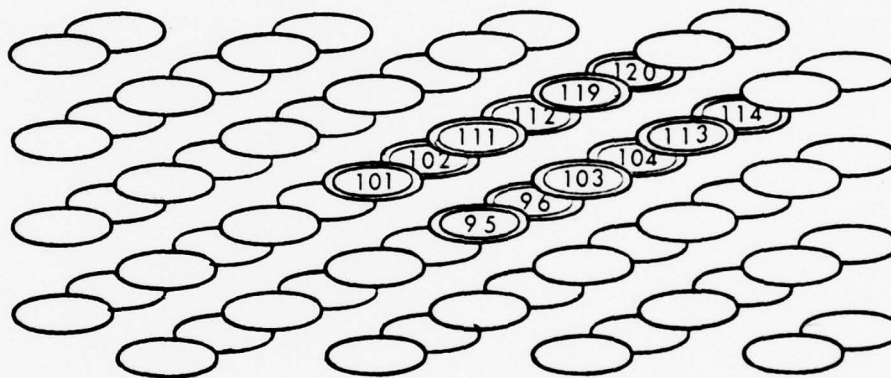
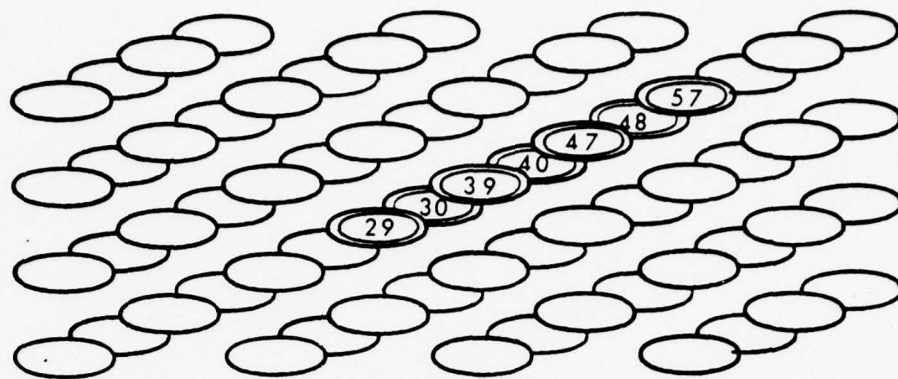


Figure 57 - 600-eV Momentum Spread in Silicon
(Timestep 72)

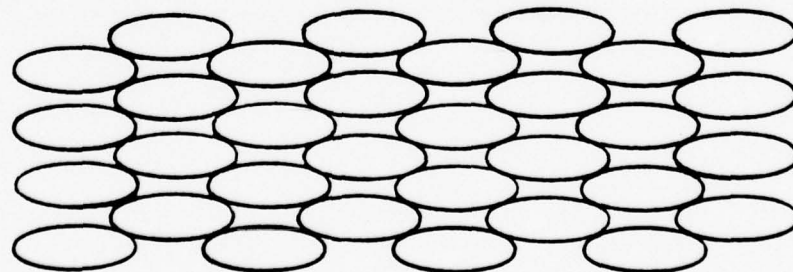
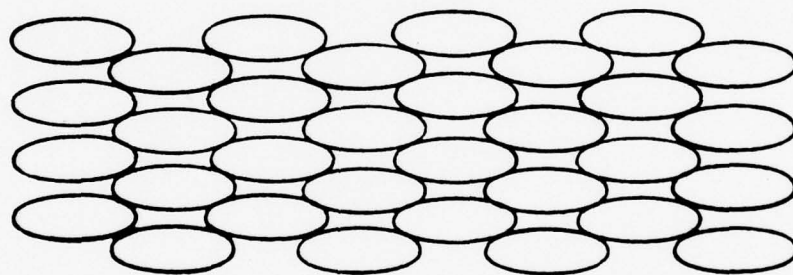
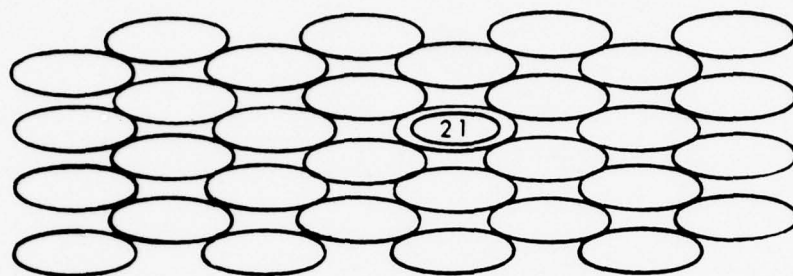


Figure 58 - 1-keV Momentum Spread in Copper (Timestep 1)

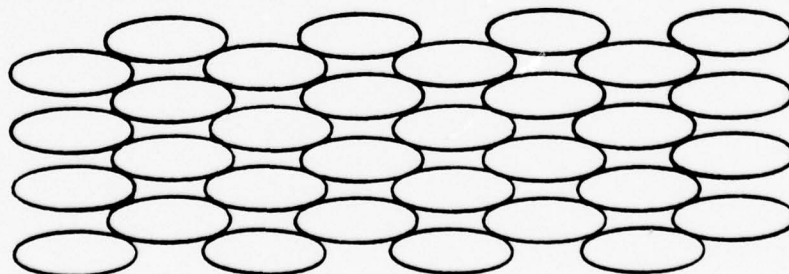
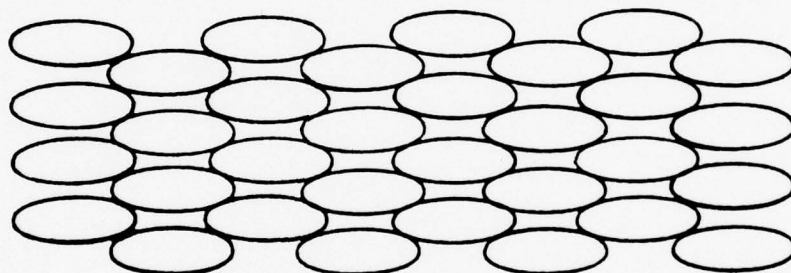
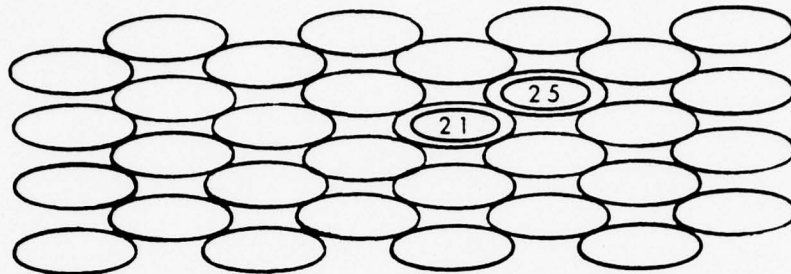


Figure 59 - 1-keV Momentum Spread in Copper (Timestep 5)

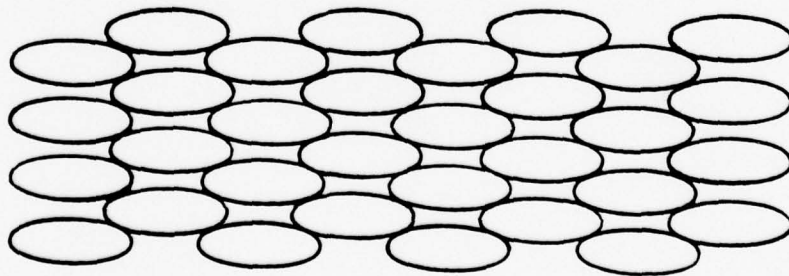
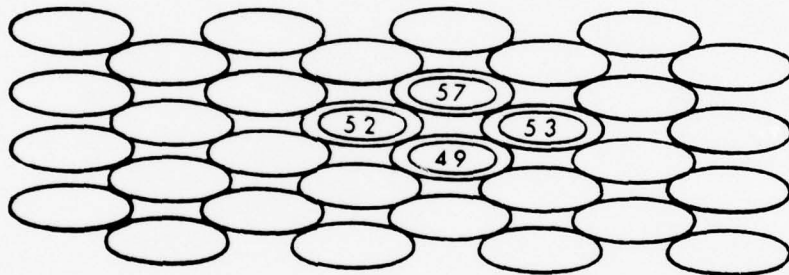
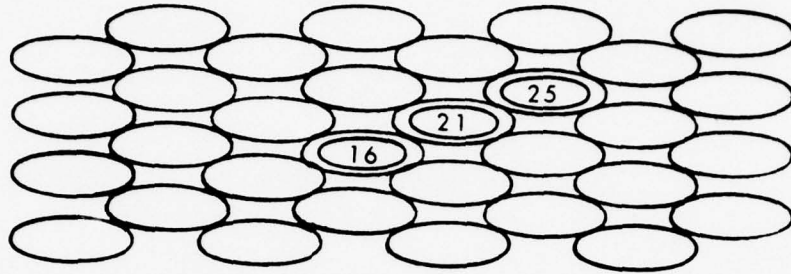


Figure 60 - 1-keV Momentum Spread in Copper (Timestep 15)

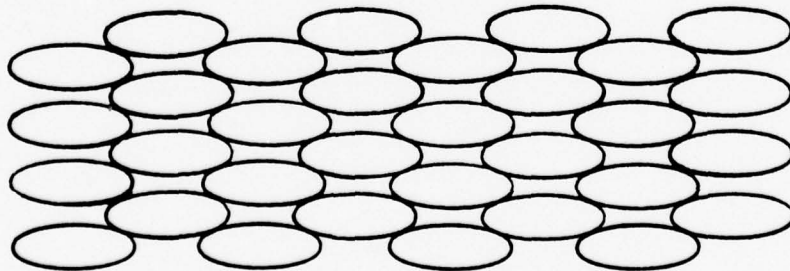
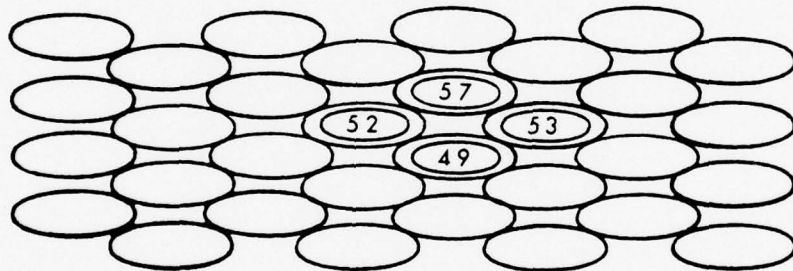
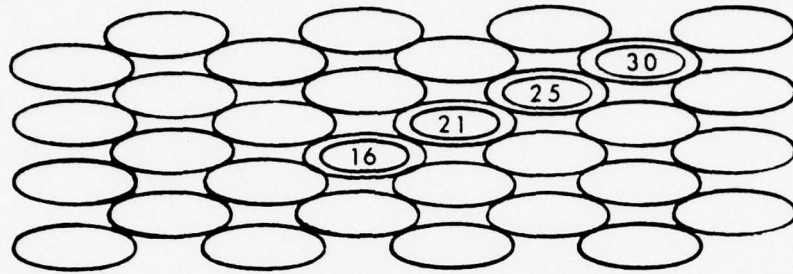


Figure 61 - 1-keV Momentum Spread in Copper (Timestep 20)

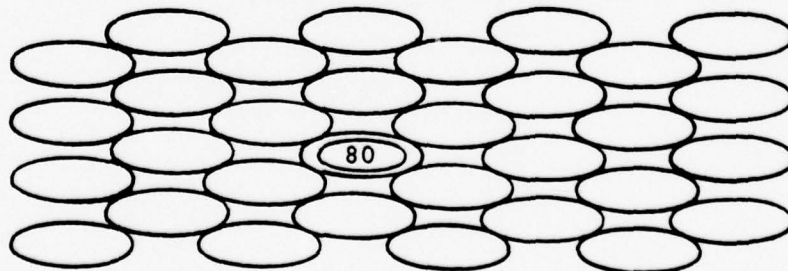
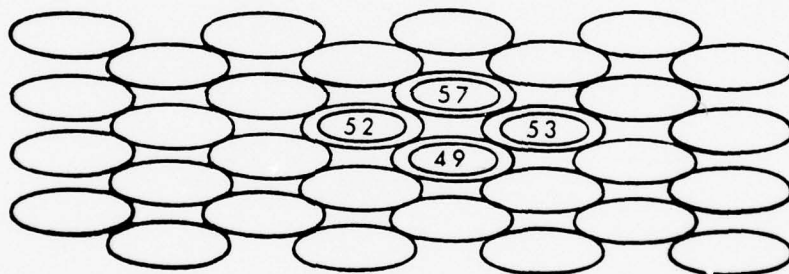
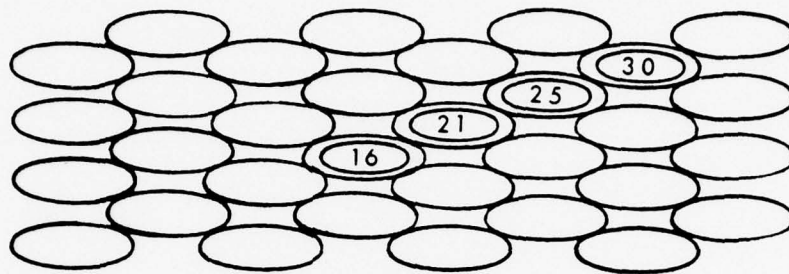


Figure 62 - 1-keV Momentum Spread in Copper (Timestep 26)

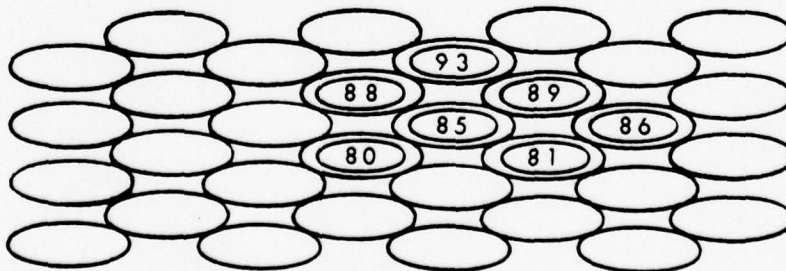
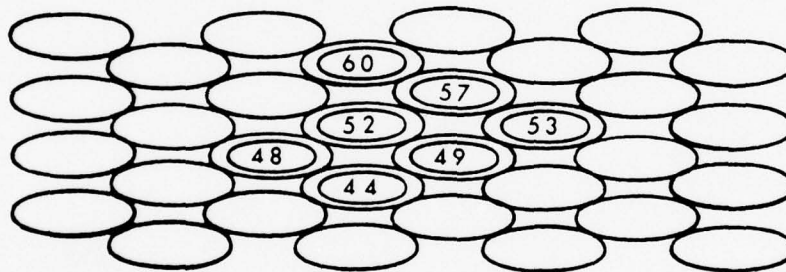
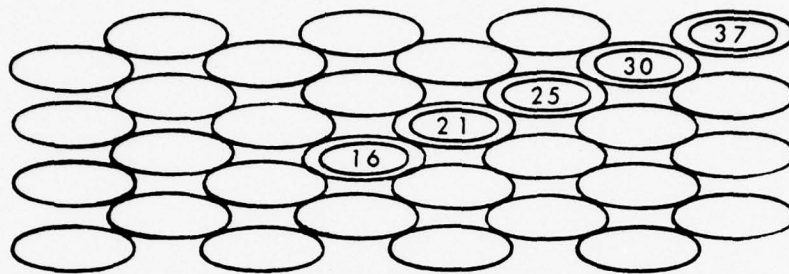


Figure 63 - 1-keV Momentum Spread in Copper (Timestep 29)

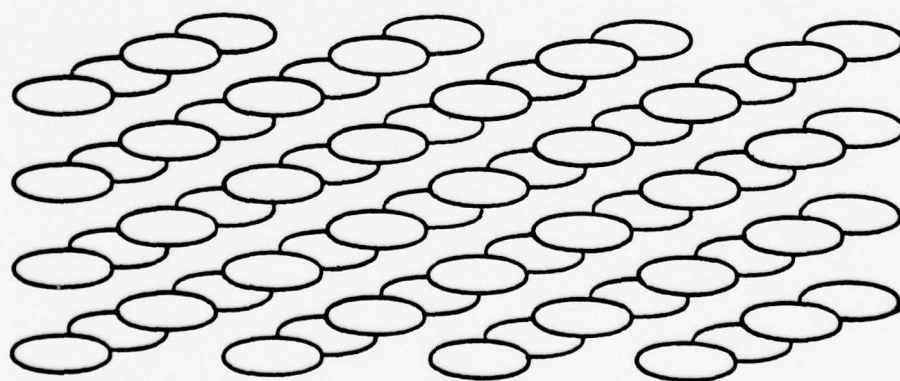
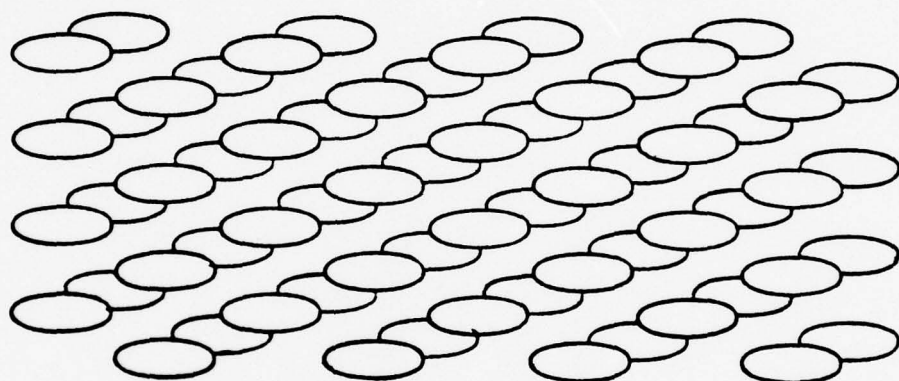
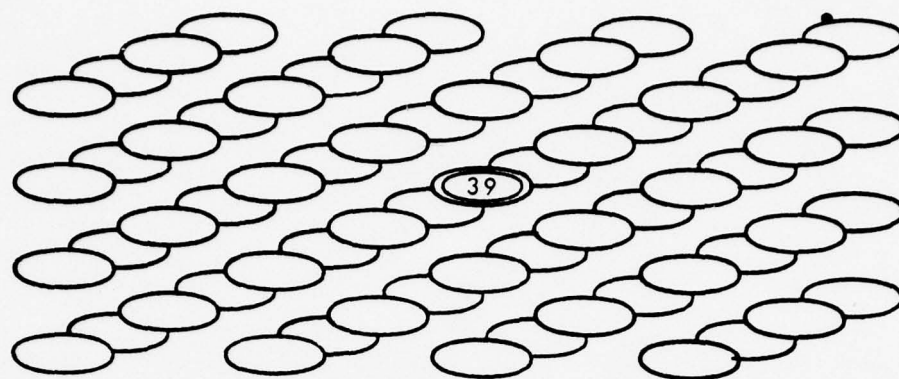


Figure 64 - 1-keV Momentum Spread in Silicon (Timestep 1)

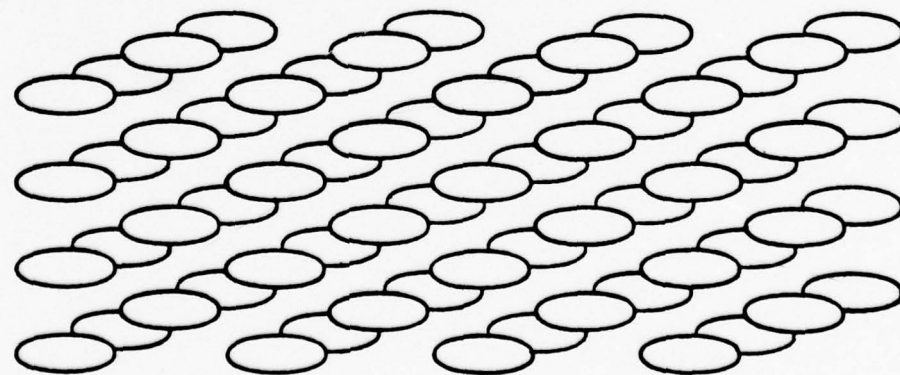
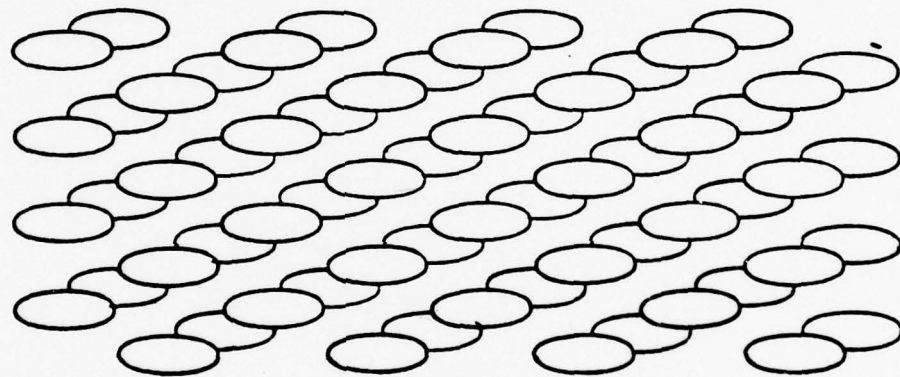
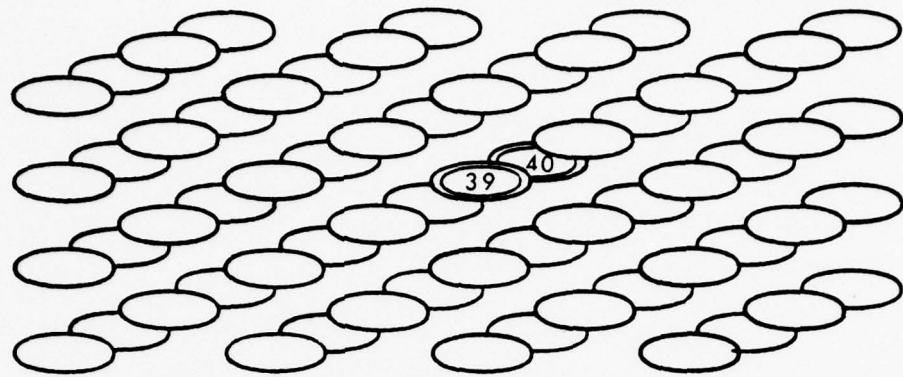


Figure 65 - 1-keV Momentum Spread in Silicon (Timestep 10)

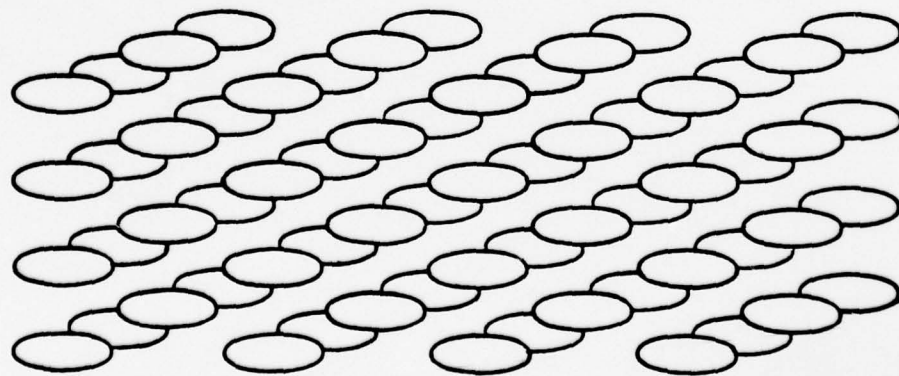
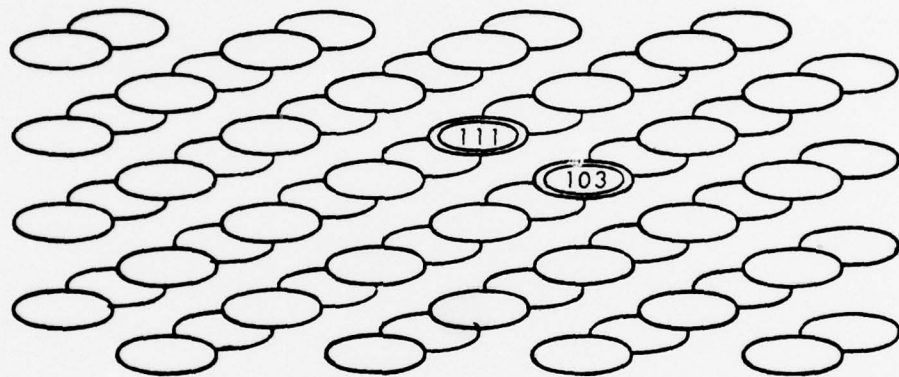
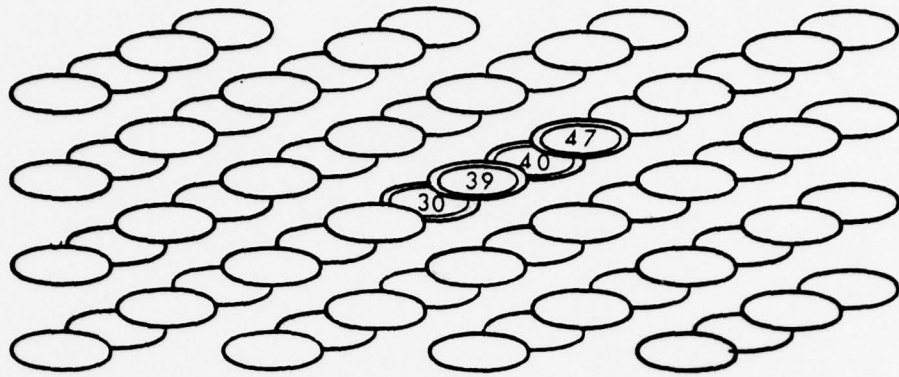


Figure 66 - 1-keV Momentum Spread in Silicon (Timestep 20)

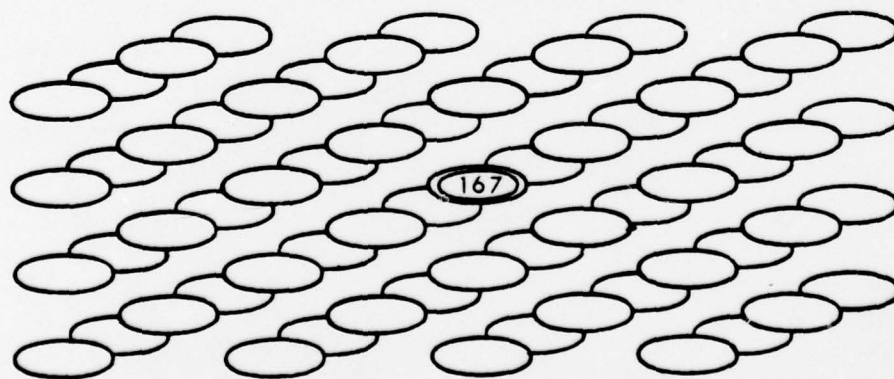
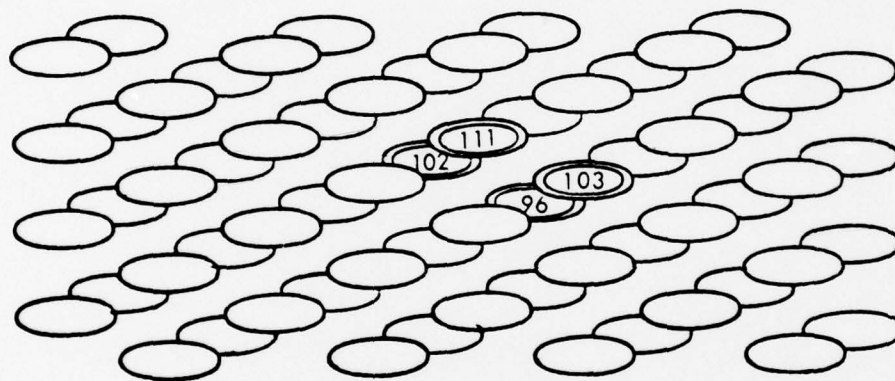
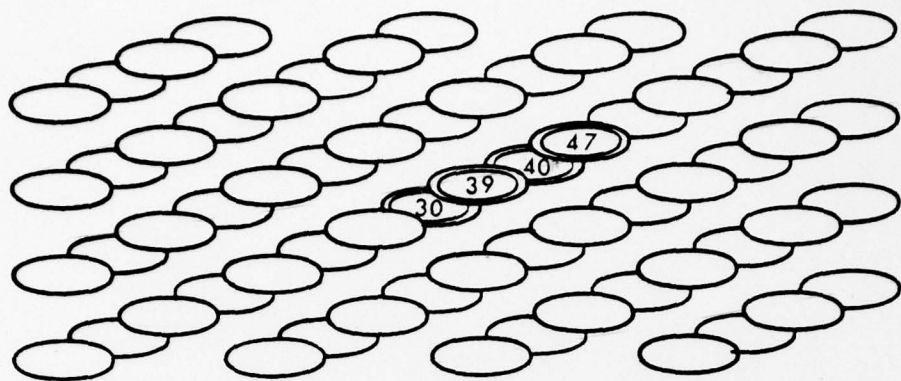


Figure 67 - 1-keV Momentum Spread in Silicon (Timestep 30)

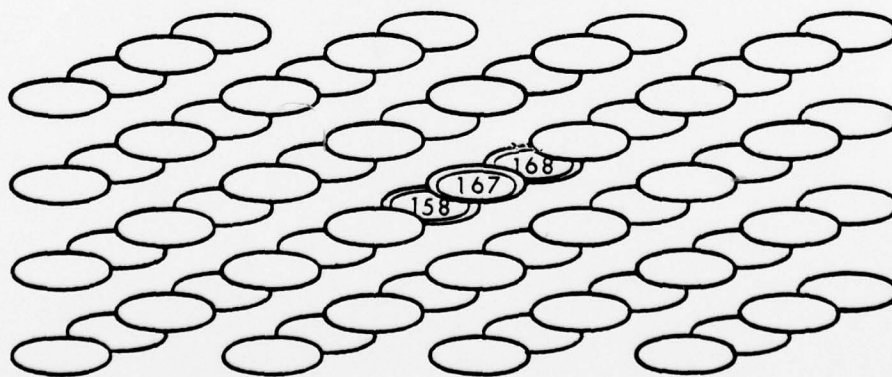
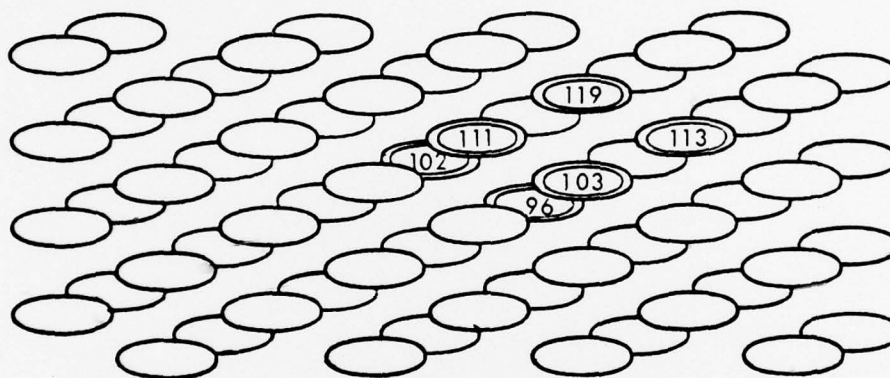
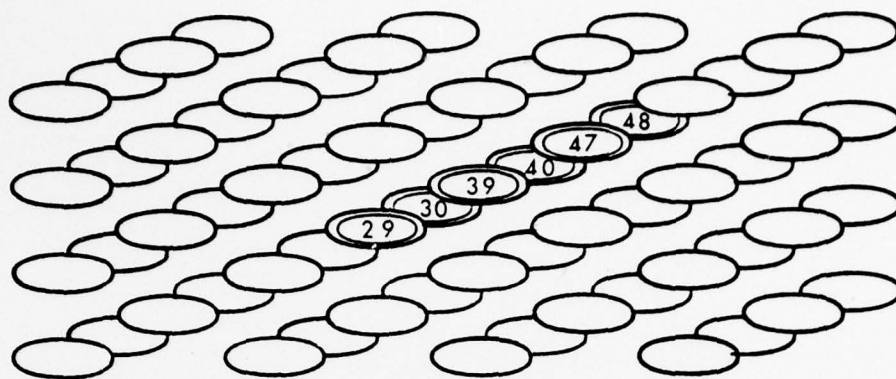


Figure 68 - 1-keV Momentum Spread in Silicon (Timestep 40)

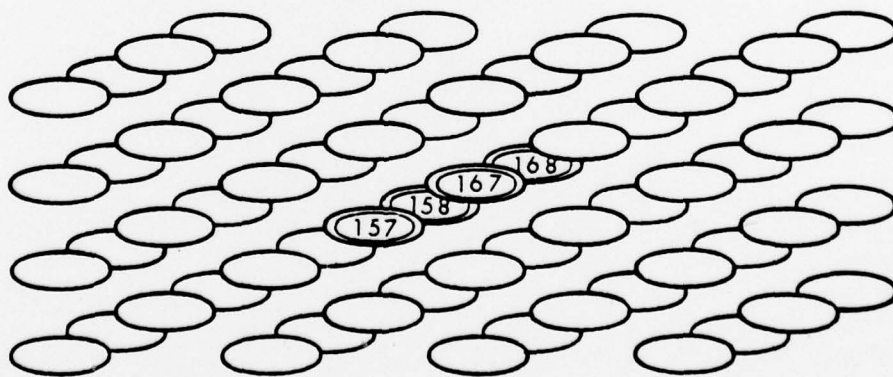
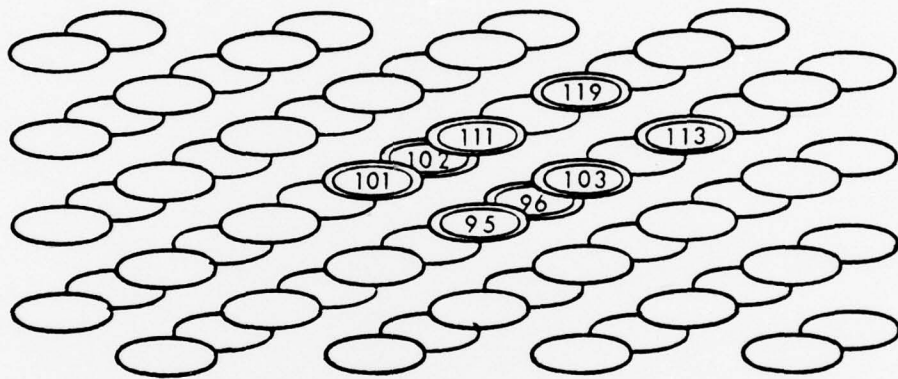
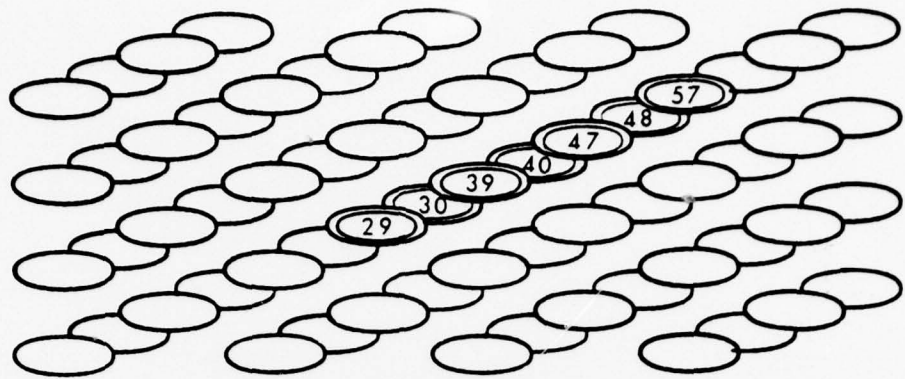


Figure 69 - 1-keV Momentum Spread in Silicon (Timestep 50)

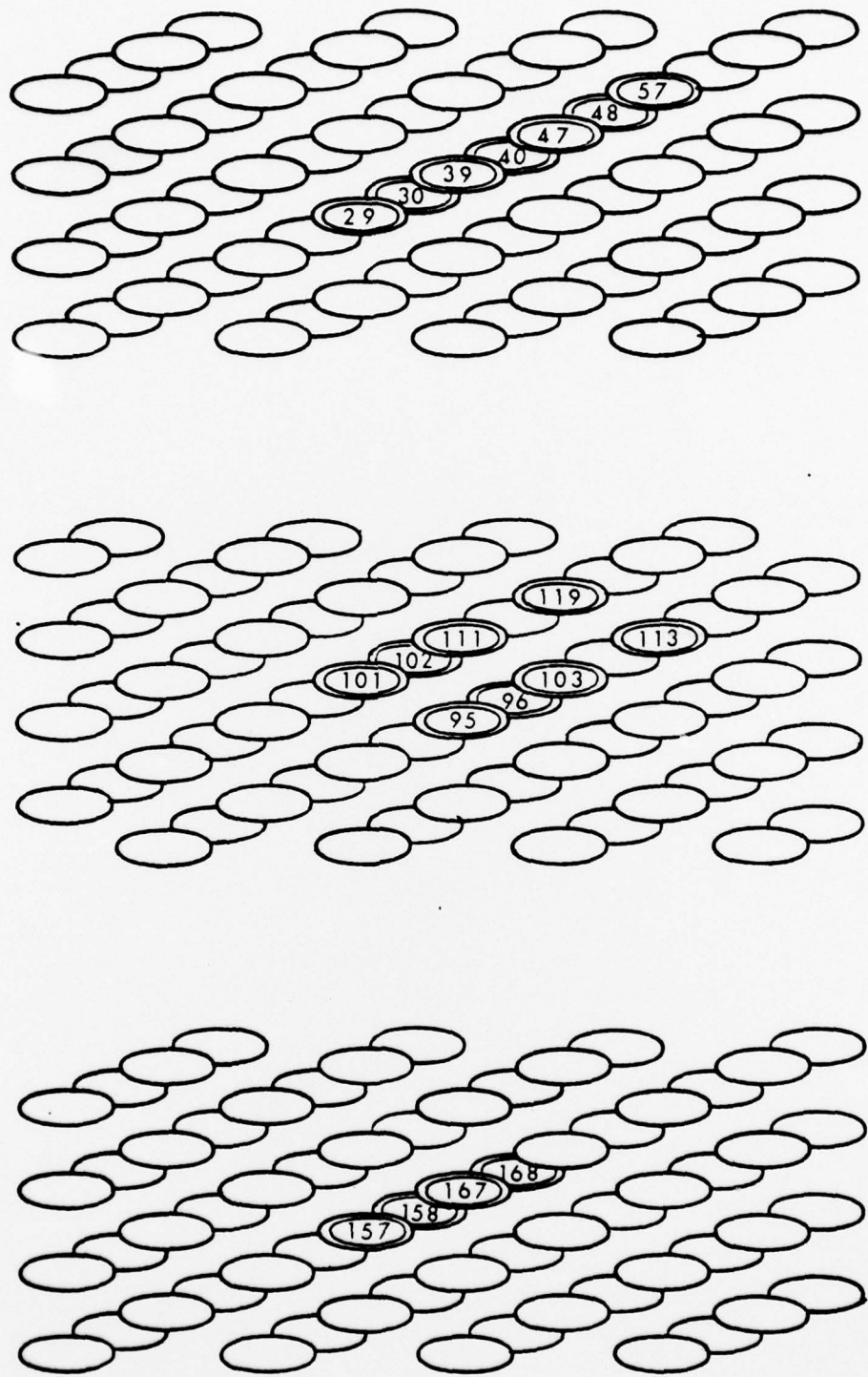


Figure 70 - 1-keV Momentum Spread in Silicon (Timestep 60)

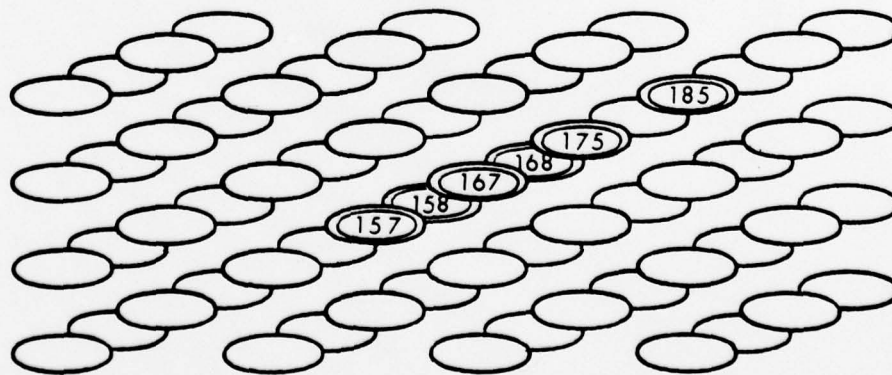
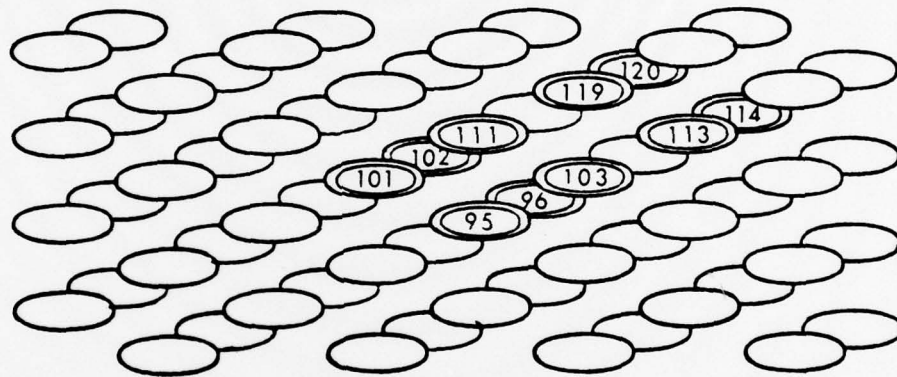
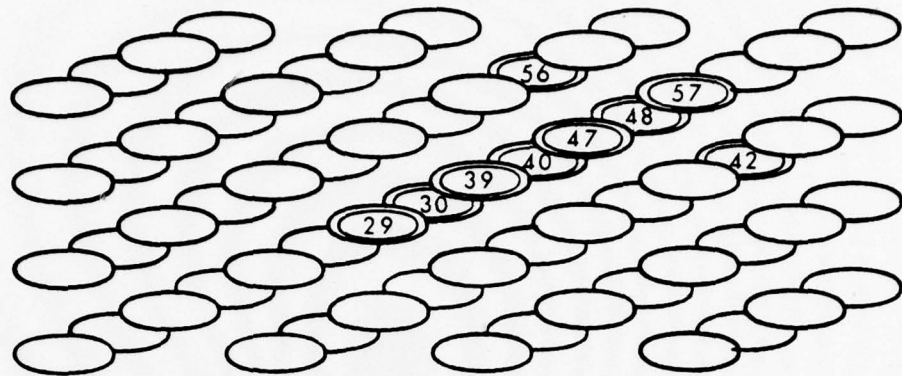


Figure 71 - 1-keV Momentum Spread in Silicon (Timestep 70)

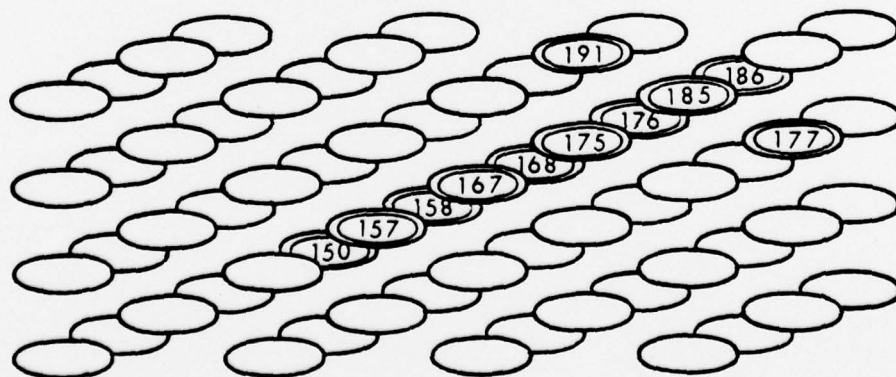
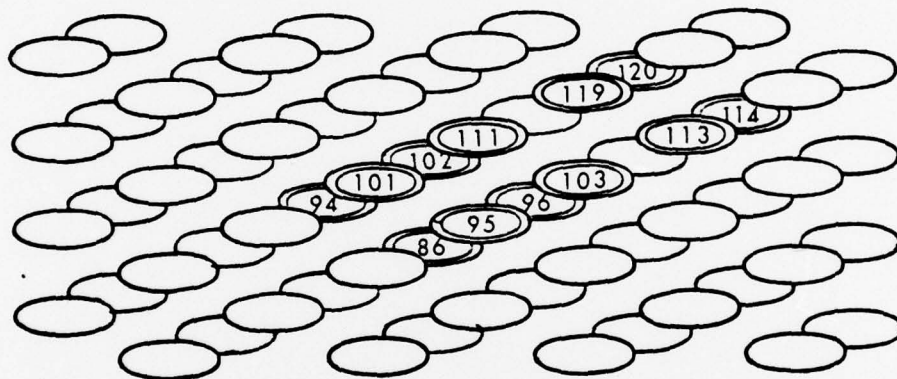
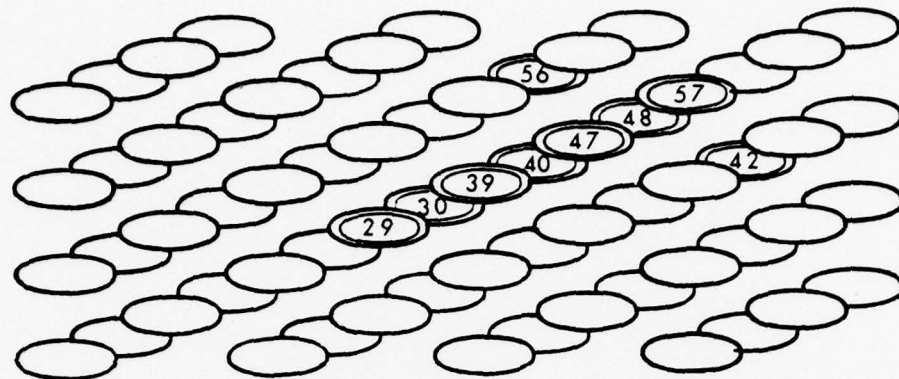


Figure 72 - 1-keV Momentum Spread in Silicon (Timestep 80)

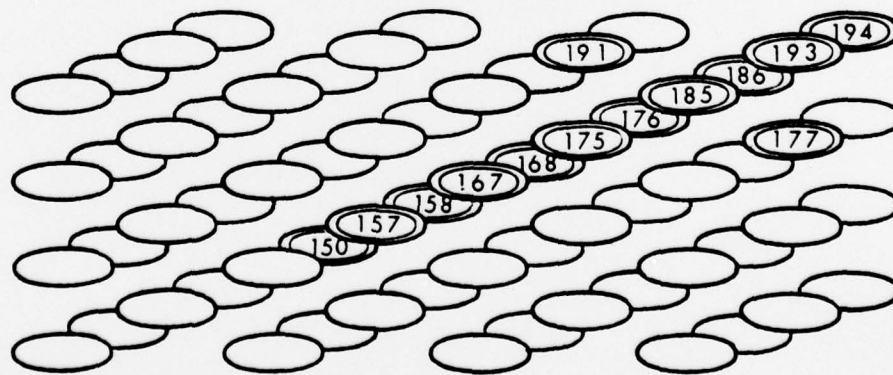
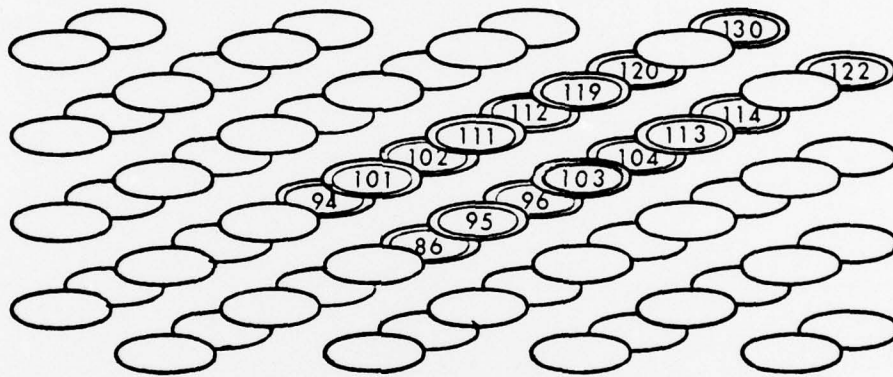
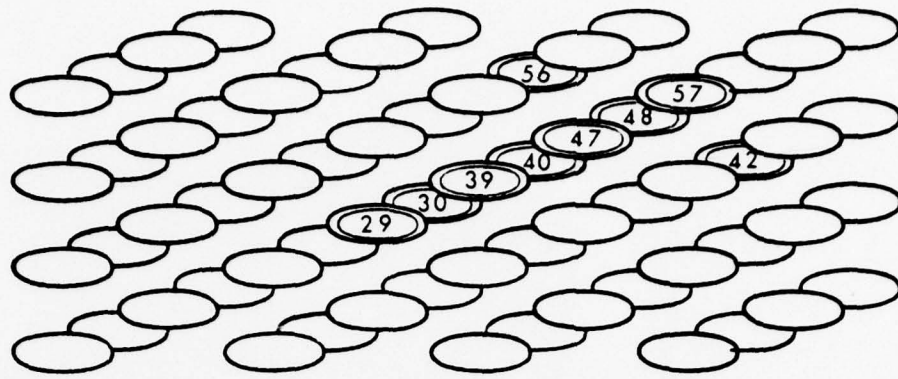
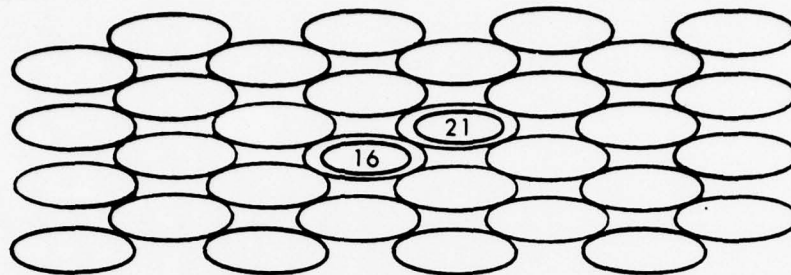
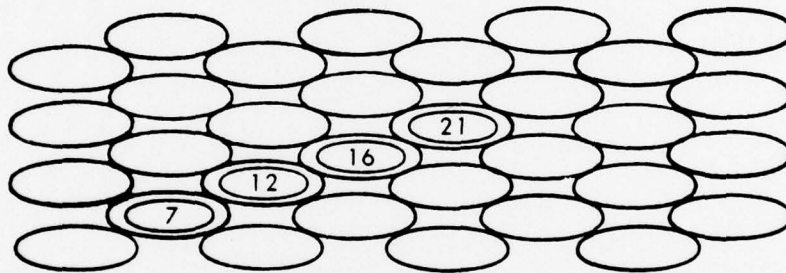


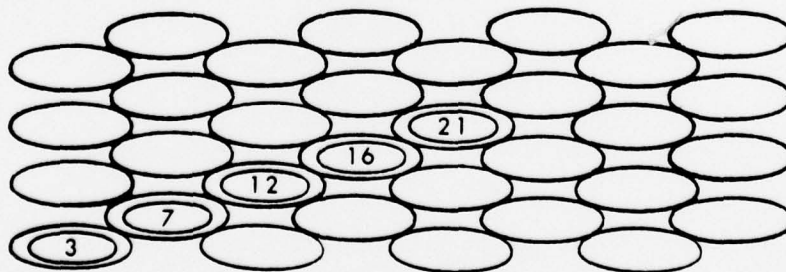
Figure 73 - 1-keV Momentum Spread in Silicon (Timestep 37)



Timestep 1

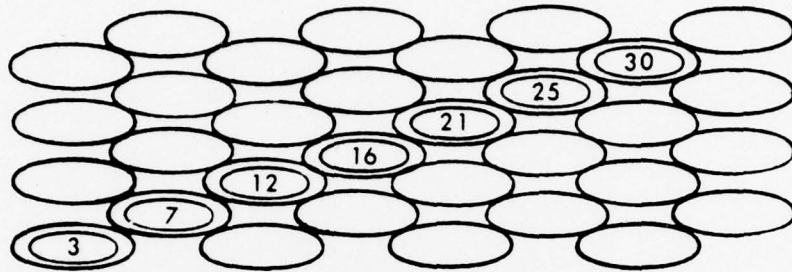


Timestep 2

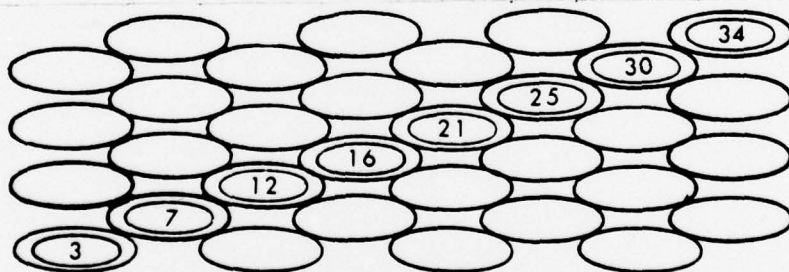


Timestep 3

Figure 74 - 600-eV Precursor Motion in Copper

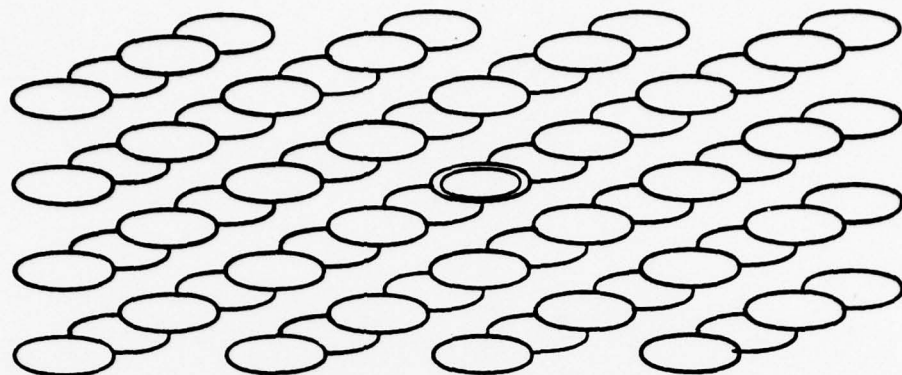


Timestep 4

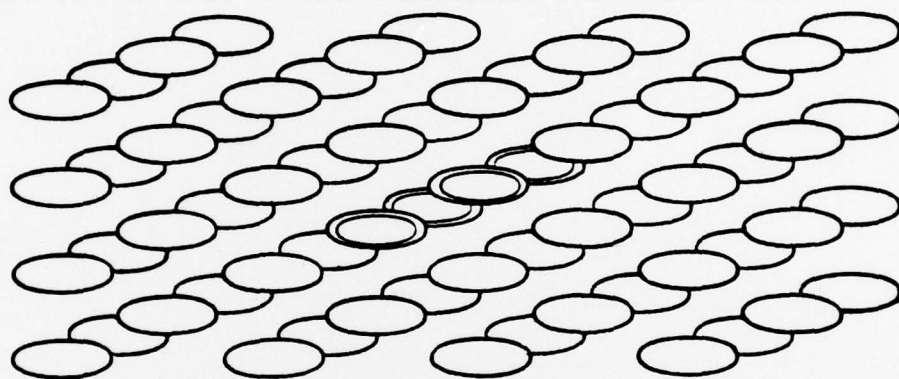


Timestep 5

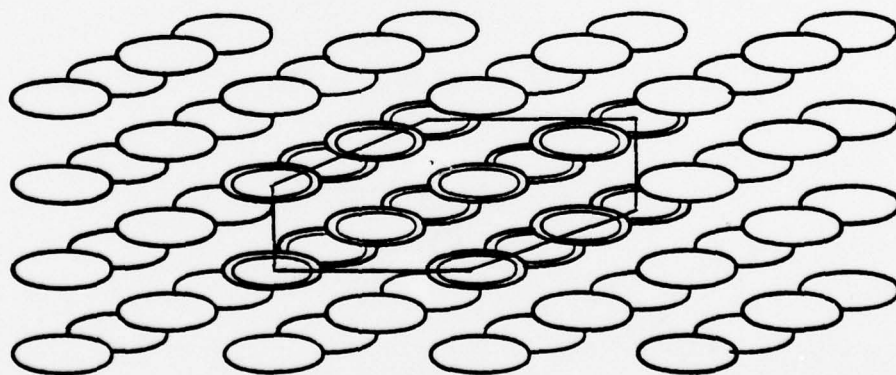
Figure 75 - 600-eV Precursor Motion in Copper



Timestep 1

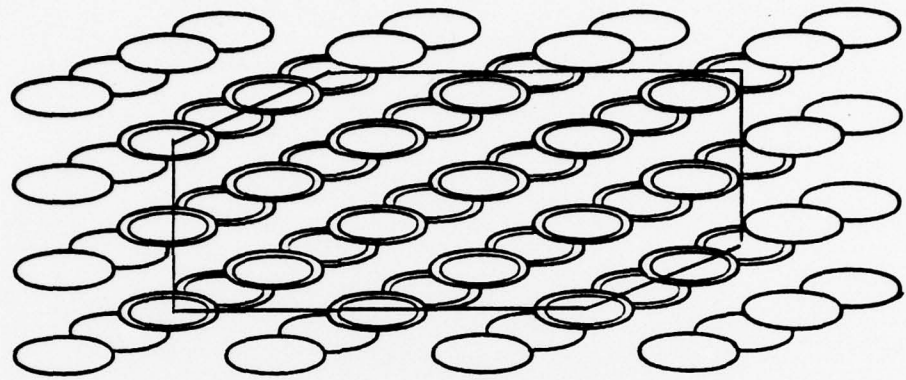


Timestep 2

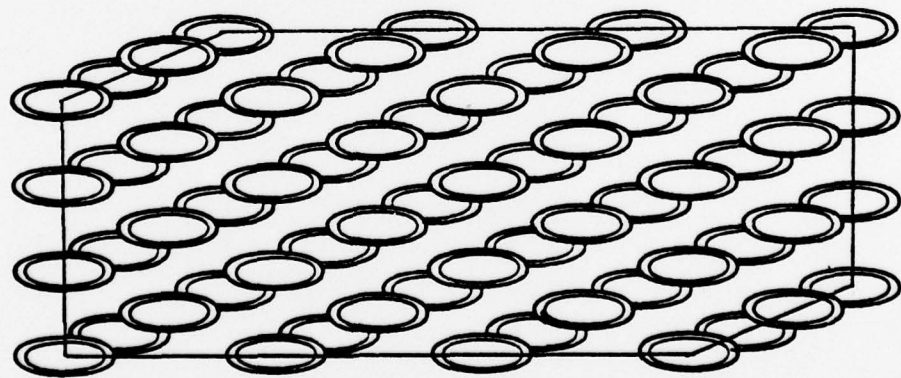


Timestep 3

Figure 76 - 600-eV Precursor Motion in Silicon



Timestep 4



Timestep 5

Figure 77 - 600-eV Precursor Motion in Silicon

LIST OF REFERENCES

1. Litton Industries Report 3031, Surface Bombardment Studies, by G. K. Wehner, G. S. Anderson, and C. E. KenKnight, 27 September 1966.
2. General Mills Report 2309, Sputtering Yield Data in the 100-600 eV Energy Range, 15 July 1952.
3. Thompson, J. J., Rays of Positive Electricity, Longman Green, 1921.
4. Bush, V. and Smith, G. C., Transactions of the American Institute of Electrical Engineers, v. 41, p. 627, 1922.
5. Hippel, A. Von., " Zur Theorie der Kathodenzerstaubung," Annalen der Physik, v. 81, p. 1043-1075, 1926.
6. Lamar, E. S., and Compton, K. T., Science, v. 80, p. 541, 1934.
7. Harrison, D. E. Jr., " Theory of Sputtering Process," Physical Review, v. 102, p. 1473-1480, 15 June 1956.
8. Silsbee, R. H., " Focusing in Collision Problems in Solids," Journal of Applied Physics, v. 28, p. 1246-1250, November 1967.
9. Lehmann, Chr., and Sigmund, P., " On the Mechanism of Sputtering," Physica Statu Solidi, v. 16, p. 507-511, 1966.
10. Sigmund, P., " Theory of Sputtering. I. Sputtering Yield of Amorphous and Polycrystalline Targets," Physical Review, v. 184, no. 2, p. 383-416, 10 August 1969.
11. Gibson, J. B., Goland, A. N., Milgram, M., and Vineyard, G. H., " Dynamics of Radiation Damage," Physical Review, v. 1028 no. 4, p. 1229-1253, 15 November 1960.
12. Harrison, D. E. Jr., Levy, N. S., Johnson J. P. III, and Effron, H. M., " Computer Simulation of Sputtering," Journal of Applied Physics, v. 39, no. 8, p. 3742-3761, July 1968.
13. Harrison, D. E. Jr., Gay, W. L., and Effron, H. M., " Algorithm for the Calculation of the Classical Equations of Motion of an N-Body System," Journal of Applied Physics, v. 10, no. 7, p. 1179-1184, July 1969.
14. Harrison, D. E. Jr., Moore, W. L. Jr., and Holcombe, H. T., " Computer Simulation of Sputtering II," Radiation Effects, v. 17, p. 167-183, 1973.
15. Finno, R. S., A Computer Study of Channeling in Silicon, M. S. Thesis, Naval Postgraduate School, June 1969.

16. Wedepohl, P. T., "Influence of Electron Distribution on Atomic Interaction Potentials," Proceedings of the Physical Society (London), v. 92, p. 79, 15 June 1967.
17. Hartree, D. R., The Calculation of Atomic Structures, Wiley, 1955.
18. Fermi, E., "Statistical Method of Investigating Electrons in Atoms (German)," Zeitschrift fur Physik, v. 48, p. 73-79, 1928.
19. Abrahamson, A. A., "Screening Electron Density Distributions and Thomas-Fermi-Dirac Screening Functions for Neutral Atoms," Physical Review, v. 123, no. 2, p. 538-543, 15 July 1961.
20. Herman, F. and Skillman, S., Atomic Structure Calculations, Prentice Hall, 1963.
21. Wilson, W. D., Haggmark, L. G., and Biersack, J. P., "Calculations of Nuclear Stopping, Ranges, and Stragglings in the Low Energy Region," Physical Review, v. 15, no. 5, p. 2458-2468, 1 March 1977.
22. Harrison, D. E. Jr., Delaplain, C. B., "Computer Simulation of the Sputtering of Clusters," Journal of Applied Physics, v. 47, no. 6, p. 2252-2259, June 1976.
23. Southern, A. L., Willis, W. R., and Robinson, M. T., "Sputtering Experiments with 1- to 5- keV Ar Ions," Journal of Applied Physics, v. 34, no. 1, p. 153-163, January 1963.

INITIAL DISTRIBUTION LIST

	No. Copies
1. Defense Documentation Center Cameron Station Alexandria, Virginia 22314	2
2. Library, Code 0212 Naval Postgraduate School Monterey, California 93940	2
3. Department Chairman, Code 61 Department of Physics and Chemistry Naval Postgraduate School Monterey, California 93940	2
4. Dr. Don E. Harrison, Jr., Code 61HX Department of Physics and Chemistry Naval Postgraduate School Monterey, California 93940	4
5. LT. Gary L. Smith, USN Class 56 SWOSCOLCOM, Bldg. 446 Newport, Rhode Island 02840	1